

From Lipid Bilayers to Synaptic Vesicles: Atomic Force Microscopy on Lipid-based Systems

Dissertation

zur Erlangung des Grades
'Doktor der Naturwissenschaften'

am Fachbereich Biologie
der Johannes Gutenberg-Universität
in Mainz

Ann-Katrin Awizio
geb. in Stuttgart

Mainz, Juli 2007

Die vorliegende Arbeit wurde in der Zeit von November 2003 bis Juli 2007 am Max-Planck-Institut für Polymerforschung durchgeführt.

Datum der mündlichen Prüfung: 25. September 2007

Abstract

The aim of this thesis was to apply the techniques of the atomic force microscope (AFM) to biological samples, namely lipid-based systems. To this end several systems with biological relevance based on self-assembly, such as a solid-supported membrane (SSM) based sensor for transport proteins, a bilayer of the natural lipid extract from an archaeobacterium, and synaptic vesicles, were investigated by the AFM.

For the characterization of transport proteins with SSM-sensors proteoliposomes are adsorbed that contain the analyte (transport protein). However the forces governing bilayer-bilayer interactions in solution should be repulsive under physiological conditions. I investigated the nature of the interaction forces with AFM force spectroscopy by mimicking the adsorbing proteoliposome with a cantilever tip, which was functionalized with charged alkane thiols. The nature of the interaction is indeed repulsive, but the lipid layers assemble in stacks on the SSM, which expose their unfavourable edges to the medium. I propose a model by which the proteoliposomes interact with these edges and fuse with the bilayer stacks, so forming a uniform layer on the SSM.

Furthermore I characterized freestanding bilayers from a synthetic phospholipid with a phase transition at 41°C and from a natural lipid extract of the archaeobacterium *Methanococcus jannaschii*. The synthetic lipid is in the gel-phase at room temperature and changes to the fluid phase when heated to 50°C. The bilayer of the lipid extract shows no phase transition when heated from room temperature to the growth temperature (~ 50°C) of the archeon.

Synaptic vesicles are the containers of neurotransmitter in nerve cells and the synapsins are a family of extrinsic membrane proteins, that are associated with them, and believed to control the synaptic vesicle cycle. I used AFM imaging and force spectroscopy together with dynamic light scattering to investigate the influence of synapsin I on synaptic vesicles. To this end I used native, untreated synaptic vesicles and compared them to synapsin-depleted synaptic vesicles. Synapsin-depleted vesicles were larger in size and showed a higher tendency to aggregate compared to native vesicles, although their mechanical properties were alike. I also measured the aggregation kinetics of synaptic vesicles induced by synapsin I and found that the addition of synapsin I promotes a rapid aggregation of synaptic vesicles. The data indicate that synapsin I affects the stability and the aggregation state of synaptic vesicles, and confirm the physiological role of synapsins in the assembly and regulation of synaptic vesicle pools within nerve cells.

Zusammenfassung

Das Ziel dieser Dissertation war die Anwendung von Techniken der Rasterkraftmikroskopie (RKM) zur Charakterisierung von Lipidsystemen. Die untersuchten Systeme waren: ein Sensor für Transporterproteine, dessen Hauptkomponente eine Festkörper-gestützte Membran ist, eine Lipidmembran vom natürlichen Lipidextract eines Archaeobakteriums und synaptische Vesikel. Für die Charakterisierung von Transportproteinen werden Liposomen, die den Analyt (Transportprotein) enthalten, an die Membran des Sensors adsorbiert. Allerdings sollten die Wechselwirkungskräfte zwischen zwei Lipidmembranen in wässriger Lösung repulsiv sein. Die Art der Wechselwirkungskräfte wurde mit RKM-Kraftspektroskopie untersucht, indem die adsorbierenden Proteoliposomen mit einem Kantilever imitiert wurden, der mit Alkanthiolen funktionalisiert wurde. Die Wechselwirkung war tatsächlich repulsiv, die Lipidmembranen bilden jedoch Stapel von mehreren Doppelschichten auf der Festkörper-gestützten Membran des Sensors. Hier wird ein Model vorgeschlagen, in dem die Proteoliposomen mit den energetisch ungünstigen Seitenrändern der Lipidstapel interagieren und eine einheitliche Schicht auf der Sensormembran ausbilden. Ausserdem wurden frei stehende Lipiddoppelschichten von einem synthetischen Phospholipid, mit einer Phasenübergangstemperatur von 41°C, und vom Lipidextract des Archaeobakteriums *Methanococcus jannaschii* charakterisiert. Die Doppelschicht des synthetischen Lipids befindet sich bei Raumtemperatur in der Gelphase und geht in die flüssig-kristalline Phase über bei Erhitzung auf 50°C. Die Membran des Extraktes zeigte keinen Phasenübergang als sie von Raumtemperatur auf die Wachstumstemperatur (~50°C) des Archeon erhitzt wurde. Synaptische Vesikel transportieren Neurotransmitter in Nervenzellen und besitzen als extrinsische Membranproteine u. a. die Synapsine, die den Zyklus der synaptischen Vesikel während der Singalübertragung zwischen Nervenzellen steuern. Der Einfluss von Synapsin I auf synaptische Vesikel wurde mit RKM Abbildungen, Kraftspektroskopie und dynamischer Lichtstreuung untersucht. Dafür wurden native synaptische Vesikel mit synaptischen Vesikeln, von denen Synapsin entfernt wurde, verglichen. Synaptische Vesikel ohne Synapsin waren größer und zeigten eine gesteigerte Tendenz zur Aggregation im Vergleich zu nativen synaptischen Vesikeln, während bei den mechanischen Eigenschaften keine Unterschiede zu erkennen waren. Zusätzlich wurde die Aggregationskinetik von synaptischen Vesikeln in Abhängigkeit von Synapsin I gemessen. Die Zugabe von Synapsin I führte zu einer sofortigen Aggregation der synaptischen Vesikel. Die Ergebnisse zeigen, dass Synapsin I die Stabilität und das Aggregationsverhalten von synaptischen Vesikeln beeinflusst und bestätigen die physiologische Rolle von Synapsinen bei der Bildung und Regulation der Reservoirs von synaptischen Vesikeln innerhalb der Nervenzellen.

Table of Contents

Abstract.....	4
Zusammenfassung	6
Table of Contents.....	7
Introduction	10
Motivation.....	14
1 Fundamentals	18
1.1 Interaction forces	18
1.2 Interaction forces in aqueous medium	18
1.2.1 DLVO Forces	19
1.2.2 Non-DLVO Forces	21
1.3 Membranes	23
1.3.1 The Cell Membrane	23
1.3.2 Lipids, the bilayer building block	24
1.4 Archae and their diether lipids	28
1.5 Supported membranes	30
1.6 Synaptic vesicles (SV)	35
1.6.1 The synaptic vesicle cycle	37
1.6.2 The biological function of synapsins	37
2 Material & Methods	40
2.1 Chemicals and Lipids	40
2.2 Buffers and Cantilevers.....	40
2.3 Biological samples	41
2.3.1 Gold electrodes.....	41
2.3.2 Tip functionalization	42
2.3.3 Extraction of Methanococcus lipids.....	42
2.3.4 Sample preparation for Archae lipid extract.....	42
2.3.5 Purification of synaptic vesicles	43
2.3.6 Sample preparation for the synaptic vesicles	45
2.4 Methods	46
2.4.1 The Atomic Force Microscope (AFM)	46
2.4.2 Imaging	48

2.4.3	Instrumentation	49
2.4.4	Force Spectroscopy	53
2.4.5	Force Volume Mode.....	56
2.4.6	Cantilever Calibration.....	56
2.4.7	Dynamic Light Scattering	60
3	Results & Discussion	62
3.1	The Solid-supported Membrane (SSM) Sensor	62
3.1.1	Interaction between modified tip and bare substrates	63
3.1.2	Di-oleoyl phosphatidylcholine bilayer by vesicle fusion	64
3.1.3	Comparing the thiol-layer with the glass surface	67
3.1.4	Di-oleoyl phosphatidylcholine in decane.....	69
3.1.5	Di-phytanoyl phosphatidylcholine in decane.....	72
3.2	Archae lipids	76
3.2.1	Influence of temperature on a DPPC Bilayer	76
3.2.2	Methods for bilayer preparation from natural lipid extract.....	80
3.2.3	Influence of temperature on natural lipid extract.....	81
3.3	Synaptic vesicles	86
3.3.1	Establishment of the AFM imaging conditions for synaptic vesicles	87
3.3.2	Shape and size determination of native and synapsin-depleted SVs by DLS and AFM	95
3.3.3	Synaptic vesicles before and after the force-volume scan.....	101
3.3.4	Stiffness measurements with the AFM in FV-mode.....	103
3.3.5	Stiffness data analysis	105
3.3.6	Influence of synapsin I on vesicles in bulk solution by DLS and AFM	107
3.3.7	The use of thawed vesicles.....	111
4	Conclusions.....	116
5	Bibliography	120
6	List of used mathematical symbols, constants and abbreviations.....	131
	Acknowledgements.....	Error! Bookmark not defined.
	Curriculum Vitae	133

Introduction

What is this fashionable buzzword 'nanobiotechnology'? It seems to be a combination of the hot topics prevalent in research and industry. It includes the 'nano' size popular in the areas of physics and chemistry, and biotechnology as the field offering new functional miniaturized systems and approaches to a more sophisticated advancement in medical sciences, e.g. high-throughput analytical devices, more specific drug delivery or tissue engineering [1-4]. The evolving field of nanotechnology offers biology new tools and biology gives nanotechnology access to new types of functional nanosystems, that by themselves or if appropriately mimicked, provide new tools or machines. A closer look shows that the size range of the used objects is not only nano (1 nm – 100 nm) but also micro (0.1 μm to 1000 μm /1 mm) [5]. Nanotechnology evolved from the field of microelectronics and the wish to miniaturize in order to be faster and cheaper with the use of less material [6]. So the manufacturing techniques come from the field of microelectronics and semiconductors and include optical and electron beam lithography [7], deposition to create material layers on a surface or etching methods to selectively remove materials [8]. In addition the characterization techniques like the electron microscope or the atomic force microscope (AFM or scanning probe microscope, SPM) are derived from this field.

Whereas the electron microscope relies on the classical method of imaging the sample with an incident beam (here consisting of electrons), the scanning probe microscope uses a tip attached to a cantilever beam to raster scan the surface. The physical interactions or forces that occur between the tip and the sample are measured by a detection system and assembled to an image with a computer.

Meanwhile the technique of the scanning probe microscope developed further into devices for ultradense data storage in nanoelectronics [9-11] or nanoprinting [12, 13].

In comparison to electronics and physical nanoscience, biological structures are relatively large, e.g. 5 - 50 μm for a mammalian cell. In biological issues though, it is more necessary to follow the dynamic processes and to resolve the internal structural development with high selectivity, than to have the ability to investigate smaller and smaller features.

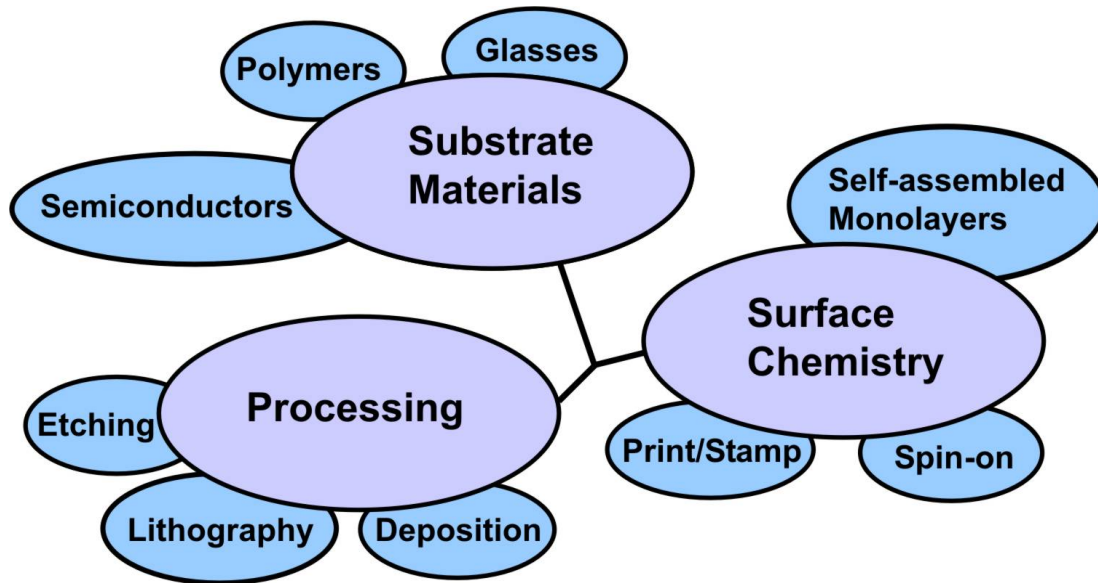


Figure 1.1 Common elements for the fabrication of Bio- Micro-and Nanotechnologies. Graph modified after [8].

In this field the scanning probe microscope and its derivatives still need further development before becoming an easy-to-use technique. Biological structures are electrically insulating and not easily imaged due to their softness, which leads to sample deformation or destruction by the shear forces exerted during the scanning process [14-17]. Conventional molecular bioscience deals with molecules in solution, but in the cell molecules are often organized in functional aggregates. Visualizing and studying these structures is one of the key challenges posed to nanoscience by biology. Progress is achieved in spectroscopic studies of single molecules or biophysical studies of multiprotein aggregates [18-23]. Biology also benefits from nanoscience by new materials and structures: surfaces patterned or modified chemically with self-assembled monolayers (SAMs) or/and printing, stamping and spin-coating [24, 25] of material; the use of substrate materials from the semiconductor industry like silicon, glass, polymers, microstructured three-dimensional scaffolds for tissue-engineering, nanoparticles as probes or new optical systems for imaging. SAMs provide the ability to modify relatively large areas of square centimetres with highly ordered molecules and a tailor-made surface property for the attachment of cells or for further application in nanobiotechnology like e.g., the

first modification step towards a membrane-based biosensor [26-28] (see also chapter 1.5).

The invention of the AFM in 1986 [29], followed by continuous improvement, has revolutionized the way in which microscopists explore biological structures [30-32]. Despite the aforementioned shortcomings the main advantage of the atomic force microscope is to provide direct topographic images of biological specimen under physiological conditions and at a resolution of several nanometers. The AFM can also measure forces within or between biological samples with a sensitivity in the piconewton range [33, 34] by directly probing the sample with the tip. Many specimens have been examined since the late 1980s, ranging from biological molecules such as DNA, to lipid membranes and cells [35-37].

Motivation

The aim of this thesis was to apply the techniques of the atomic force microscope (AFM) to biological samples, namely lipid-based systems. To this end, several systems with biological relevance based on self-assembly, such as a solid-supported membrane (SSM) based biosensor, a bilayer of the natural lipid extract from an archaebacterium and synaptic vesicles, are investigated by the AFM. First, a well-established high throughput screening sensor for transporter assays is studied by force-spectroscopy [38]. This sensor is based on an integrated membrane system with a thiol monolayer self-assembled on a gold electrode, and a second layer of diether lipids, complementing the bilayer, added from a decane solution. The analyte is applied to the SSM of the sensor via the adsorption of membrane fragments or proteoliposomes containing the ion-pump or enzyme under investigation on top of the supported bilayer. This device allows a rapid solution exchange under high pressure without removing the analytes. Since the headgroups of both membranes, the one of the sensor and the one of the sample are charged, a repulsion between them is expected. However, experimentally they attract each other. To investigate this unknown, attractive interaction I employed a simplified system and mimicked the interaction between two charged layers with the solid supported membrane (SSM) and an AFM tip, which was covered with hydroxyl-terminated thiols. This hydrophilic thiol layer is charged in solution and acts as a substitute for charged lipid headgroups. As a reference for a known repulsive interaction, a synthetic, charged lipid was dissolved in decane and used for the membrane. I assembled also a bilayer on the electrode by vesicle fusion from an aqueous suspension. This freestanding bilayer acted as a comparison and a control in case the different interaction is connected to the solvent from which the lipid molecules are applied. Finally, I assembled the SSM layer by layer and monitored each step with the AFM. I can show that this system displays the repulsive interaction that was expected. Based on my findings of bilayer stacks on top of the membrane I propose a mechanism that leads to the attraction and the fusion of the added liposomes due to the exposure of unfavourable bilayer edges to the aqueous medium.

Diether lipids form membranes with a high electron impermeability, which is a desired feature for sensors dealing with electron-transport. These lipids are derived from archaeobacteria, which are organisms living under extreme conditions of temperature, pressure and salinity. These lipids have also an intrinsic temperature stability, when assembled to liposomes or membranes these assemblies keep their structure and stability over a wide range of temperatures. In addition they have a resistance to chemical modification, e.g. the phytanyl chains resist oxidative processes [39]. These characteristics make them prone for functionalising surfaces, which have to resist high temperatures [40], or as anti-corrosive coatings [41, 42].

This led us to the question if it would be possible to form a bilayer from a natural total lipid extract of an archaeobacterium (*Methanococcus jannaschii*) and what material properties such a bilayer would display, if heated from room temperature to the growth temperature of this archaeon. I compare this bilayer to a bilayer made of a synthetic ester lipid, dipalmitoyl phosphatidylcholine (DPPC) which has a phase transition that lies within the chosen temperature range [43].

The AFM is also suitable to investigate the material properties of larger biological assemblies such as cells or cellular organelles. By operating the AFM in force-volume-mode (FV-mode), information on the mechanical properties of natural or artificial samples can be obtained [33, 34, 44-47]. I used this mode to compare the morphology, the mechanical properties, the aggregation state of natural synaptic vesicles (SVs), purified from rat forebrain, in the presence and absence of endogenous synapsin. Synaptic vesicles are spherical organelles located at the nerve terminals, which store and release neurotransmitters. Synapsin is one of the most abundant peripheral membrane proteins associated with them and its removal from the nerve terminal leads to a significant decrease in the number of SV. Since synapsin is known to stabilize phospholipid bilayers, I wanted to investigate its influence on the stabilization of SVs.

Additionally, I studied the aggregation kinetics with dynamic light scattering (DLS). This method allows to measure size distributions of particles in the submicrometer range, by simply knowing the viscosity of the dispersive phase [48].

Overview

First I give an introduction in the chapter *Fundamentals* to interaction forces valid in aqueous medium, to membrane systems and lipids . I will also explain the biological systems that I used for my experiments: the solid supported membrane sensor, the archae lipids and the synaptic vesicles. Moreover in the chapter *Materials and Methods* the materials (buffers, cantilevers, substrates) and devices (the different atomic force microscopes, the heating stage and the DLS instrument) are described, together with an explanation of the used methods and of the sample preparation procedures . Finally, the results of this work are discussed in three subchapters and in each the findings are compared with the available literature in the chapter *Results and Discussion*.

1 Fundamentals

1.1 Interaction forces

Atomic force microscopy is used in this work to characterise topography and also local mechanical properties of the samples. A system that has the sensitivity to measure forces in the range of piconewtons is also sensitive to surface forces that occur at the tip-sample interface.

Therefore a basic knowledge of these forces is essential for the interpretation of the data obtained by AFM experiments. Since all the measurements in this work were carried out in buffer, a requirement for most biological samples, I give a brief overview in the following paragraphs about some of the most important forces, that occur between surfaces in solution [33, 49, 50].

1.2 Interaction forces in aqueous medium

Surface forces governing the behaviour of dispersions can be divided into DLVO-forces (described by Derjaguin, Landau, Verwey and Overbeek) and non-DLVO forces. Dispersions or colloids are two-phase systems, in which one phase has the dimension of 1 nm to 1 μm , e.g., colloidal particles, and is suspended in the matrix of the other phase. Colloidal particles have such a large interface-to-volume ratio due to their small size, that their behaviour is determined completely by surface properties and gravity becomes negligible. For more than 100 years it has been known that many aqueous dispersions precipitate upon the addition of salt. The theory describing this effect quantitatively was developed by Derjaguin, Landau, Verwey and Overbeek, and is called after them the 'DLVO'-Theory [51, 52]. However not all effects observed, while studying the interaction of surfaces, are explained by that theory. For the non-DLVO forces the theories and models are still under debate, although the existence of them has been experimentally verified.

1.2.1 DLVO Forces

The DLVO Theory describes quantitatively the interaction between particles with an attractive van der Waals force and a repulsive electrostatic double layer force. This describes dispersions of particles. If salt is added the particles precipitate. Charged particles are held in suspension by the electrostatic repulsion between them. With the addition of salt the repulsion is decreased and the particles approach until the attractive van der Waals force dominates and they aggregate to larger assemblies, which cause them to precipitate.

Van der Waals

The van der Waals force F_{vdW} is the sum of three kinds of dipole-dipole interactions:

- *The Keesom energy*, describing the interaction between two freely rotating dipoles [53, 54]
- *The Debye energy*, describing the interaction between a dipole and a polarisable, non-dipolar molecule [55, 56]
- *The London dispersion energy*, describing the attraction between two non-polar molecules with a fluctuating dipole moment in terms of quantum mechanics [57]

$$F_{vdW} = C_{orientation} + C_{induced} + C_{dispersions}$$

The potential energy decreases with $1/D^6$ (distance D) between two molecules and with $1/D^3$ between a macroscopic body and a molecule or between two macroscopic bodies. Usually the London dispersion energy is dominating [49].

Electrostatic double layer force

The origins of the electrostatic double layer force are surface charges at interfaces. Due to the high dielectric constant of water the dissociation and adsorption of charged species on the surface is a common process. The charged surface and the counterions balancing it in solution are known as the electric double layer.

When surfaces with charges of the same sign approach, the concentration of ions between the surfaces increases, which results in a repulsive force. The electric double layer force decays roughly exponentially at large distances. The decay length is called *Debye length* λ_D , which is determined by the salt concentration c . For a monovalent salt it is

$$\lambda_D = \sqrt{\frac{\epsilon\epsilon_0 k_B T}{2ce^2}}$$

For water at 25°C it can be simplified to $\lambda_D = 3.04/\sqrt{c}$ (the result is expressed in nm with c in mol/l).

When ions of higher valency Z_i are present the term $2c$ has to be replaced by $\sum c_i Z_i^2$. The sum runs over all ions present with c_i being the bulk concentration of the i th ion species. In a 0.1 M aqueous solution of NaCl at 25°C the Debye length is 0.96 nm. Due to the dissociation of water which keeps the ion concentration at least at 2×10^{-7} mol/l it cannot be longer than 680 nm and usually is only a few 100 nm since even distilled water contains ionic impurities or has a pH differing from pH 7.

The electrostatic double layer force can be calculated using continuum theory. Gouy [58] and Chapman [59] developed a theory for a diffuse layer of ions near the charged surface, based on the thermal fluctuations that drive counterions away from the surface. They applied this theory to planar surfaces, whereas Debye and Hückel calculated the potential and ion distribution around spherical surfaces [60]. In both cases the solvent is treated as a continuous medium with a certain dielectric constant and ions are treated as a continuous charge distribution.

The potential distribution between two surfaces is determined from the Poisson-Boltzmann equation, a second-order differential equation. To solve this equation certain boundary conditions have to be assumed. The usually assumed boundary conditions for approaching the surfaces are that either surface charges or that surface potentials remain constant. Two surfaces with constant charge of equal sign always repel each other for $D \rightarrow 0$. Two surfaces with constant potential are attracted for $D \rightarrow 0$, even when the surface potentials have the same sign [50, 61].

For aqueous solutions the DLVO theory provides relatively good predictions for monovalent salts at concentrations below 0.2 M and for potentials below 50–80 mV.

These salt concentrations are in the range of physiological buffer conditions. Deviations occur for bivalent and trivalent salts because of the actual discrete distribution of surface charges in opposition to the assumed continuous distribution.

1.2.2 Non-DLVO Forces

Hydration repulsion

When two hydrophilic surfaces are brought into contact in an aqueous electrolyte, repulsive forces in the range of 1-3 nm are observed. These forces are attributed to the energy required to remove water of hydration from the surface and therefore were termed hydration forces [62]. They are relatively short-ranged, repulsive and decay in most cases exponentially with distance. With increasing salt concentration, especially divalent cations, hydration forces tend to become stronger and longer ranged as opposed to the electrostatic double layer force. At salt concentrations below 0.1 M they can be distinguished from the longer range electrostatic and van der Waals forces.

The origin of hydration forces is not yet clear. Several effects could contribute to the short-range repulsion mainly observed between approaching lipid bilayers or other flexible, amphiphilic surfaces. Molecular scale fluctuations of hydrocarbon chains or a steric repulsion between mobile headgroups may contribute significantly [63].

In addition the single molecules in lipid bilayers undergo a thermal motion perpendicular to the bilayer plane and protrude alternately several angströms into the medium within a timescale of picoseconds. This fluctuation is hindered, if two bilayers approach each other. The entropy of the lipid molecules decreases and subsequently for both membranes the thermodynamic potential (Gibb's free energy) increases, therefore the two bilayers repel each other.

Hydrophobic attraction

Hydrophobic surfaces in water attract each other. This attraction is called hydrophobic interaction [64]. The origin of this interaction, which is stronger and longer ranged than the van der Waals attraction, is still under debate. It consists of two components: a short-ranged one that decays exponentially with a decay length of typical 1-2 nm and a long-ranged one which extends to several 100 nm in some cases [65]. The first one is attributed to a change in water structure upon approach of the surfaces. For the second one several theories exist. One of them involves the existence of gas bubbles on a hydrophobic surface. The fusion of these nanobubbles when contacted leads to the formation of bigger cavities and subsequently to a strong attraction due to the meniscus force [66]. A number of AFM experiments already proofed the existence of such bubbles and also the dependence of the long-range components on the concentration of dissolved gases in the medium was shown.

For one hydrophobic and one hydrophilic surface, attraction dependent on the hydrophobicity of the substrate was observed although one order of magnitude lower than for the symmetric hydrophobic interaction [67].

1.3 Membranes

1.3.1 The Cell Membrane

The membrane envelopes the cell as a fluid leaflet made of a double layer of pinlike lipid molecules. The pinheads are the hydrophilic headgroups of the lipids, exposed to the aqueous environment and the elongations are the hydrophobic hydrocarbon chains that are arranged towards each other inside the membrane. It consists of roughly 100 different types of lipid and protein molecules as well as of carbohydrates. A pure lipid membrane acts as an insulator and membrane proteins inserted into it lead to a selective permeability regarding ions, chemical molecules or even small peptides depending on the transporters associated with the specific function of the cell or compartment. The membrane is stabilized by a two-dimensional network of protein filaments (fibers made of protein monomers, i.e., actin filaments) that are attached to proteins, which are anchored in the membrane.

There are numerous models describing a biological membrane. Singer and Nicholson proposed the first one. In 1972 they summarized the evidence gathered by research over the preceding decade and presented in *Science* 'the Fluid Mosaic Model' [68] (Figure 1.1a). In the model the membrane is seen as a fluid lipid sheet, in which some integral proteins are freely diffusing, leaving the majority of the bilayer surface exposed to the aqueous environment.

This simplistic model was updated over the years with more complex interrelations found between the molecules. Not only proteins, but also lipids group together with specific lipid-lipid and lipid-protein interactions and are forming regions of separated composition on their own (lipid rafts) [69, 70]. The different protein complexes, lipid rafts or protein-lipid domains lead to a restriction of the fluidity in the membrane plane, influencing the lateral diffusion of small molecules. Fluidity seems only possible within lipid channels separating these specific domains [71, 72].

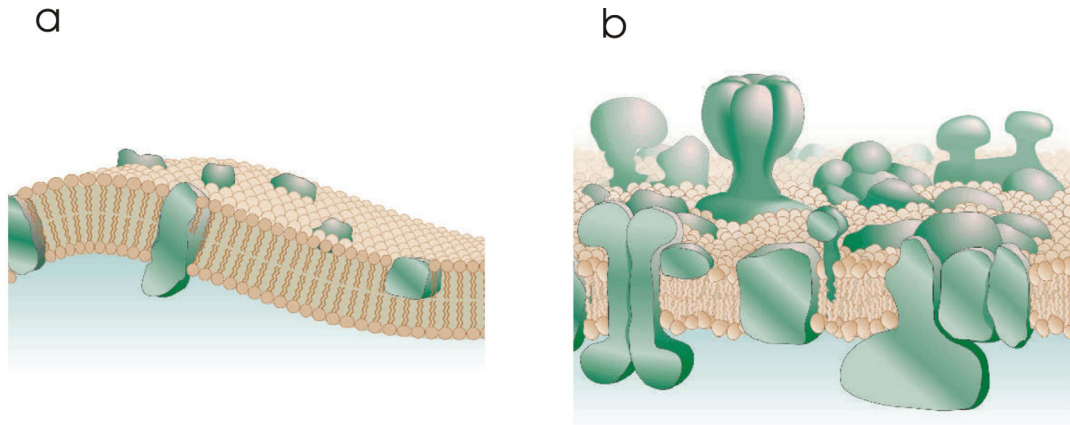


Figure 1.1 (a) Simplistic membrane model according to Singer and Nicholson in 1972 [68]. (b) Updated membrane model according to Engelman 2005 [73]

Membranes seem to be systems of variable patchiness, variable thickness and with a higher protein occupancy than has been considered for the last decades [73]. They are nowadays thought to resemble more a mosaic than a fluid layer in organization (Figure 1.1b).

1.3.2 Lipids, the bilayer building block

Membrane lipids are amphiphilic molecules with a hydrophilic headgroup and a hydrophobic tail. They display a large diversity of chemical structures and self-assemble into bilayer phases that fulfill a variety of biological functions.

Depending on the experimental conditions in aqueous media, the molecules self-assemble to micelles, vesicles or bilayers. These aggregates are formed spontaneously, if lipid molecules encounter an aqueous environment. The hydrocarbon chains are screened as much as possible from water, a process that is driven by the 'hydrophobic effect': Water molecules are arranged into a loose network of hydrogen bonds and by the addition of an hydrophobic molecule, this network is disturbed. The water molecules are forced to a more ordered arrangement in the vicinity of the hydrophobic molecule and their entropy is decreased. So the interface that lowers their entropy is reduced to a minimum and therefore lipid molecules assemble to higher structures in order to reduce the contact region [74].

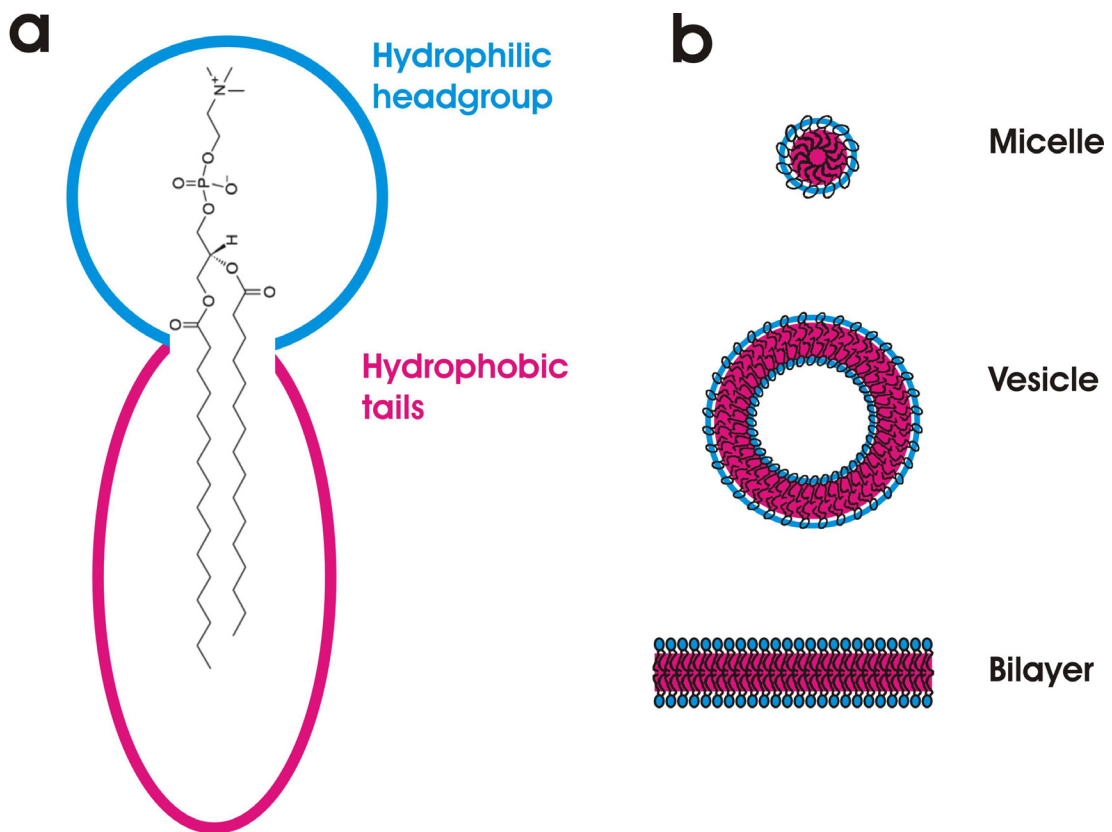


Figure 1.2 (a) Properties of lipid molecules. (b) Self-assembled structures of lipid molecules in water. Lipids with a conical shape assemble to micelles, whereas lipids with a cylindrical shape form bilayers or vesicles.

The major classes of lipids are phospholipids, glycolipids and cholesterol.

The phospholipids have two fatty acid chains and their polar headgroup esterified to the carbon atoms of the glycerol moiety. Headgroup molecules can be Phosphatidylcholine (PC), Phosphatidylserine (PS), Phosphatidylglycerol (PG), alcohol based such as Phosphatidylethanolamine (PE) or sugar derivatives such as Phosphatidylinositol (PI). PC and PE are neutral (zwitterionic) whereas PS, PG and PI can be electrically charged. This difference plays a role for the binding of proteins or drugs to the membrane.

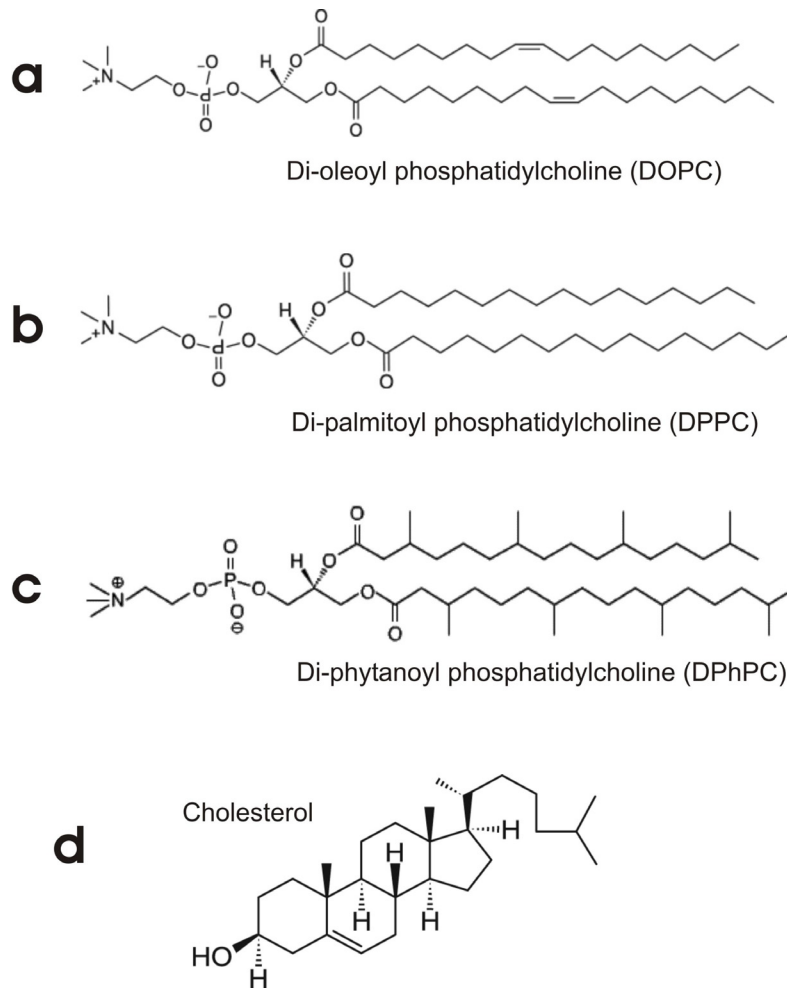


Figure 1.3 Examples of lipid molecules. (a) DOPC, with an unsaturated double bond at C₁₈, (b) DPPC, a saturated lipid, (c) DPhPC, a diether lipid with hydrocarbon chains made from isoprene units, (d) cholesterol with the bulky structure characteristic for steroids

The fatty acid alkyl chains usually contain an even number of carbon atoms as a result of the fat metabolism they are originating from. The length ranges from C₁₂ to C₂₄ with the degree of unsaturation increasing with the chain length. The number of unsaturated double bonds in the fatty acid chains determines the phase transition temperature of the lipid. The longer the lipid chains the higher the number of double bonds to keep the membrane in it's fluid state.

Cholesterol

Cholesterol plays a special role in biological membranes. This bulky molecule keeps membranes in a liquid-ordered phase. The hydrocarbon chains are ordered by the intercalation of cholesterol but the fluidity of the membrane is retained over a wider range of temperature.

Phase transition

Homogenous, artificial bilayers are found to undergo a variety of phase transitions [75], however the main transition is the one occurring at the highest temperature. The main transition is characterized by a specific transition temperature, T_m , which depends on the length of the hydrocarbon chain and their degree of unsaturation.

For example the saturated di-palmitoyl phosphatidylcholine (DPPC, Figure 1.3b) has a transition temperature of 41°C, whereas di-oleoyl phosphatidylcholine (DOPC, Figure 1.3a), with one unsaturated double bond in each hydrocarbon chain, has a T_m of -20°C [76, 77].

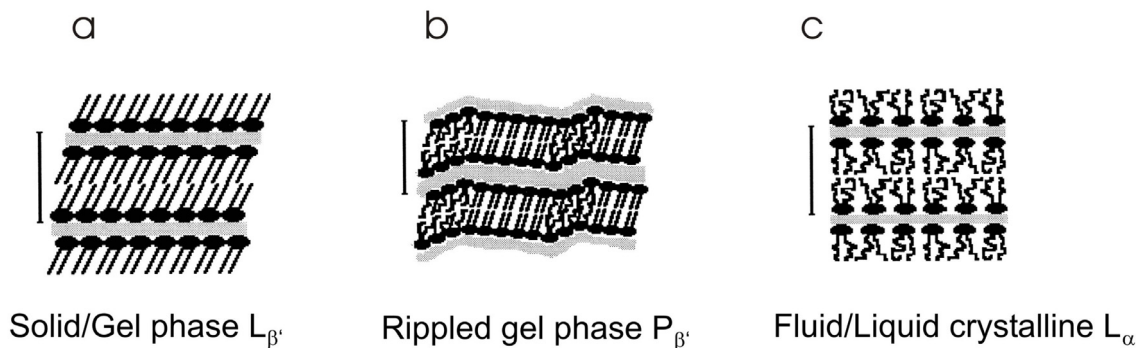


Figure 1.4 Schematic of main lamellar phases at the phase transition from the gel phase (a) over the rippled gel phase (b) to the fluid crystalline phase (c) [77]

At the main transition temperature, the bilayer changes from a gel like solid-ordered state to a fluid liquid-disordered state. Solid and liquid describe the positional degree of freedom for the single molecules whereas ordered and disordered refer to the conformational degree of freedom of the fatty acid chains.

1.4 Archae and their diether lipids

Archae bacteria are microorganisms living under extreme conditions (extremophiles), as existed on the primitive earth, namely, high temperature, anaerobic atmosphere and high salinity. They form the third domain of life on earth besides eubacteria and eukarya [78] differing from them in three major points:

- The sequence of the ribosomal RNA of the small, 16S unit differs from the sequence of both, eubacteria and eukaryotes
- The cell wall consists of glycosylated proteins rather than the peptidoglykan structure in eubacteria
- The membrane lipids are unique ether-linked isoprenoid structures, which are stereospecific regarding the glycerol backbone.

One of the best characterized extremophiles is the methanogen *Methanococcus jannaschii* [79], which lives near hydrothermal vents under extreme temperatures (up to 80°C) and whose genome was completely sequenced 1996 [80].

The lipid composition of the cell membrane comprises 80 – 95% of polar glycerolipids of various structures and headgroups and 5-20% neutral squalenes and other isoprenoids. The polar glycerolipids of methanogens show various structural properties. Three major core components are a diether (D, 2,3-di-O-phytanyl-*sn*-glycerol), a macrocyclic diether (D_m, 2,3-di-O-cyclic-biphytanyl-*sn*-glycerol), only present in the strain of *Methanococcus jannaschii* [81], and the bolaamphiphile tetraether (T, 2,2',3,3'-dibiphytanyl-*sn*-diglycerol).

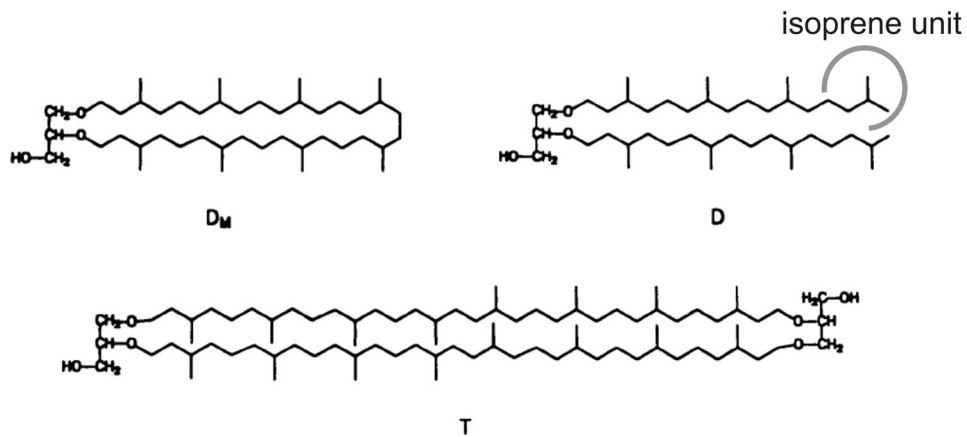


Figure 1.5 Structures of the ether lipid cores in *M. jannaschii*. D_m , macrocyclic diether; D , diether; T , tetraether; [82]

Methanococcus jannaschii can grow at temperatures that range from 45°C to 70°C. At higher growth temperatures this methanogen alters the ether lipid cores dramatically from a mainly diether core fraction when grown at 50°C to an increasing fraction of macrocyclic/tetraether structures when grown at higher temperature, e.g., 60°C [82].

	Diether core [%]	Macrocyclic Diether Core [%]	Tetraether Core [%]
Grown at 50°C	60	19	15
Grown at 60°C	21	42	43

Table 1. Proportions of ether lipid cores in *M. jannaschii* according to growth temperature

At the growth temperature of a given organism the lipids are in a liquid crystalline state [83], so by increasing the tetraether fractions the extremophiles maintain the necessary liquid crystalline phase of the membrane lipids.

1.5 Supported membranes

Mimicking the cellular membrane with artificial bilayer systems makes the investigation of membrane proteins and their functions possible. Two major categories are freestanding bilayers across a hole that separate two fluid compartments (black lipid membranes) or bilayers supported by a solid base and formed by synthetic lipids or other amphiphiles, so-called solid supported membranes (SSM). Solid supported membranes have the advantage that the bilayer is stabilized by the support, which acts as a substitute for the cytoskeleton, and that it is possible to transfer the specificity and the selectivity of proteins via a membrane to an electrode surface [84-86].

Their addition to the area of proteomics is valuable, since most proteins that act as targets for drugs like, e.g., receptors for cellular signalling or transporters for glucose or neurotransmitter, are membrane proteins.

There are three types of supported membranes (Figure 1.6):

- Integrated bilayers (a)
- Freely supported bilayers (b)
- Tethered bilayers (c)

Apart from the integrated bilayer keep the other systems the structural and thermodynamic behaviour of a free lipid bilayer despite the solid support.

Integrated bilayers

Integrated bilayers have the inner leaflet directly linked to the substrate either covalently by conjugating techniques or by ion bridges. Here advantage is taken of the self-assembly of alkyl mercaptanes on gold, which leads to a covalent bond between the sulphuric group of the alkyl and the gold. Gold has a high surface energy and adventitious materials from the environment adsorb easily. The strong binding energy between the sulphuric group and the gold leads to an elimination of such contaminants during the spontaneous coverage of the surface, which results in a defect-free thin film with the desired functionalization that is defined by the endgroup [28].

The outer leaflet is deposited by either Langmuir-Blodgett (LB) transfer or by vesicle fusion. The advantage is a highly reproducible system that makes detection of electrical signals possible e.g. for the investigation of ion pumps and transporters for charged molecules. But the fluidity of the bilayer is compromised by strong linkage of the inner leaflet to the substrate.

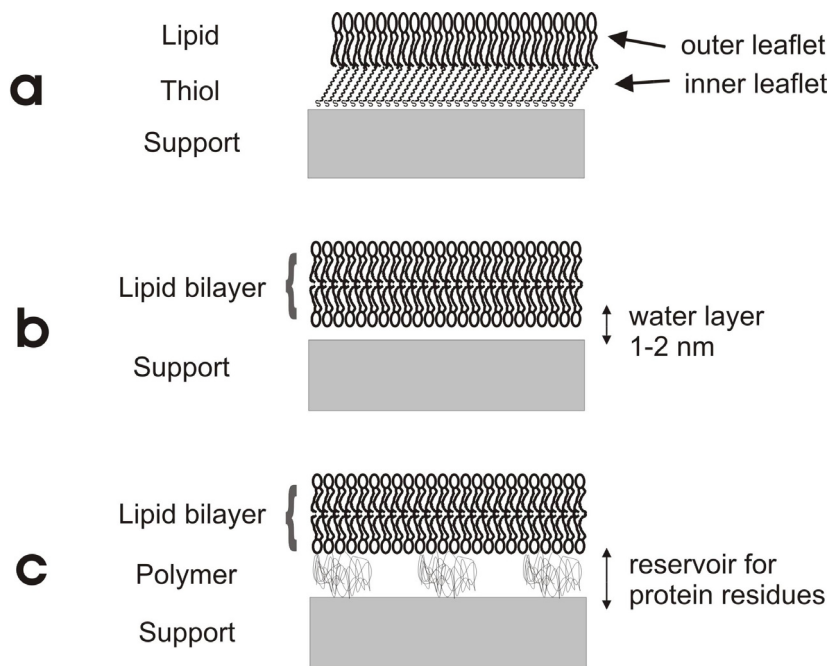


Figure 1.6 Types of supported membranes. (a) Integrated Bilayer, the inner leaflet is linked to the substrate, (b) Freely supported bilayer, a thin water layer divides the bilayer and the substrate, (c) Tethered lipid bilayers, the bilayer is separated from the substrate by polymer cushions or polymer chains

Freely supported bilayer

The freely supported bilayer is a fluid membrane separated from the substrate by a thin water layer of approximately 1 or 2 nm thickness. This water layer provides lubrication and maintains sufficient mobility for the lipid molecules [87]. The bilayer is achieved by either LB transfer or by spreading of vesicles on a hydrophilic substrate.

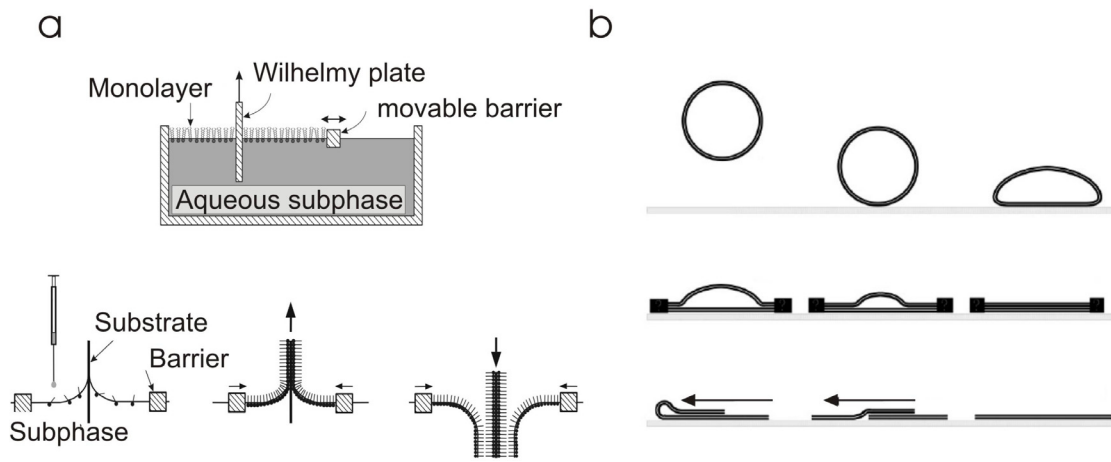


Figure 1.7 Methods to create a freely supported bilayer. (a) Langmuir-Blodgett transfer has the advantage that the density of the molecules can be controlled [50], (b) Vesicle fusion yields fluid bilayers in thermal equilibrium [88], the vesicle attaches to the surface, flattens and spreads into a bilayer patch.

Since it is thermodynamically in equilibrium the fluidity of the bilayer is retained. However the application for a biosensor system is hindered since the system can not dry out because the bilayer structure would then be destroyed.

Also the small space between the bilayer and the substrate is unsuitable for proteins with a large domain protruding into the cellular compartment, because the function could be compromised by an unwanted interaction with the substrate [89].

Tethered lipid bilayers

Tethered lipid bilayers are often the choice when it comes to the investigation of large membrane proteins. The membrane is separated from the substrate by polymer cushions or spacers allowing for some space beneath the membrane, while the bilayer is still attached to a stabilizing support. This submembrane space ranges from 10 to 100 nm [90] and provides a reservoir for large protruding domains of membrane proteins. Interactions with the substrate are reduced and the protein can move freely in the bilayer or change the conformation without any constriction.

A big variety of such systems is developed, regarding the chemistry of the substrate and the molecules used for the inner leaflet [91].

The SSM-sensor is an integrated membrane

Transport proteins in membranes are important targets for drug discovery, since membrane transport plays a crucial role in the development of disease [92, 93]. The difficulty with transporter sensors is, that the transport protein should be efficiently incorporated into a membrane for proper function, and the translocation of the substrates across the membrane should be monitored.

Special techniques have been developed recently to observe charge displacement in electrically active transporters. These are based on solid supported membranes (SSM). They take advantage of the specific capacitance and the stability of a lipid bilayer prepared on a solid support. The transporter protein is incorporated into liposomes (proteoliposomes), which are then adsorbed to the SSM. The currents, which are generated by the transporter activity, are recorded via the potential difference between one electrode in the medium and the electrode, on which the membrane is assembled (Figure 1.8), [94-96].

The SSM can withstand high flow velocities. By rapidly changing from a solution that contains no substrate for the transporter to one that contains a substrate, the transporter can be activated and a transient current can be recorded.

For example, the transporter protein Na^+/K^+ -ATPase is electrogenic in the absence of potassium ions and the disappearance of the current response after an ATP concentration jump can be followed (Figure 1.8b).

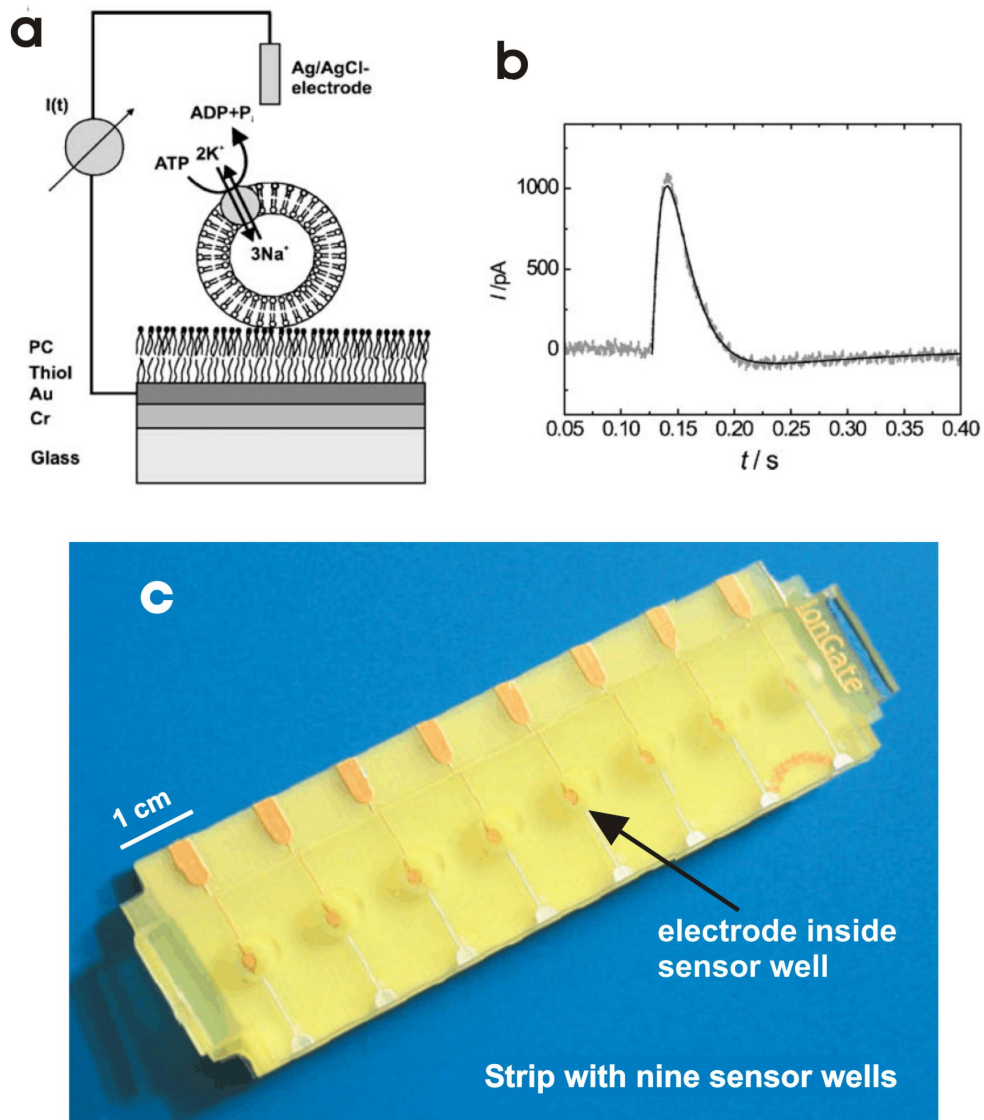


Figure 1.8 (A) Components of the solid-supported membrane (SSM). Glass support, gold electrode (Cr and Au), a thiol monolayer (Thiol), a diether phospholipid monolayer (PC), and liposomes with the incorporated transport protein (e.g. Na⁺/K⁺-ATPase). (B) Electrical current of the Na⁺/K⁺-ATPase in vesicles after adding ATP-containing buffer. (Picture from [95]). (C) Commercial SSM-sensor strip with nine electrodes embedded in sensor wells (IonGate Biosciences, Frankfurt a. M., Germany) .

1.6 Synaptic vesicles (SV)

The nervous system coordinates the flow of information and the resulting actions of the body with a variety of neural circuits. A part of the circuits are synapses, the neurally active sites between two nerve cells. At chemical synapses signals are transmitted with chemical molecules, i.e. neurotransmitter which are stored and released by synaptic vesicles.

A synapse comprises as a functional unit:

- the presynaptic ending at the axon of a nerve with the synaptic vesicles assembled at the active zone of the presynaptic membrane
- the synaptic cleft with a width of 20 nm
- the postsynaptic membrane of the opposite neuron with the corresponding receptors for the neurotransmitter (Figure 1.9).

An action potential reaching the presynaptic end of the neuron triggers the exocytosis of the synaptic vesicles and the release of their content molecules into the synaptic cleft. The neurotransmitter triggers ion channels at the postsynaptic side by binding to the specific receptors, which are linked to ion channels. The opening of the channels leads to a depolarisation and a potential change at the postsynaptic ending of the nerve cell propagating the nerve signal.

Characteristic for synapses is the presence of clusters of synaptic vesicles in the presynaptic terminal [97]. These organelles have a diameter of appr. 40 nm and are composed of a specific set of proteins and lipids. Obligatory components of the protein fraction are transport proteins for the uptake of neurotransmitter and proteins necessary for traffic at exo –and endocytosis. These are necessary for the reliable and constant recycling of these organelles, enabling the synapse to transmit signals repeatedly.

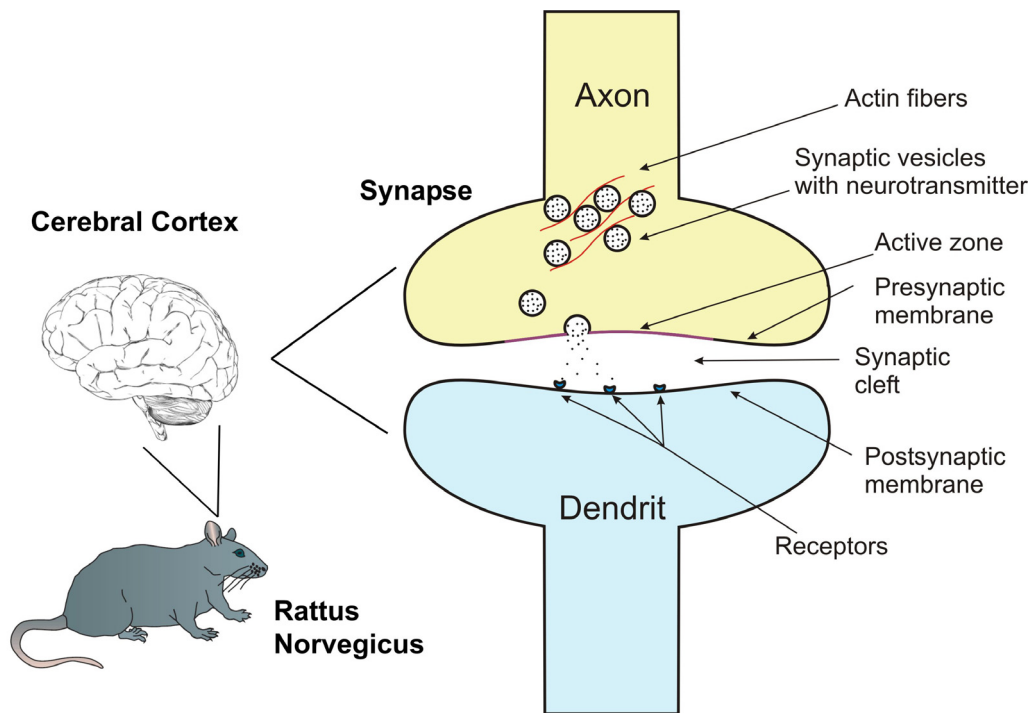


Figure 1.9 Chemical synapses are functional units of the nervous system where signals are transmitted between nerve cells. Synaptic vesicles are located at chemical synapses in the brain (cerebral cortex).

The clusters are functionally divided into so-called pools. The total number (~ 300) of synaptic vesicles partaking on exo –and endocytosis are the recycling pool, which divides further into a readily releasable pool, vesicles released immediately after stimulation, and a reserve pool of vesicles, which are recruited upon longer lasting stimulation [98].

1.6.1 The synaptic vesicle cycle

SV undergo a rapid (< 30 sec) trafficking cycle at the nerve terminal which involves several sequential steps (Figure 1.10):

- Loading the SV with neurotransmitter by active transport,
- Clustering in front of the active zone at the presynaptic terminal,
- Release from the clusters upon signalling (Ca^{2+} - influx),
- Docking at the active zone,
- Priming of the vesicles,
- Calcium-dependent opening of the fusion pore to release neurotransmitter.

For the fusion step are two different mechanisms known. One is the 'full fusion' mode, where the SV merges completely in the membrane and is retrieved by clathrin-mediated endocytosis [99]. In the other one ('kiss and run') the SV releases the content by forming a transient fusion pore with the presynaptic membrane, which allows fast undocking of the vesicle afterwards without the full intermixing of the membranes [100, 101]. An even faster recycling step of this mode is 'kiss-and-stay', where the vesicle is recycled directly at the membrane without undocking from the active zone [102].

The mechanisms that trigger the formation of the pools and govern the recycling pathways are not completely understood yet. However a family of proteins called 'synapsins' seems to play an important role in these mechanisms.

1.6.2 The biological function of synapsins

Several lines of evidence support this view:

Immunoelectron microscopy studies showed that within the nerve terminals, the synapsins are concentrated in areas occupied by synaptic vesicles [103-105]. In addition subcellular fractionation showed that the synapsins are enriched in fractions containing synaptic vesicles [106]. Later studies determined that the high-affinity binding of synapsin I and II to the membrane of synaptic vesicles is mediated by multiple sites located on the N-terminal and middle portions of the molecules. These sites bind specifically to acidic phospholipids [103, 107, 108].

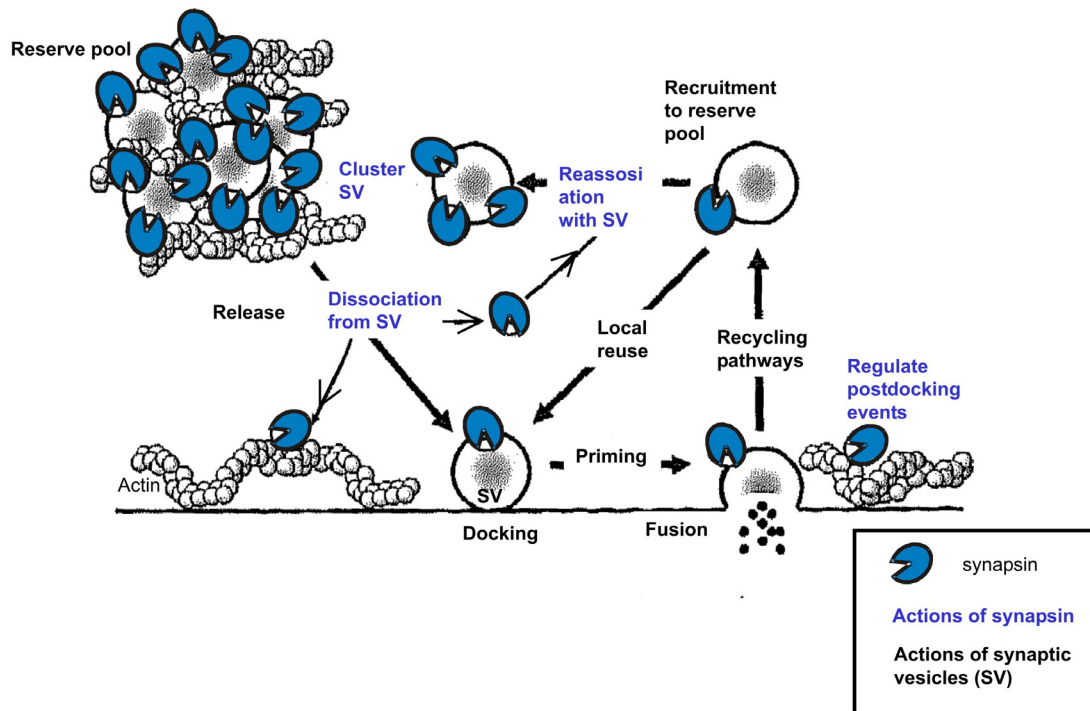
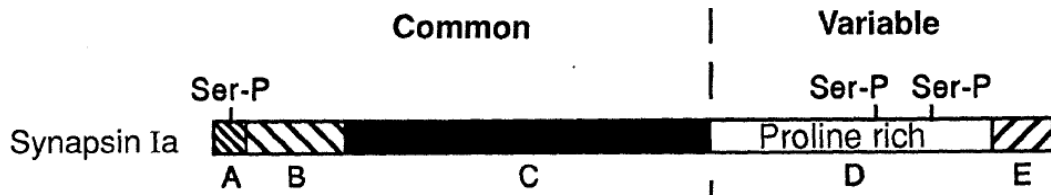


Figure 1.10 Simplified schematic of the synaptic vesicle cycle and the role of synapsins. Graph modified after [109].

These studies have led to a model in which synapsins, by tethering synaptic vesicles to each other and to an actin-based cytoskeletal network, maintain pools of vesicles in the vicinity of the active zone in nerve cells (Figure 1.10).

In addition they are responsible for the SV release after a stimulus. At the presynaptic cleft they enhance the postdocking events such as priming and fusion possibly by interacting with the presynaptic cytoskeleton and/or inhibiting proteins that counteract the fusion process. After endocytosis synapsins promote the recruitment of the SV to the reserve pool [109].

Synapsins are associated with SV as peripheral membrane proteins that bind to lipid surfaces and to components of the cytoskeleton. Three different synapsin genes express protein variants with distinctly different C-terminal sequences mainly synapsin I, II and III. I focused on synapsin I, an 80 kD protein which has 5 different domains:



- A short N-terminal domain that features phosphorylation sites for protein kinases (A)
- a linker sequence (B)
- a large central C-domain that interacts with other synapsins for dimer formation and contains hydrophobic sites for the interaction with membranes. The N-terminal domains vary for the different synapsins except for the small conserved E-domain at the C-terminus, which controls the aggregation of vesicles. Only for the core (C-domain) a crystal structure is resolved by x-rays.

Synapsin has hydrophilic and amphiphilic regions and behaves like a surfactant at the air-water interface [110]. It interacts specifically with the negatively charged phospholipid moiety of the SV membrane as was shown by Benfenati et al [108]. In experiments with synthetic lipid membranes made of DOPS (dioleoyl phosphatidylserine), synapsin enhanced the membrane stability by forming a closed layer that covered large areas (several μm^2), which could not be penetrated with an AFM tip [111, 112].

2 Material & Methods

2.1 Chemicals and Lipids

1,2-Diphytanoyl-*sn*-Glycero-3-Phosphocholine (DPhPCPC), 1,2-Dioleoyl-*sn*-Glycero-3-Phosphocholine (DOPC), 1,2-Dipalmitoyl-*sn*-Glycero-3-Phosphocholine (DPPC) were purchased from Avanti Polar Lipids Inc., (Pelham, USA).

BSA was the pre-diluted standard from Pierce (Rockford, USA).

The mica sheets were purchased from Plano GmbH (Wetzlar, Germany).

All buffer substances, Poly-D-Lysine (70 – 150 kD) and 11-Mercapto-1-Undecanol were purchased from Carl Roth GmbH (Darmstadt, Germany), or from Sigma-Aldrich GmbH (Seelze, Germany) and were of reagent grade or better.

2.2 Buffers and Cantilevers

Buffers

The measurements with the SSM-sensor were done in HEPES-buffer: 30 mM HEPES, 140 mM NaCl, 2 mM MgCl₂, pH 7.4

The archae lipids and the DPPC were measured in the buffer of the last step of the extraction to which 100 mM of potassium chloride was added to screen electrical charges on the surface. 25 mM potassium acetate, 100 mM potassium chloride, pH 7.4 (KOH)

All experiments with the synaptic vesicles were done in glycine buffer: 300 mM Glycine, 5 mM HEPES, 0.02% sodium azide, pH 7.4 (NaOH).

Cantilevers

For the force-spectroscopy on the SSM-sensor and the synaptic vesicles were used NP-S, triangular silicon nitride probes with a nominal spring constant of 0.58 (N/m) from Veeco Instruments Ltd. (Mannheim, Germany)

In addition, the Biolever, rectangular silicon nitride probes coated with gold, nominal spring constant 0.006 (N/m) from Olympus Ltd. (Tokyo, Japan) was used for the synaptic vesicles.

For the archae lipid extract and DPPC were used Cont-W silicon probes, nominal spring constant 0.2 N/m from Nanoworld AG (Neuchâtel, Switzerland). Bimetallic effects, due to temperature variation are reduced with this cantilever. Silicon nitride probes coated with gold exhibit more drift, since the thermal expansion coefficients of the two materials are different and changes in the temperature lead then to an undesired bending of the cantilever.

2.3 Biological samples

2.3.1 Gold electrodes

The electrodes were prepared in the group of Klaus Fendler at the MPI of Biophysics in Frankfurt a. M.

The electrode shape was obtained by the use of an aluminum mask. A 5 nm thick chromium layer was evaporated onto the glass substrate as a basis for mechanically stable gold layers, and then a gold layer of 150 nm thickness was evaporated. The electrodes were rinsed with isopropanol and with distilled water and then dried with compressed air.

Diphytanoyl phosphatidylcholine (DPhPC: synthetic: Avanti Polar Lipids Inc. Pelham, AL) and octadecylamine (60:1, wt/wt, 98%, Riedel-DeHaen AG, Seelze-Hannover, Germany) were prepared 1.5% in n-decane according to a well established procedure [113] for the membrane.

Since gold is easily contaminated the electrodes were etched for 3 min in argon plasma prior to the insertion into an octadecyl-iosopropanol solution for 20 min to obtain the thiol monolayer. The electrodes with the assembled monolayer could be stored under a nitrogen atmosphere for several weeks before use.

DOPC (PC: synthetic: Avanti Polar Lipids Inc. Pelham, AL) was prepared like DPhPC for the outer leaflet of the lipid layer.

2.3.2 Tip functionalization

Silicon nitride cantilevers with a nominal spring constant of 0.3 N/m were inserted in the evaporation chamber of a Baltec MED20 (BALTECH, Balzers, Liechtenstein) and etched for 60 seconds with argon plasma at a pressure of ~ 0.02 mbar. Then a chromium layer of 3 nm thickness was evaporated, followed by a 20 nm thick gold layer, at a pressure of 2×10^{-5} mbar. After the procedure the cantilevers were inserted immediately into a 1 mM ethanol solution of 11-mercapto-1-undecanol for 12 h. They were afterwards rinsed copiously with ethanol and stored in ethanol until used.

2.3.3 Extraction of Methanococcus lipids

The lipid extract of the extremophile *Methanococcus jannaschii* was kindly provided by Sander Smits from the MPI of Biophysics, Frankfurt a. M.

The extraction followed a modified protocol of the Bligh and Dyer method [114, 115]. The freeze-dried pellet of the harvested cells was dissolved in 100 ml Tris-buffer and a mixture of Chloroform/Methanol 2/1 v/v was added. After overnight incubation at -20 °C the solvent mixture was separated from the aqueous phase with a separatory funnel and the solvents were partly removed. After a final filtering step the lipid extract was stored at -40 °C.

2.3.4 Sample preparation for Archae lipid extract

Liposomes are formed when dry thin lipid films are hydrated by an aqueous solution. The bilayer stacks swell until the lipid sheets detach under agitation and close to form multilamellar vesicles (MLV). Reducing the lamellarity and the size of such MLV's requires the input of energy in the form of sonication or extrusion. Since archaean liposomes are exceptionally stable and do not fuse or aggregate easily [116] an additional freeze-thawing step increases the size of the vesicles (50 to 500 nm) which enhances the probability of fusion for the formation of a bilayer on a hydrophilic support [117].

Archaelipid extract

100 μ l of the extract in a solvent-mixture of chloroform/methanol were transferred to a glasstube with an Hamilton-syringe. Both items were rinsed in chloroform before the procedure. Under constant rotation the solvent was evaporated under a stream of Argon gas until appr. 10 μ l of the mixture remained. Then 100 μ l of sodium acetate buffer, pH 7.4, 50°C was added and the glass tube was sealed and kept overnight at 0°C.

The solution was thawed the next day to room temperature to increase the size of the vesicles. 50 μ l of the solution were pipetted on freshly cleaved mica and after 30 min the sample was rinsed carefully and assembled into the liquid cell.

Formerly a total evaporation of the solvent was tried, but led to an insoluble lipid layer, which could not be hydrated again regardless of the use of different buffers at different temperatures.

DPPC

DPPC is a synthetic lipid with a phase transition temperature of $T_m = 41^\circ\text{C}$. It was used at a concentration of 5 mg/ml. Unless stated otherwise the preparation procedure was similar to the one used for lipid extract.

The solvent was evaporated under vacuum with a rotary evaporator and 100 μ l of sodium acetate buffer, pH 7.4 at 50°C added. The sample was kept on ice overnight and also thawed to room temperature. The vesicle solution was then subjected to 3 cycles of sonication (3 x 1 min) and 3 min incubation at 50°C to improve the subsequent fusion of the vesicles on the mica.

2.3.5 Purification of synaptic vesicles

The synaptic vesicles and synapsin I were prepared by Franco Onofri and Fabio Benfenati from the Institute of Experimental Medicine of the University of Genoa, Italy. Synapsin I was purified from bovine brain under non-denaturing conditions as described previously [118].

The protocol used to purify the synaptic vesicles was adopted from Huttner et al [106] and can be divided into six major steps, as shown in Figure 2.1.

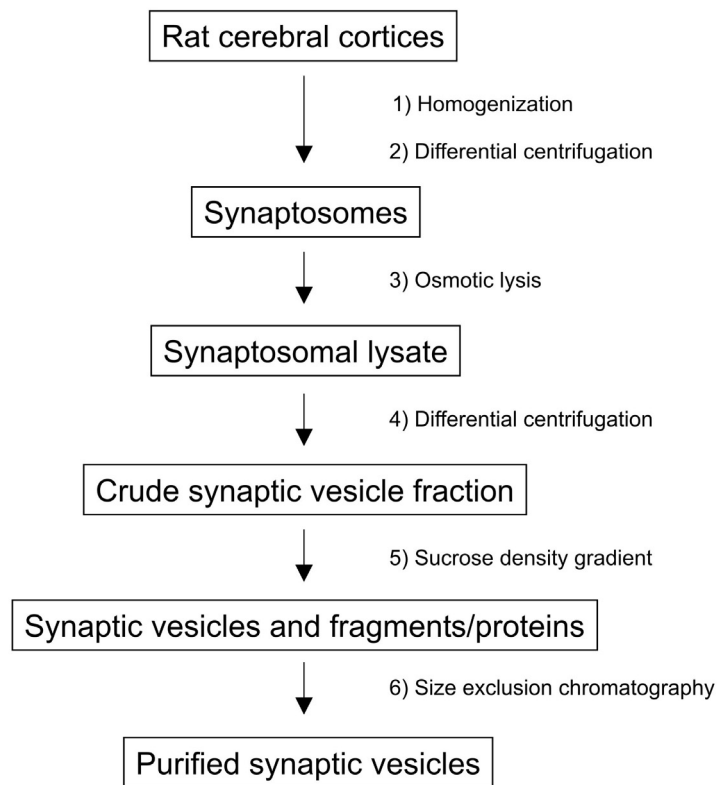


Figure 2.1 The purification of synaptic vesicles in six sequential steps

Isolated forebrains of rats were homogenized and finally purified through the step of controlled-pore glass (CPG) chromatography.

After elution, purified SVs were centrifuged for 2 h at 175 000g and resuspended at a protein concentration of 1-2 mg/ml in glycine buffer. Endogenous synapsin I was quantitatively removed from the synaptic vesicles by diluting them immediately after elution from the column with an equal volume of 0.4 M NaCl. After 2 h of incubation on ice, the vesicles were centrifuged for 2 h at 175 000g and resuspended in glycine buffer as described above. The extent of association of synapsins with SVs after this procedure was assessed by SDS-polyacrylamide gel electrophoresis and immunoblotting, as shown in Chapter 3.3.2.

2.3.6 Sample preparation for the synaptic vesicles

Freshly cleaved mica sheets (Plano GmbH, Wetzlar, Germany) were coated with poly-D-lysine (0.1 mg/ml, Sigma Aldrich), dried and then glued with superglue (UHU GmbH, Bühl, Germany) on specimen steel disks (Ted Pella Inc., Redding, USA). Afterwards, 50 μ l of a suspension containing synaptic vesicles at a protein concentration of 4 μ g/ml in glycine buffer were pipetted on such a disk, and the sample was incubated for 1 h on ice. The sample was thoroughly rinsed with glycine buffer to wash off the unspecifically adsorbed SVs and inserted into the AFM liquid cell for the measurements.

2.4 Methods

2.4.1 The Atomic Force Microscope (AFM)

With the invention of the scanning tunneling microscope (STM) in 1982 the era of the scanning probe microscopes started [119]. The basic principle is the scanning of the surface point per point with a probe and the assembly of the acquired data to an image. The interaction of the probe with the sample can be based on electrical (STM), mechanical (AFM) or magnetic forces (MFM), or can be a lightwave (NSOM) as well.

In scanning probe microscopes the piezo-tube scanners are widely used either to scan the sample under the tip or to scan the tip over the sample [120]. A piezoelectric material has the ability to either expand or contract according to a change in the crystal structure, when an external electric field is applied.

From the measuring of the tunneling current the inventors soon applied the STM set-up to introduce a tool for measuring forces between the tip and the sample. The device was a combination of the STM principles with the stylus profilometer. A profilometer contacts the surface with a diamond stylus at a certain force and by moving laterally detects height features on the surface [29]. In this new device the force acting between tip and sample was taken as a measure for the tip sample spacing.

The vertical tip was exchanged for a small lever, cantilever, whose deflection was measured by the tunneling current. Soon after optical methods were applied to detect the deflection of the cantilever with the so-called 'light-lever technique' or 'optical beam deflection'.

Atomic Force Microscope

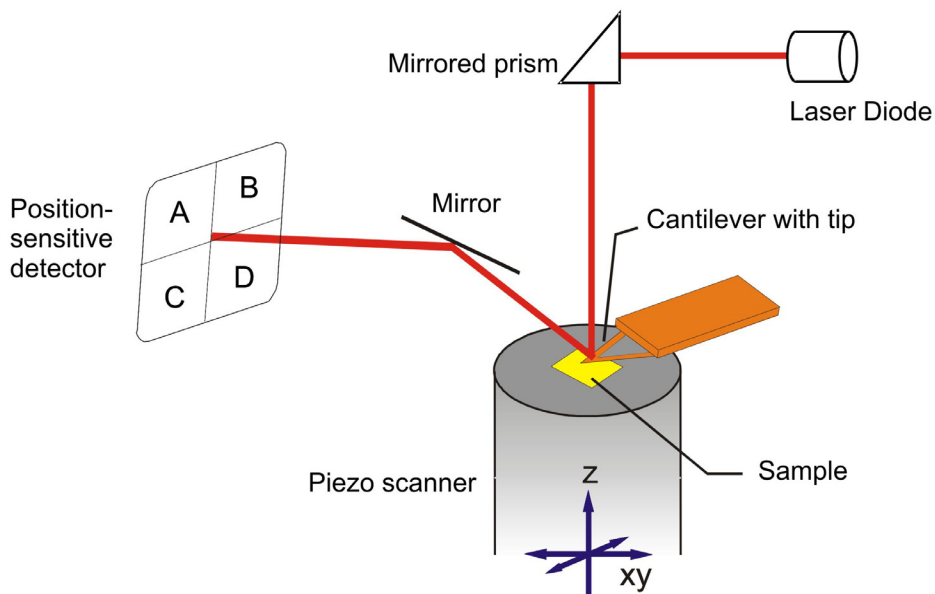


Figure 2.2 Principle of operation for a commercial atomic force microscope

Now the optical beam deflection method is most commonly used in commercial AFMs as it is sensitive, reliable and easily implemented [121]. A laser beam is focussed on the back of the cantilever and the deflection of the beam is detected with a position-sensitive detector, a split photodetector with four quadrants. The deflection of the laser beam is measured as the signal difference between the upper quadrants (A+B) minus the lower quadrants (C+D). To keep the force acting on the sample constant this signal is used to control the height of the piezo scanner via a feedback circuit by modulating the applied voltage such that the tip deflection remains constant. The height variation of the piezo scanner is thus a direct measure of the surface topography.

2.4.2 Imaging

To obtain images of the surface features of a sample the AFM can be operated in two modes.

Contact Mode

In the contact mode the deflection of the tip while scanning the sample surface is kept constant. A feedback loop is adjusting the voltage on the piezo scanner, and thus its extension, to keep the force constant. The vertical movement of the scanner at each data point is stored and converted to a topographic image while measuring.

Tapping Mode

For the tapping mode or 'intermittent contact mode' operation the cantilever oscillates near its resonance frequency with a certain amplitude. As the tip approaches the sample the amplitude is damped. This damped amplitude serves as a setpoint and is kept constant by the feedback loop. The vertical position of the scanner necessary to maintain the constant 'setpoint' amplitude is stored to form a topographic image of the sample.

2.4.3 Instrumentation

The NanoWizard™ AFM from JPK Instruments

The AFM manufactured by JPK (Berlin, Germany) is an AFM especially developed for life science applications, and is mounted on a standard inverted optical microscope. Therefore the scanner is positioned on top of the cantilever, which is mounted onto a glass block by a spring. The set-up allows for imaging large samples on glass-slides or in petri-dishes in liquid. The z-range is 15 μm and the area that can be scanned is 100 x 100 μm^2 . This AFM was used for the force-spectroscopy measurements on the SSM-sensor gold electrodes in chapter 3.1.

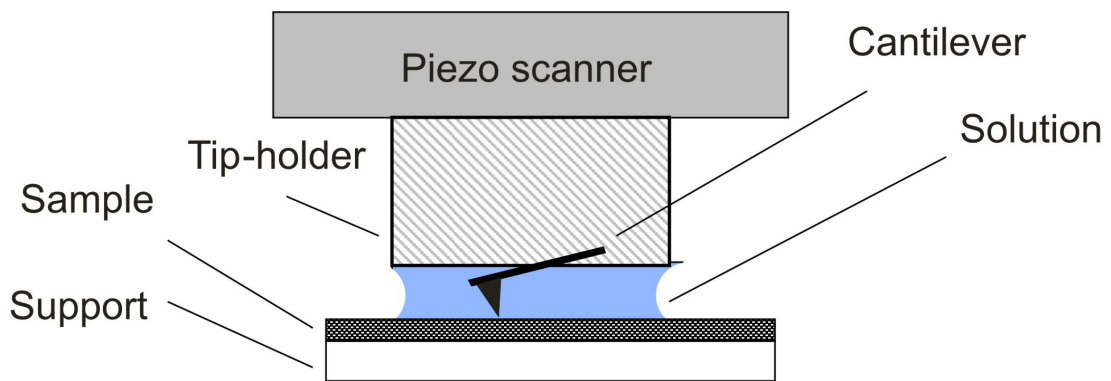


Figure 2.3 The set-up of the measurement in liquid with the NanoWizard™ AFM.

The Multimode AFM from Veeco

Images and force curves for the experiments in chapters 3.2 and 3.3 were acquired with a Multimode AFM with a Nanoscope IIIa Controller (Veeco Instruments Inc., Santa Barbara, CA) and the corresponding liquid cell. This AFM has a limited sample size of 12 x 12 mm². The scan area depends on the piezo scanner that is used and ranges from 1 x 1 μm² to 100 x 100 μm².

AFM images were acquired in contact mode at constant load, by adjusting the force to ~1 nN and using an E-scanner (range 12 x 12 μm²). The liquid cell is a cantilever holder made from glass and together with a silicone o-ring a chamber is obtained together with the sample surface. The cell has two openings for the exchange of buffer. This AFM was used for the characterization of the archae lipid extract, the DPPC bilayer and the synaptic vesicles.

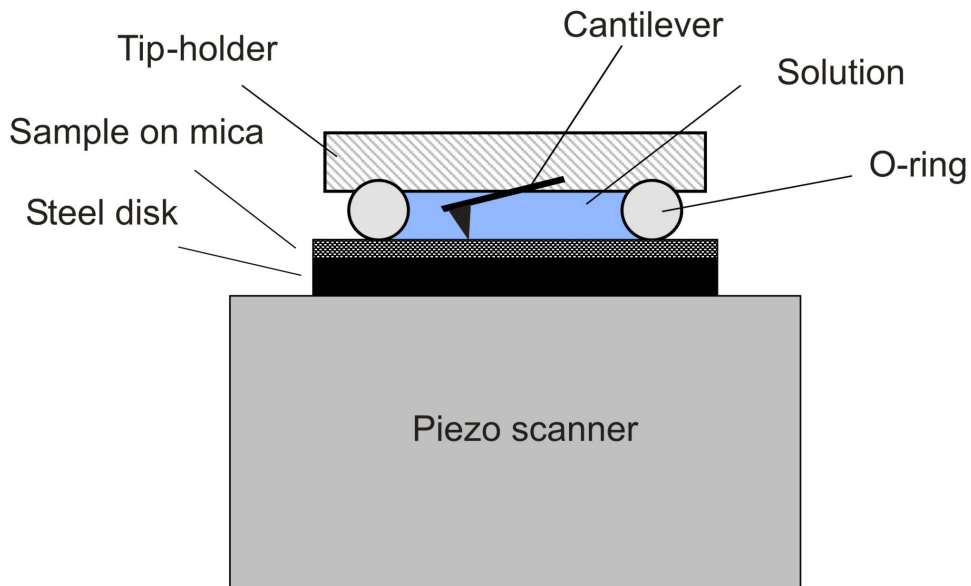


Figure 2.4 The liquid cell of the Multimode AFM

The heating stage of the Multimode AFM

The temperature-dependent measurements with the Archae-lipid extract and DPPC were done with the heater/cooler-system for the Multimode AFM. The components are a J-Scanner (xy-range 100 x 100 μm^2) with an internal scanner cooling system comprising a peristaltic pump and a water reservoir that can be put on ice to avoid overheating of the scanner piezos, a temperature controller and a peltier heater/cooler element.

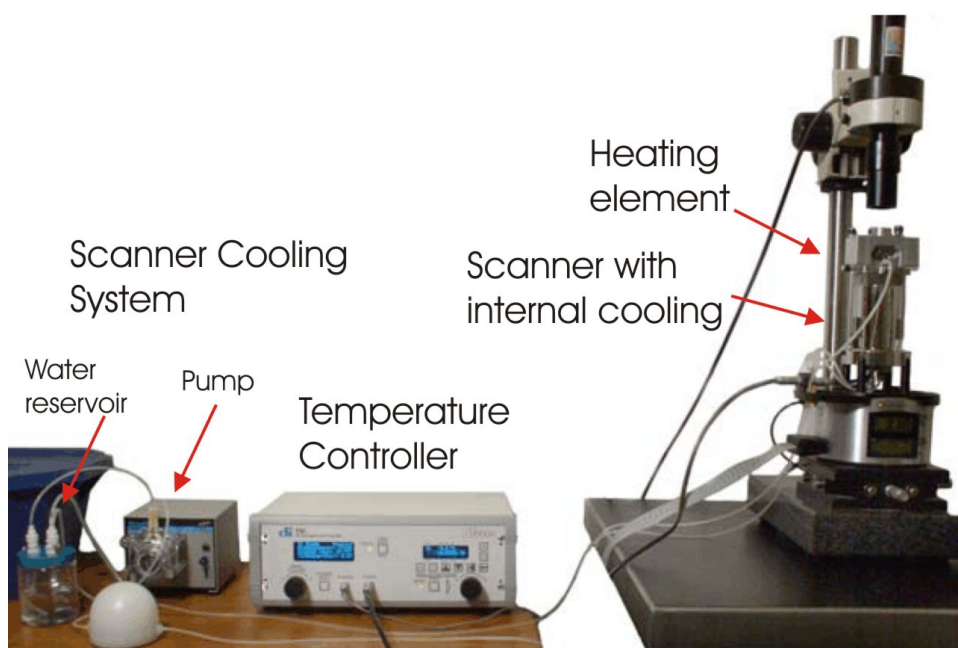


Figure 2.5 Set-up and components of the heating stage for the AFM Multimode.

The heater/cooler element has inside an Peltier (thermoelectric) element that is positioned under the tungsten (chemical element W, lowest coefficient of thermal expansion) cap and a thermocouple. The body consists of Delrin, a temperature resistant plastic, often used as a metal substitute. The heater/cooler is plugged into the scanner with the contact pins. The sample is deposited onto the cover and the liquid cell is assembled on top of it (Figure 2.6).

The heating stage was calibrated before the measurement with a temperature sensor, which was inserted into the liquid cell through a small hole at the top.

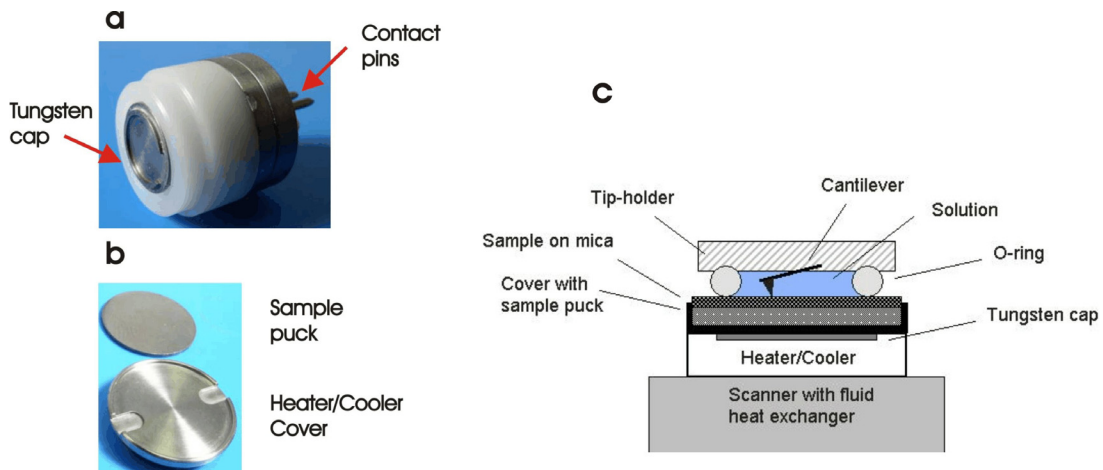


Figure 2.6 The heating element: (a) heater/cooler with a range from -35°C to 100°C , (b) the heater/cooler cover for the sample puck, (c) the heater/cooler assembled with the liquid cell

The difference between the measured temperature and the set temperature increased with heating and followed a linear relationship within the measured temperature range from 25°C to 50°C (Figure 2.7).

$$T_{act} \approx T_{room} + 0.58 * T_{set}$$

At room temperature the set temperature (T_{set}) is equivalent to the actual temperature (T_{act}), because there is no application of energy (heating). The increasing addition of energy (T_{set}) yields due to the energy coefficient of 58% a linear dependence of the actual temperature, which allows the extrapolation to other temperatures within the given range. As shown in Figure 2.6c the system contains several points for heat transfer to the environment between the peltier-element below the tungsten cap and the sample.

If the temperature was set to 70°C only 50°C were achieved inside the liquid cell, although heavy drifting started already to impair the measurement.

Especially the recording of force-distance curves was difficult. The drift lead to a constant change of the force either to lower or to higher forces, although a setpoint was adjusted. At set temperatures higher than 70°C the formation of bubbles and their attachment to the cantilever made proper measurements difficult. So reliable experiments could only be obtained up to a temperature of around 50°C .

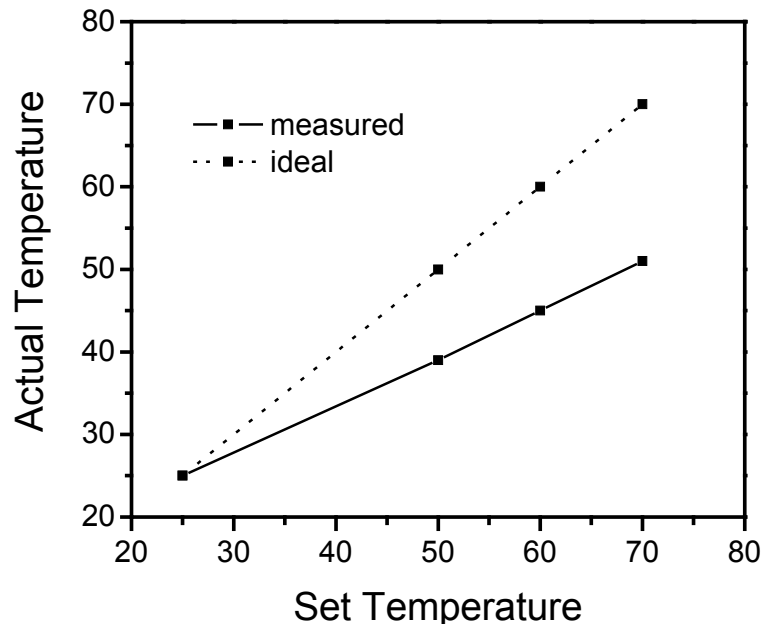


Figure 2.7 Calibration of the heating stage. The hysteresis between the set temperature and the actual temperature in the liquid cell increases linearly.

2.4.4 Force Spectroscopy

Interaction forces between tip and sample are studied by force spectroscopy. The sample is moved up and down by applying a voltage only to the z electrode of the piezo tube in a sawtooth pattern, while the cantilever deflection signal is monitored by the photodiode. Figure 2.8a shows a standard force curve including the tip sample movements. The force spectroscopy cycle starts at the right with the approach (red).

In the zero force regime the tip deflection is zero while the sample is approaching.

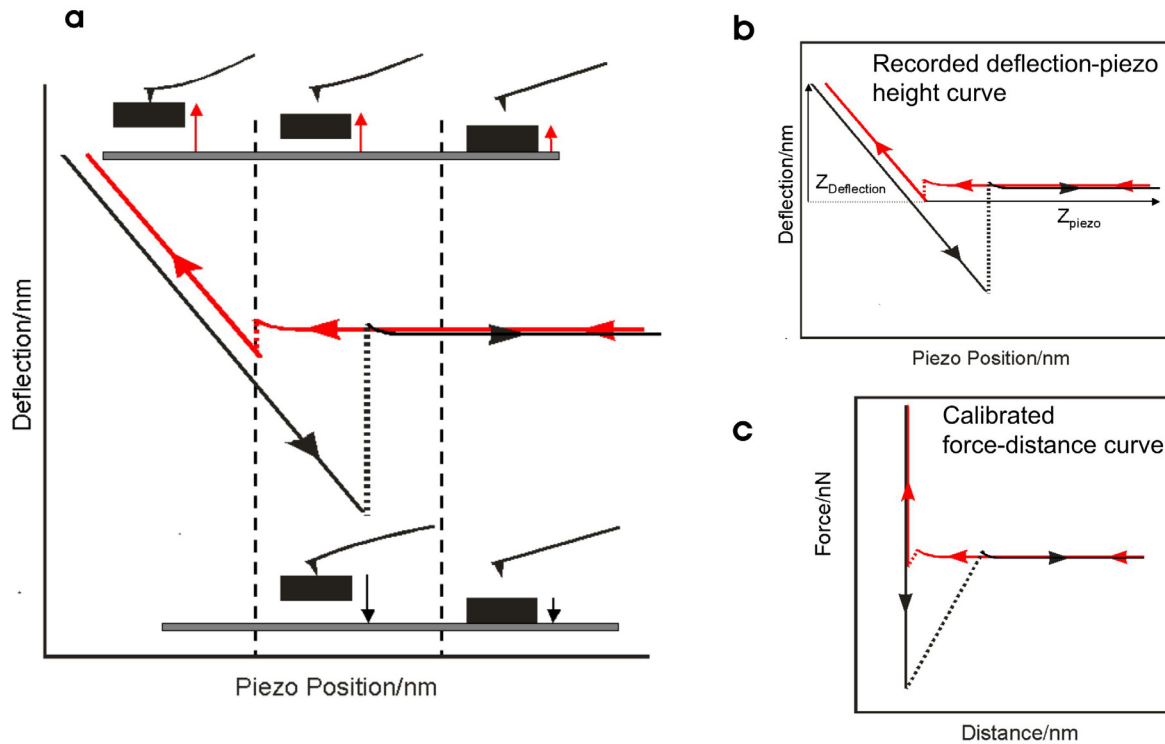


Figure 2.8 (a) The movement of the cantilever and the sample during force spectroscopy, approach (red), retraction (black); (b) Recorded curve; (c) Calibrated curve

Just before the contact point, the cantilever is deflected upwards by electrostatic repulsive forces until it reaches a distance where attractive forces dominate. The cantilever is attracted to the surface and ‘snaps-in’ to contact with the sample. The cantilever is moved upwards by the sample until a chosen setpoint is reached. In this regime of constant compliance the deflection of the cantilever and the movement of the sample are simultaneous.

The movement then reverses while the sample is retracting from the tip. The contact region of the retraction part is longer due to adhesion forces until the tip ‘snaps-off’ the surface. Adhesion keeps the tip in contact with the sample and leads to a negative deflection. The result is a deflection [nm] vs. piezo position [nm] curve of the cantilever movement which is converted to a force [nN] vs. distance [nm] curve by multiplying the deflection of the cantilever, $Z_{\text{Deflection}}$, with its spring constant, k_c , according to Hooke’s Law [122],

$$F = k_c Z_{\text{Deflection}}$$

to obtain the forces, F , and by adding the deflection of the cantilever to the position of the piezo, Z_{Piezo} , to obtain the distance D

$$D = Z_{Deflection} + Z_{Piezo} .$$

Additional mechanical information can be obtained from the contact regime between tip and sample. In Figure 2.9 two approach curves are shown. The slope of the bottom curve is linear in the contact regime due to an infinitely stiff surface that is non-deformable. The bottom curve represents the contact regime on a deformable surface like, e.g. a soft, biological specimen. The non-linear slope deviates from the ideal slope (dotted line). To obtain information on the mechanical properties of the sample it is necessary to measure the photodiode sensitivity with the same cantilever on a stiff surface [33, 123]. This difference in the slopes can then be used to calculate the stiffness of the deformable sample as will be explained in detail in chapter 3.3.4, in the context of the stiffness measurements on synaptic vesicles.

● Non deformable surfaces

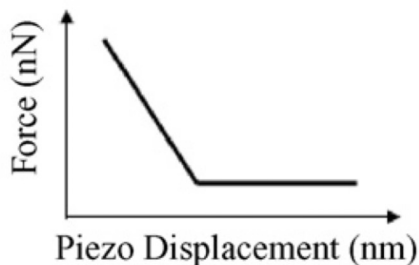
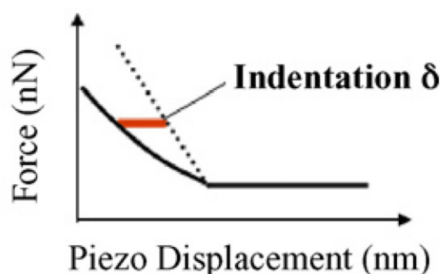


Figure 2.9 The two diagrams show the approach curves for non-deformable (top) and deformable (bottom) samples in the absence of surface forces. Graph from [123]

● Deformable surfaces



2.4.5 Force Volume Mode

The FV-mode is a method, where the tip of the cantilever scans the sample as in AFM imaging, and additionally acquires a force curve at each point of the two-dimensional array, into which the scan area is divided. The topographic information is recorded as the displacement of the piezo scanner needed to attain a certain cantilever deflection. Comparison of the topography with the force curves allows matching the surface features to the mechanical properties of the sample. The slope values of the array of force-curves are displayed in histograms which contain the peak for the slope values of the stiff substrate and one or more peaks for the softer slope values of the sample (explained in more detail in chapter 3.3.5).

2.4.6 Cantilever Calibration

The accurate spring constant of the cantilever is important for converting the measured AFM voltage signals into an absolute value of the force in Newtons. From the manufacturer nominal values are given, but due to material differences, manufacturing processes and environmental parameters the real values differ up to 30% around the given value. Several methods are known up to now for the calibration of cantilevers. They can be divided in geometrical methods, where the dimensions of the cantilever occur in the equations, thermal methods, which are based on the thermal noise spectrum of the cantilever, and static loading methods, where a calibrated cantilever is used as a reference to calibrate other cantilevers.

Cleveland Method or Added Mass Method

The first calibration procedure, published by Cleveland et al [124], is based on measuring the cantilever's resonance frequency unloaded and loaded with small masses of known weight (m_{eff}).

$$k = \frac{1}{2\pi} \sqrt{\frac{f}{m_{\text{eff}}}}$$

The shift in the resonance frequency (f), caused by the additional mass, gives the spring constant (k) of the cantilever. It is considered one of the most accurate, non-destructive methods, though time consuming for the attachment and removal of the masses at the end of the beam.

Sader Method (Geometrical)

The second method for rectangular cantilevers from Sader et al [125] incorporates the experimentally determined values of the resonance frequency ν_0 and the quality factor Q_f , together with the cantilever plan view dimensions in order to calculate the spring constant.

The surrounding fluid, typically air, is also considered in the calculations. The dimensions are obtained by optical microscopy whereas the resonance frequency and the quality factor are deduced from thermal noise spectra directly. This method is easy to implement but only applicable to rectangular cantilevers, which made it necessary to apply another method to assess the spring constant of v-shaped cantilevers also used in some experiments.

Reference Spring Method (Direct Method)

A third method used in this thesis is the 'static loading using two probes'.

The idea is to use a rectangular cantilever calibrated according to the method of Sader to obtain the stiffness of a second cantilever, which can be rectangular or V-shaped.

The reference cantilever is placed under the cantilever of interest. A force curve is taken on a hard substrate, the pyrex chip of the reference cantilever, to determine the cantilever deflection δ_{tot} directly from the piezo travelling distance. Another force curve is then taken at the very end of the reference beam. The flexibility of the beam leads to a different piezo travelling distance δ_{test} . This difference corresponds to the deflection of the reference spring.

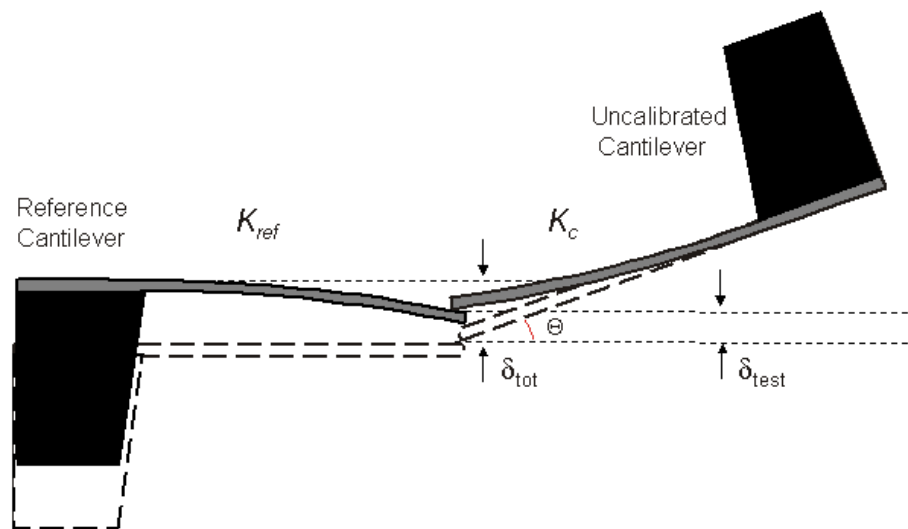


Figure 2.10 The Reference Spring Method: The cantilever with the unknown spring constant, K_c , is pushed against the reference cantilever with the known spring constant, K_{ref} .

With the known spring constant of the reference the spring constant of the cantilever can be calculated by

$$K_c = K_{ref} \left(\delta_{tot} - \frac{\delta_{test}}{\cos \Theta} \right)$$

with Θ indicating the angle between the two beams measured by optical microscopy. For commercial AFMs, this tilting angle is usually around 12° .

The advantage with this set-up is that the absolute variation of the spring constants is still between 10-20% but a precise comparison between several experiments is possible when the cantilevers are calibrated always with respect to the same reference cantilever[126].

The Thermal Method

The thermal method uses the thermal fluctuations of the cantilever positioned at a distance far from the sample. From vibrations near the resonance frequency of the cantilever, the spring constant can be determined according to the 'equipartition theorem' [127, 128]. Treating the cantilever as an ideal spring with the constant k , a measurement of the thermal noise $\langle x^2 \rangle$ determines the spring constant with

$$k = \frac{k_B T}{\langle x^2 \rangle}$$

However the cantilever is far from being an ideal spring and after a series of improvement the correct formula used now is

$$k = 0.8174 \frac{k_B T}{s^2 P} \left[\frac{1 - \left(\frac{3D}{2L} \right) \tan \phi}{1 - \left(\frac{2D}{L} \right) \tan \phi} \cos \phi \right]$$

where

- 0.8174 is a numerical factor for the geometry of the cantilever spring
- s is the sensitivity calibration factor in units of m/V
- P is the positional noise power in units of V^2 isolated from the fundamental resonant mode only
- D is the height of the tip
- L is the cantilever length
- ϕ is the tilt angle of the cantilever

Taking a force curve previous to the acquirement of the thermal noise spectra on a hard substrate and determining the deflection sensitivity from the region of constant compliance yields the calibration factor s .

The term in the brackets is usually close to unity and therefore its influence on the calibration is minor [129]. It is neglected in most calibration softwares of commercially available AFM devices.

2.4.7 Dynamic Light Scattering

One of the fastest methods available for the determination of the size of particles ($< 1 \mu\text{m}$) is Dynamic Light Scattering (DLS) also known as photocorrelation spectroscopy (PCS) or quasi-elastic light scattering (QELS). It is based on the Brownian motion of particles in a suspension. The set-up consists of three main components: an optical unit, a correlator and a computer. The optical unit comprises a laser as a lightsource, a sample holder, which keeps the temperature of the sample constant and a photomultiplier as a detector [48, 130].

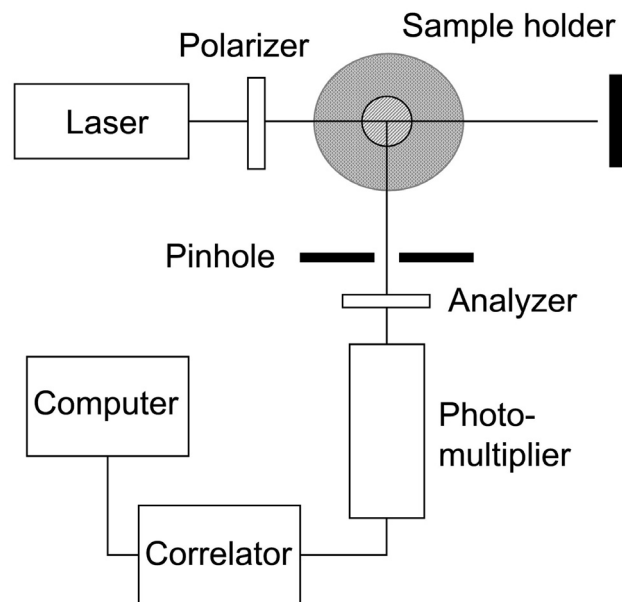


Figure 2.11 Schematic of the particle analyzer used for Dynamic Light Scattering

The diffusion velocity of the particles is measured to derive the diffusion coefficient. The hydrodynamic diameter, $d(H)$, of the particles is calculated with the Stokes-Einstein equation:

$$d(H) = \frac{k_B T}{3\pi\eta D}$$

k_B :Boltzmann constant; T: temperature; η viscosity of the medium; D: diffusion coefficient. The hydrodynamic diameter is the diameter of a sphere with an equivalent velocity of diffusion.

The method can only be applied to particles with a spherical shape and an expected monodisperse distribution. This method provides the possibility to measure biological samples non-destructively in their natural aqueous environment.

A Zetasizer 3000HS (Malvern Instruments Ltd., Malvern, UK) was used for all DLS measurements. The experiments were performed at 25°C, at a constant angle of 90°, and with a laser wavelength of 633 nm.

3 Results & Discussion

3.1 The Solid-supported Membrane (SSM) Sensor

In Chapter 1.5 I explained SSM-sensors similar to the one developed by Pintschovius et al [38]. Several publications [94, 131-133] and the development of a screening device by a company (Figure 1.8c) are proof of the functioning of the device. The analyte (transport proteins) in this system is applied by the adsorption of native membrane fragments or proteoliposomes on top of the supported bilayer. However the forces governing bilayer-bilayer interactions in solution are repulsive under physiological conditions, especially if both bilayers are composed of charged lipids [63]. Considering these interactions, the adsorption process of the proteoliposomes onto the SSM remains unclear and even more so when the system is subjected to several rapid solution exchanges (28 ml/min in a cuvette with a volume of 17 μ l). These processes are, however, not affecting the functioning of the system, as demonstrated by the functioning of the sensor.

This gave nevertheless rise to the speculation that this system could presumably exhibit a different interaction than was expected, e.g., unknown, attractive forces could act in the system.

For the investigation of the system with the force-spectroscopy mode of the AFM I developed a simplified approach. As a substitute for charged lipid headgroups an AFM tip was coated with gold and functionalized with hydroxy-terminated thiols (11-mercapto-1-undecanol) to mimic the membrane interaction of the proteoliposome with the solid supported membrane.

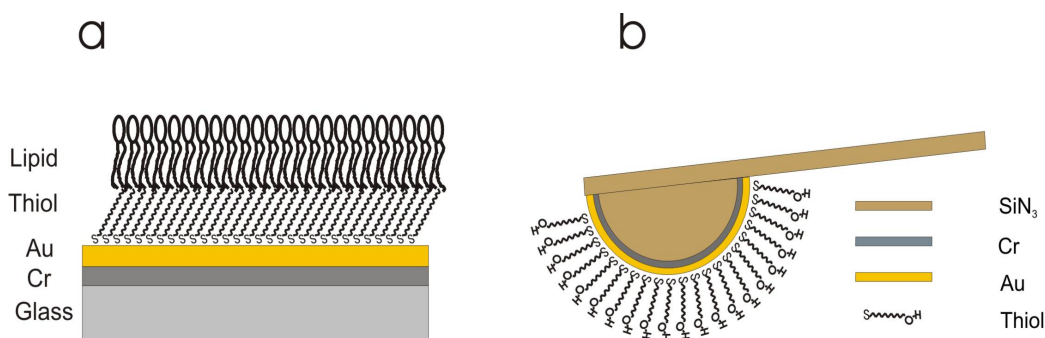


Figure 3.1 (a) Layers of the integrated membrane on the gold electrode of the SSM-sensor: Glass support (1 mm), a chromium layer (Cr, 5 nm), a gold layer (Au, 150 nm), an octadecanethiol monolayer (Thiol), a diphytanylphosphatidylcholine monolayer (PC), (b) Schematic of functionalized tip. The cantilever (SiN₃) was coated with layers of chromium (Cr, 3 nm) and gold (Au, 20 nm) by evaporation and functionalized with 11-mercapto-1-undecanol (Thiol).

3.1.1 Interaction between modified tip and bare substrates

Prior to the measurement I cleaned the glass plate with the gold electrode in argon plasma to remove organic contaminants and then directly covered with buffer. Gold is a strongly hydrophilic material with a theoretical value of the contact angle of 0. On a clean gold surface therefore a repulsion of the hydrophilic cantilever interacting with the hydrophilic surface would be expected. In reality gold, like surfaces of metals and metal oxides in general, has the tendency to adsorb adventitious organic material readily from the environment since this adsorbates lower the free energy of the interface [134]. Therefore the force curve exhibited a jump-in of the cantilever onto the surface indicating a weak attraction and a slight adhesion below 1 nN during the retraction before the tip was released from the sample. The surface was already contaminated although only 2 to 3 min passed between the removal from the plasma cleaner until the insertion in the buffer.

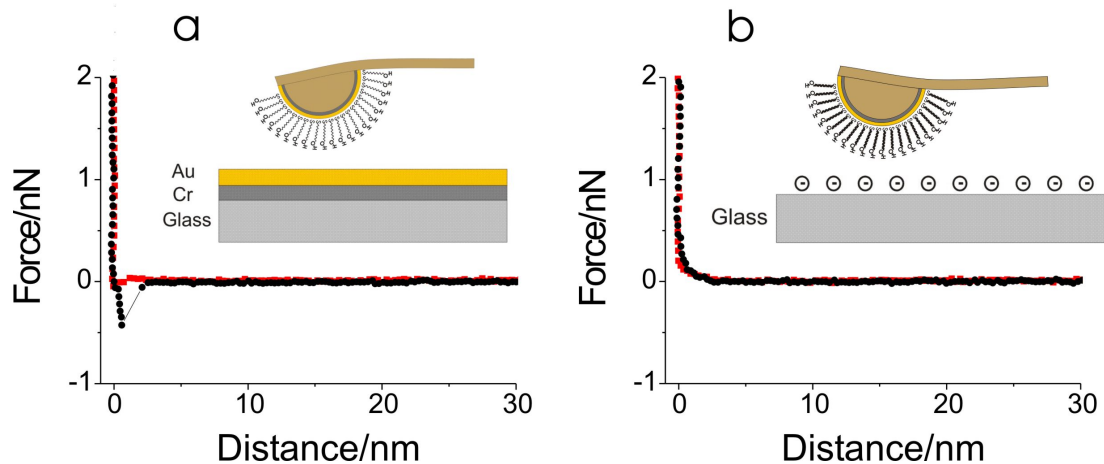


Figure 3.2 Force curves taken on the bare substrates: (a) the tip is attracted to the uncharged gold surface, (b) the tip is repelled by the charged glass surface

In order to check the integrity of the functionalized tip I took force-curves on the glass beside the electrode as a reference surface. Glass, as a charged surface, should lead to repulsion of the charged tip due to the hydration repulsion and the electrostatic double layer force.

3.1.2 Di-oleoyl phosphatidylcholine bilayer by vesicle fusion

First I assembled a bilayer achieved by vesicle fusion on the electrode from DOPC, a lipid with the same headgroup as Di-phytanyl PC for the comparison with the literature and to rule out the influence of this specific substrate.

The method of vesicle fusion to obtain bilayers in thermal equilibrium is well-known [135, 136] and yields typical force-curves as shown in Figure 3.3 [137, 138]. During the approach the tip is moved upwards by a repulsive force. This repulsive force can be fitted with an exponential function and the decay length lies usually in the range of 1 nm. The origin of the repulsive force acting on the cantilever is yet under debate and accounted for by hydration forces, electrostatics and the entropic protrusion effect caused by fluctuating, protruding lipid molecules.

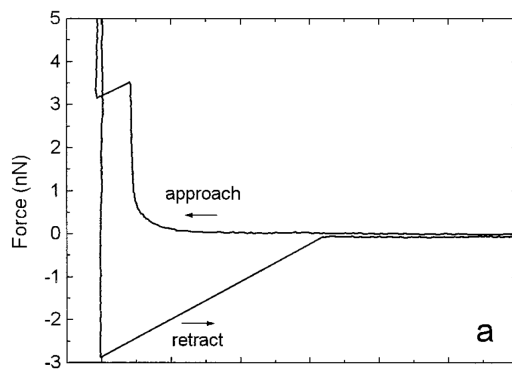


Figure 3.3 Force curve on mica after bilayer deposition. The bilayer is made from egg PC by vesicle fusion. Picture from [137]

Once a certain threshold force is exceeded (in this example 3 nN) an instability occurs and the tip penetrates the bilayer with a jump-in on the surface[139, 140]. The jump-distance corresponds to the thickness of the lipid film.

In order to compare the results from the integrated membrane system with the behaviour of a bilayer in thermodynamic equilibrium I formed a bilayer by vesicle fusion from DOPC (Chapter 1.5). After cleaning a gold electrode in argon plasma the vesicle suspension was applied and rinsed away after 10 min.

The expected, repulsive interaction of the modified tip with the glass was perhaps changed by the adsorption of some molecules from the vesicle suspension. It was possible to form a bilayer on the gold, although not as homogenous as on mica. The bilayer had a thickness of 3.7 ± 1.7 nm and the breakthrough occurred at a load of 3.5 ± 1.25 nN.

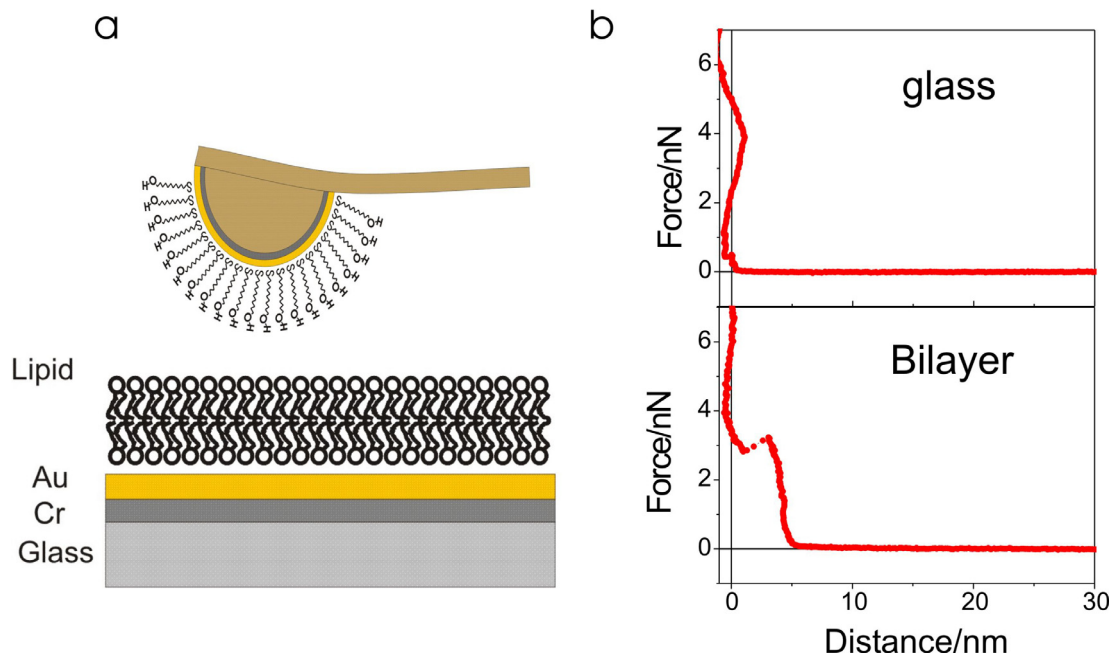


Figure 3.4 (a) Schematic of the DOPC bilayer on the gold substrate and the modified tip, indicating the expected repulsive interaction. (b) Force-curve taken on glass and on the bilayer. The repulsion, before the membrane is pierced at a force of around 3.5 nN, is clearly visible.

The big variance in the values was due to strong laser interference during the measurement as is visible in the curve taken on the glass substrate in Figure 3.4. On glass repulsion occurred, although a small adhesion event was present possibly caused by some contamination introduced with the vesicle suspension. Nonetheless I proved the possibility of spreading a bilayer on the gold and I showed the expected repulsion between the modified tip and the lipid to occur also with the gold substrate.

3.1.3 Comparing the thiol-layer with the glass surface

Subsequently I assembled the SSM system layer by layer and the interaction for each layer was measured with the functionalized tip. On each surface and for each layer I took a force-volume plot with 8x8 curves over an area of 500 x 500 nm². This approach gives also some information about the homogeneity of a layer.

The electrode was incubated for 20 min in 1 mM ethanolic solution of octadecylmercaptan to assemble the thiol monolayer on the gold. After rinsing in 2-propanol I dried the electrode under a stream of nitrogen and inserted it in the AFM liquid cell for measurement in aqueous buffer (30 mM HEPES, 140 mM NaCl, 2 mM MgCl², pH 7.4).

The adhesion force is displayed for the layers in Table 2. In all cases the interaction force on glass was nearly zero, whereas on the electrode a significant adhesion force of several nN was present.

This is an indication of a hydrophobic interaction between the tip and the thiols. Because thiols form strong covalent bonds with gold by their sulphur groups when assembling into a monolayer [141] they are presenting their hydrocarbon chains on the surface. The hydrophobic interaction is also present if only one surface is hydrophobic and the other is hydrophilic since the hydrophobic surface prefers to combine with any molecules to avoid the contact with water [67]. The extent of the interaction depends on the hydrophobicity of that respective surface [142].

In addition the tip was also attracted to the thiol monolayer on the gold surface, when approaching as shown in Figure 3.5. The snap-in of the tip onto the surface is clearly visible in the representative force-curve displayed.

Table 2: Adhesion values measured during retract from the thiol-layer in buffer, with the addition of decane measured in buffer and on glass as a control with the functionalized tip

	Control (Glass) [nN]	Electrode (Gold) [nN]
	DOPC / DPhPC	DOPC / DPhPC
Thiol in buffer	-0.13 ± 0.16 / -0.04 ± 0.02	-4.25 ± 3.16 / -1.38 ± 0.37
Thiol with decane	-0.11 ± 0.12 / -0.09 ± 0.07	-6.90 ± 2.31 / -1.37 ± 0.45

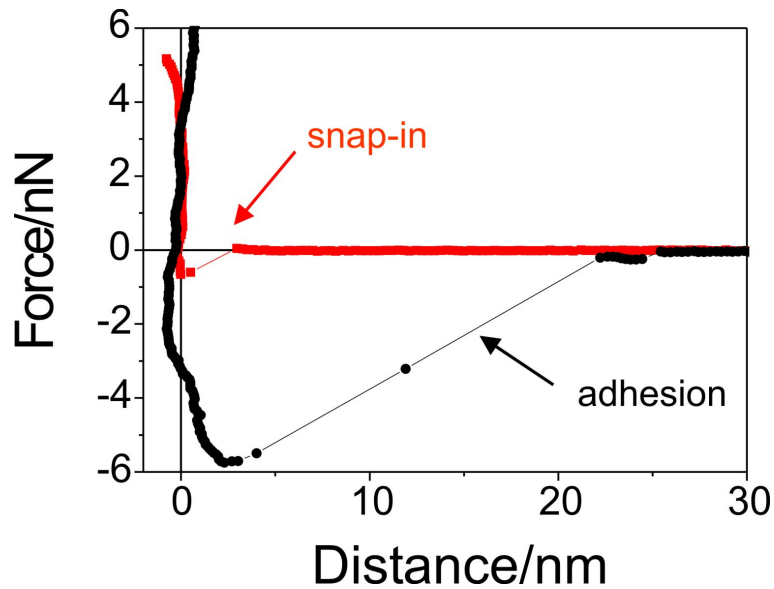


Figure 3.5 Representative force-curve taken for attractive forces between the thiol-layer and the functionalized tip. The tip is drawn into contact with the hydrophobic layer (snap-in) and is only released when a certain pull-off force is exceeded (adhesion).

Later I dried the electrode under a stream of nitrogen and added 1 μl of pure decane solution to check the influence of the solvent on the interaction. After 5 sec the electrode was immersed into buffer. The addition of pure decane to the system did not change the interaction properties significantly as shown in Table 2. Therefore the nature of the solvent is also not influencing, or even changing, the interactions between the different surfaces.

I checked the surfaces prior to the assembly of the final lipid layer for the DOPC dissolved in decane as well as for the DPhPC dissolved in decane.

3.1.4 Di-oleoyl phosphatidylcholine in decane

As an additional reference I dissolved DOPC in decane in order to use an unsaturated lipid in the setup, which allows the direct comparison with the force curves obtained for the bilayer made by vesicle fusion in chapter 3.1.2.

Until this point in the measurements the set-up of the SSM-sensor displayed the interactions expected between the individual layers and the functionalized tip, namely the repulsion for the charged surfaces (glass, lipid bilayers) and the attraction for the uncharged or hydrophobic surfaces (gold, thiol monolayer).

After the measurement of the interaction with the tip and the thiol layer I pipetted 1 μl of the DOPC solution (1.5% wt/v in decane) onto the electrode. The electrode was rinsed five seconds later with buffer and inserted into the AFM.

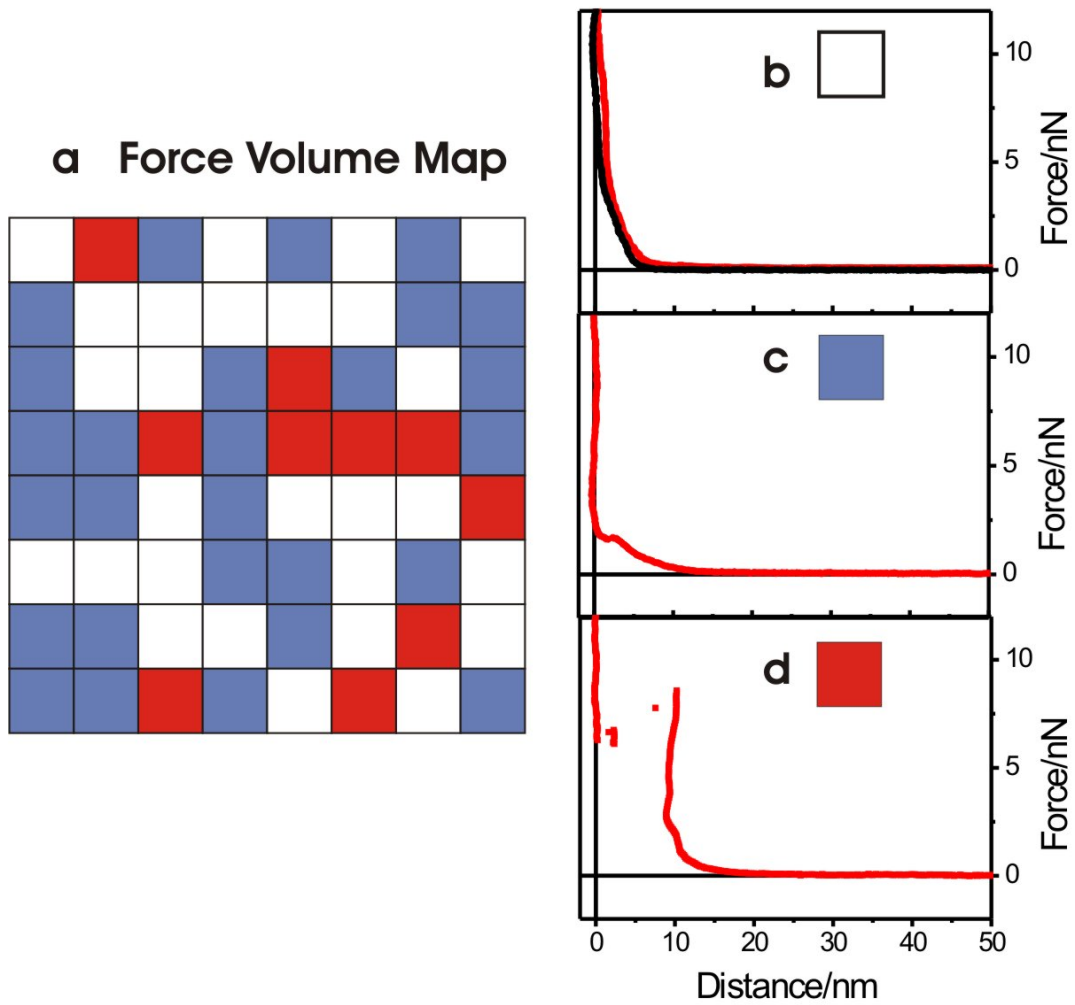


Figure 3.6 Distribution of three different force-curves over an area of 500 x 500 nm². (a) Map of the FV-Scan with different colours indicating force-curves that are repulsive (b, □), display a minor jump-in (c, ■) or an extensive jump-in (d, ■).

With the addition of DOPC the sample displayed the characteristics of a lipid layer regarding the repulsion of the charged tip. As indicated by the white squares approximately half of the curves showed only a repulsive interaction consisting of two different slopes (Figure 3.6b). A linear increasing slope followed by a steep slope that seems like an indentation of a softer layer followed by the region of constant compliance in hard contact. Considering the second type of force-curve (Figure 3.6c, blue square) which features a minor jump-in of appr. 1 nm of the tip into a layer it seems that a lipid layer was formed on the thiols. It was either an undefined assembly of the molecules or a very tightly formed single layer of DOPC molecules that can only be penetrated by the tip occasionally to some extent. According to the small breakthrough distance of 1 nm which corresponds well to the thickness of the headgroup region [143] the hydrocarbon chains could interdigitate with the thiols and only protrude by their headgroups from the layer or the hydrophobic decane is trapped between the hydrocarbon chains tightening the single layer of the DOPC molecules and only the region of the charged headgroups can be penetrated lacking the hydrophobic attraction.

However, at some spots at a force of 8 nN long-distance jump-ins occurred over 8 nm. Rarely they featured another small jump-in event at 1 nm distance indicating that the first layer is underneath. This would correspond to a stack of a complete bilayer of DOPC, which has a thickness of approximately 6.3 nm [143] on top of the afore mentioned, thin layer. The irregularity of the layer according to the different force-curves does not make this lipid a suitable candidate for reproducible and defined layers as the final coating of a membrane-based sensor, but I demonstrated its tendency to form a lipid layer with a repulsive interaction towards the hydrophilic tip, as demonstrated before by the vesicle fusion.

3.1.5 Di-phytanoyl phosphatidylcholine in decane

The original set-up of the SSM-sensor includes DPhPC as the outer leaflet on top of the thiols. To add the last layer, I pipetted 1 μl of the DPhPC-solution (1.5% wt/v in decane) onto the electrode and then after 5 sec immersed in buffer. After 5 min force curves were acquired on the electrode.

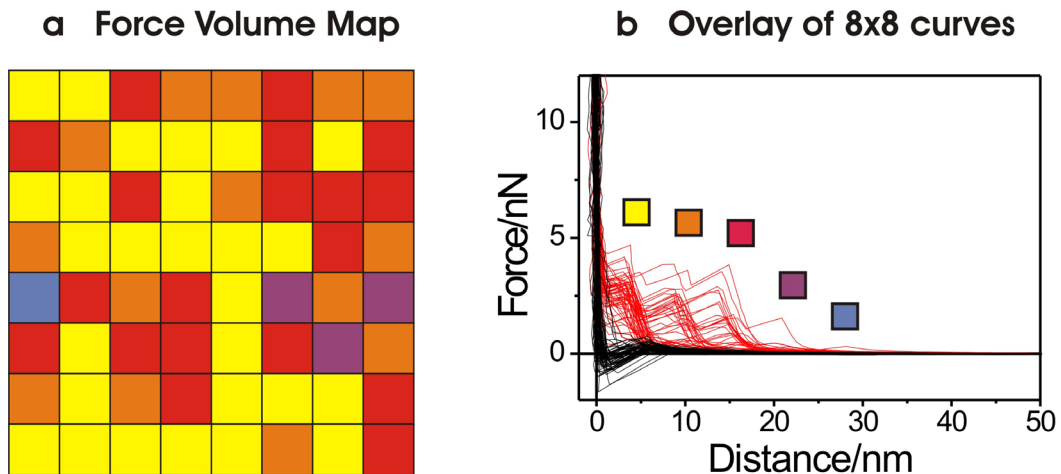


Figure 3.7 Distribution of the lipid stacks over an area of $500 \times 500 \text{ nm}^2$. (a) Map of the FV-Scan with different colours indicating the number of breakthrough events of the respective force-curve. (b) Overlay of 64 force-curves displaying a regular pattern of one (■), two (■), three (■), four (■) or even five breakthrough events (■).

The repulsion on the glass is unchanged, whereas on the electrode after a repulsive regime the tip overcomes a barrier and penetrates the membrane.

I tested the consistency of the lipid layer by taking a force-volume plot of 8×8 curves in an area of $500 \times 500 \text{ nm}^2$. The curves revealed a multilayer system with breakthrough events at appr. 3.5nm, 9nm, 14.9nm and 21nm. The distances are regular and similar for the events, even if one compares the curves with a different number of events between each other (Table 3). The respective breakthrough forces do not correspond to a similar pattern. In general the force decreases, the farther from the substrate the breakthrough events occur (Table 4).

The jump distance of the first breakthrough, as shown in Table 3, lay between 3.37 and 3.57 nm, which would account roughly for the calculated layer thickness of 3.2 nm of one DPhPC molecule. The following layers had thicknesses according to their breakthrough events starting with 5.14 nm for the second layer, 6.25 nm for the third and 6.1 nm for the fourth layer.

Table 3: Distances of the breakthrough events with DPhPC as outer leaflet

<i>Number of Breakthroughs [nm]</i>	1st Distance	2nd Distance	3rd Distance	4th Distance
1 (■)	3.37±0.73			
2 (■)	3.57±0.95	9.01±1.45		
3 (■)	3.39±0.60	9.10±0.63	14.89±1.14	
4 (■)	3.51±0.62	8.65±0.83	14.91±0.6	21.00±0.30

The two last values corresponded well to a thickness of 6.3 nm determined by x-ray scattering for a fully hydrated egg-phosphatidylcholine bilayer [144]. The reduced thickness of the second layer, which is presumably the first complete double layer, could be due to some ordering of the layer which could be caused by the following layers on top of it. The interaction via the headgroups of this first bilayer with the complete layer beneath it and the dispersed bilayer on top of it, could reduce the freedom of movement of the single lipid molecules in it and keep them in a more confined plane, in opposition to the bilayers on top of it.

Table 4: Forces of the breakthrough events with DPhPC as outer leaflet

<i>Number of Breakthroughs [nN]</i>	1st Force	2nd Force	3rd Force	4th Force
1 (■)	2.48±1.01			
2 (■)	2.49±0.98	1.05±0.64		
3 (■)	3.65±0.64	2.73±0.74	1.99±1.20	
4 (■)	3.19±0.31	2.36±0.28	1.59±0.38	0.76±0.68

All three bilayer systems exhibited the expected interaction between the modified tip and the lipid layers. Membranes of different quality and thickness were created, with the integrated membrane system of the SSM-sensor displaying the most homogenous coverage and a defined stacking of several bilayers.

Since I detected no attraction that could account for the interaction of the proteoliposomes with the lipid layer, the mechanism of adsorption on the DPhPC layer can only be explained with other mechanisms, than the chemical interaction between the headgroups.

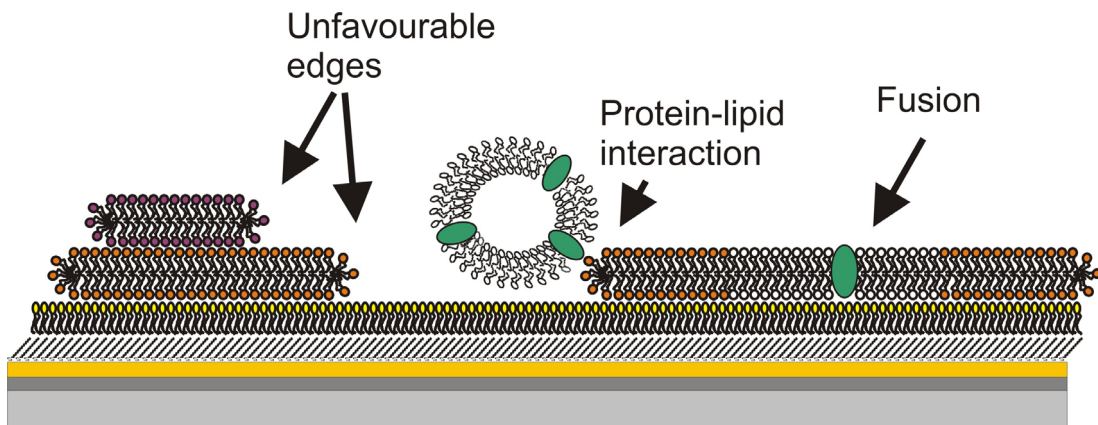


Figure 3.8 Schematic of the interaction mechanism between proteoliposomes and the SSM-sensor surface. The lipid stacks expose unfavourable edges, when the vesicles interact via the protein with the lipid headgroups the fusion between the vesicles and the lipid bilayers is favoured and the defects are filled with lipid bilayers incorporating the protein.

A possible way for the tight and permanent interaction between the proteoliposomes and the membrane could be now explained by the discovered stacking of bilayers.

The bilayer stacks comprising a full bilayer are distributed randomly on top of the outer leaflet of the integrated membrane. All of them expose their edges to the aqueous environment. At such edges the lipid molecules reorient to cap the bilayer. In that way the hydrophobic interior of the bilayer is protected from exposure to the medium, while the hydrophilic headgroups are in contact with the solution. These edges are energetically strained by their structure [145], and

therefore expected to promote the interaction with neighbouring material which could be vesicles from solution. Once they reach the SSM-sensor membrane, an interaction of the membrane proteins with the lipid headgroups could lead to a first attraction and near the edges the fusion of the proteoliposomes with the existing bilayer stack could be promoted. In such a case the whole area between the different stacks could be filled with additional membrane fragments that contain the protein that is to be measured. This is also supported by the fact that lipid bilayers and vesicles are, under certain circumstances, laterally mobile and once they reach additional edges, they coalesce into an even larger membrane patch [146]. Provided that the vesicle suspension contained enough material, a uniform layer could be formed. This layer would be kept together by the hydrophobic interaction between the lipids and withstand as a smooth surface also repeated flushing.

3.2 Archae lipids

Diphytanyl-based lipids and tetraethers, also referred to as bolaamphiphiles, have a range of application, from the manufacturing of liposomes as drug carriers to the assembly of membranes for sensors, due to their enhanced temperature stability and low proton permeability [39, 40]. For these applications usually only one lipid compound is used. The single compound is either isolated from natural sources or synthesized with similar features.

The aim of this experiment was to investigate the temperature dependent changes of a supported bilayer made from the total lipid extract of the extremophile *Methanococcus jannaschii* and to compare the findings with a supported bilayer made from a synthetic lipid, DPPC.

For the investigation of the archae lipid extract I chose the approach of the vesicle fusion. Other techniques for the formation of a lipid bilayer like, e.g. the Langmuir-Blodgett transfer, are not recommended, since this technique is highly influenced by any impurities in the solution, which are expected in a mixture of lipids directly extracted from cells.

3.2.1 Influence of temperature on a DPPC Bilayer

The absence of a phase transition in the archealipid extract is most clearly demonstrated by comparing the temperature dependence with that of a synthetic lipid that has a phase transition within the observed temperature range, such as DPPC ($T_m = 41^\circ\text{C}$).

I heated the vesicle solution to 50°C and the bilayer was fused in the liquid-crystalline state on the mica and then cooled down. I prepared the sample as described in chapter 2.3.4. and inserted it into the liquid cell of the AFM.

At 25°C the DPPC bilayer is in the gel phase. (Figure 3.9). The tighter packing of the lipid molecules in the gel-phase leads to defects between fused sections (white arrow in Figure 3.9) due to the lack of a reservoir of lipid molecules in the solution to fill the evolving holes [147].

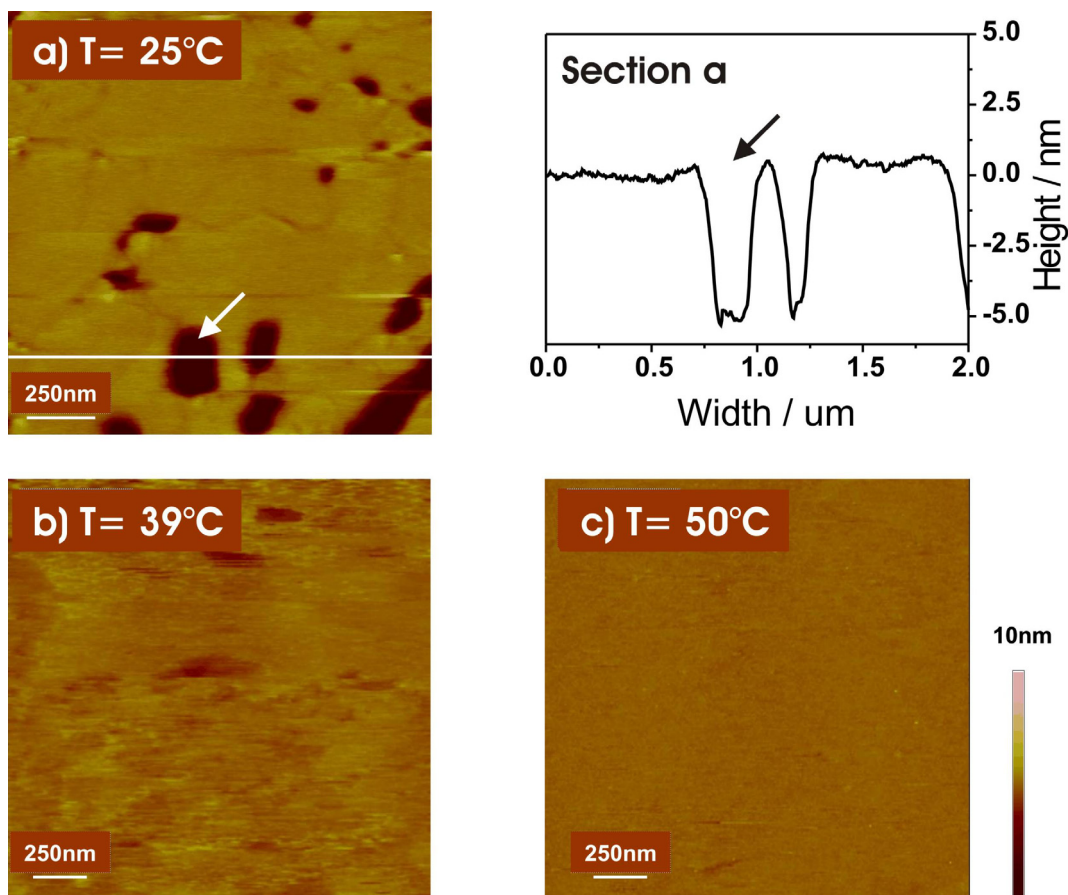


Figure 3.9 AFM tapping mode height images of the DPPC bilayer on mica. (a) at 25°C with a section of the bilayer and the arrows indicating a defect (section a), scansize 2 x 2 μm^2 , (b) at 39°C, scansize 3 x 3 μm^2 , (c) at 50°C, scansize 3 x 3 μm^2

The thickness of the layer was 5.5 nm from the cross-section of the AFM image (Figure 3.9a, Section a), similar to values from literature (Leonenko et al. 2004 [148], Garcia-Manyes et al. 2005 [43]). The force-curves taken at 25°C show only the repulsive regime. The bilayer was not pierced by the cantilever in our experiment (see Figure 3.10a). However at higher forces and with a stiffer cantilever (0.5 N/m) it is possible to pierce through the gel-phase as was shown by Garcia-Manyes et al for a DPPC-bilayer at 24°C. So the spring constant of the cantilever I used was with a stiffness of 0.19 N/m (determined with the 'Reference Spring Constant Method 2.4.6) to small to overcome the energy threshold at that temperature. However, I used the same cantilever to measure

the forces in the lipid extract, which were in some cases below 1 nN and which could not be measured properly with a stiffer cantilever.

Table 5: Forces and distances of the two breakthrough events in the force-curves taken on the DPPC bilayer

	25°C	39°C	42°C	50°C
Outer jump	Repulsion	16.27 ±0.99 nN	7.27 ±1.64 nN	4.42 ±1.32 nN
		8.68 ±0.41 nm	9.29 ±0.57 nm	8.74 ±0.91. nm
Inner jump		22.76 ±1.49 nN	15.04 ±2.05 nN	6.92 ±0.44 nN
		3.20 ±0.29 nm	3.55 ±0.36 nm	3.19 ±0.65 nm

I heated the sample in temperature intervals to 39°C, 42°C to 50°C and after one hour of equilibration, I took images and approximately 100 force curves.

At 39°C the fluidity of the lipid bilayer increased, as is shown in Figure 3.9c.

The sharp distinction between the holes and the bilayer was reduced. The resistance of the gel phase to the scanning tip led to a clear contrast between the features of the sample, whereas with increasing fluidity the tip encountered less resistance and the contrast was reduced.

As can be shown by the force curves taken on the lipid bilayer (see Figure 3.10b), the tip pierced the film at a force of appr. 23 nN (see Table 5). The occurrence of a second jump in this system could be due to lipid material picked up by the tip during the investigation of the gel-phase, since the onset of the outer jump started at 8.68 nm indicating the thickness of two bilayers. Both jumps penetrated the layers with a force above 15nN. It was not possible to distinguish between the break-through event on the layer or on the substrate.

The rise of the temperature to 42°C, thus close to the phase transition temperature, lead to a decrease in the force necessary to penetrate through the lipid bilayer by 35%. At 41°C the phase transition temperature of DPPC was reached. However due to the adsorption of the lipid bilayer onto the substrate the phase transition temperature was higher than the sharp transition peak found by Differential Scanning Calorimetry [148]. This was shown by Yang and Appleyard with DPPC coated mica and DSC [149].

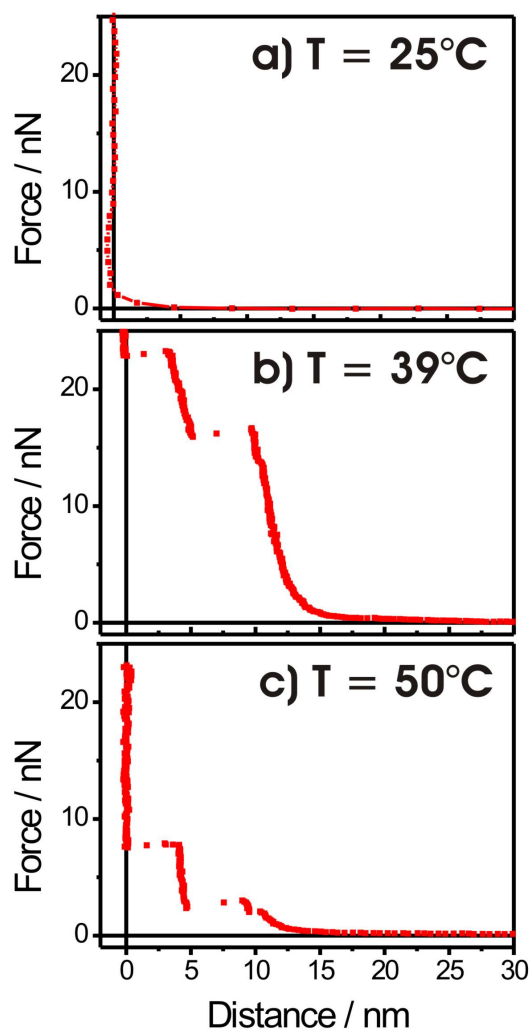


Figure 3.10 Representative force-curves for the heated DPPC bilayer

At 50°C the lipid bilayer reached the fluid regime and the rupture force fell below 7nN (Table 5). This observation is consistent with the data published by Garcia-Manyes et al. They obtained a minimum of the breakthrough force for the liquid-like phase which was between 5-7 nN.

The image shows no features as the tip was moving onto a fluid film, a feature also observed earlier for lipid bilayers in their fluid phase [111, 137, 138]. The force-curves showed even at this temperature two distinct breakthrough events.

Consequently the bilayer

reached the fluid regime, and simultaneously maintained a compact arrangement.

The inability to penetrate the bilayer in the gel-phase indicates a strong lateral interaction between the neighbouring molecules. Also the bilayer was formed in the fluid phase (which is a necessary condition for vesicle fusion) and while cooling down to the gel-phase holes appeared as defects in the bilayer due to a denser packing of the molecules. With increasing temperature the defects were filled again with lipid molecules as the bilayer reached the liquid-ordered phase. The packing density decreased again while the tip could also finally pierce the bilayer and the breakthrough force decreased further with rising temperature. This effect can be explained by the area per lipid value (A). In the gel-phase it is $A=47.9 \text{ \AA}^2$ for DPPC bilayers and $A=64 \text{ \AA}^2$ for the fluid phase [143]. A more

packed structure results in an increase of order and in an enhancement of lateral interactions between neighbouring molecules.

3.2.2 Methods for bilayer preparation from natural lipid extract

The first attempt to prepare a sample bilayer from the lipid extract of *Methanococcus jannaschii* was to apply the method of vesicle fusion. After drying the lipid extract under vacuum, it was not possible to dissolve the film with the addition of an aqueous solution even when the solution was heated. This led to the attempt of dropping the lipid/solvent solution directly into a buffer of 2 mM HEPES, 2 mM Histidin, pH7.3 while sonicating. I chose this buffer according to Fan et al.[150], as a buffer with low ionic strength for the formation of vesicles from thermophile lipids.

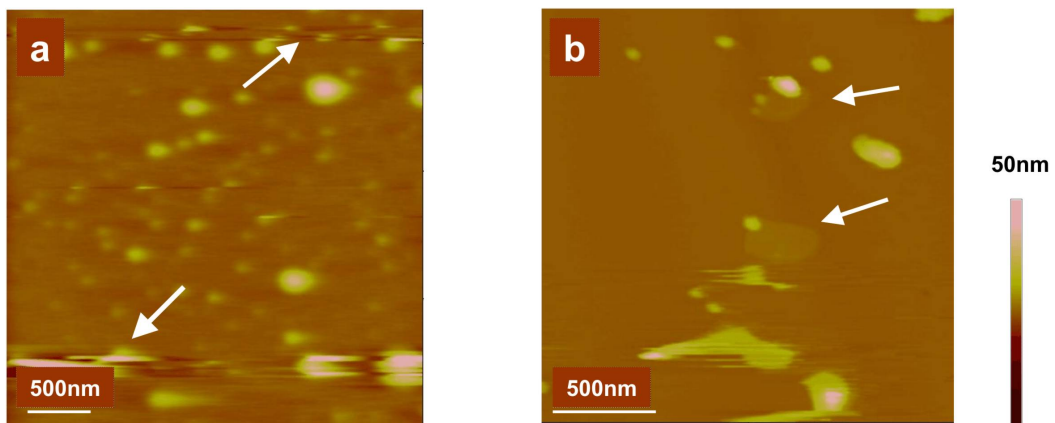


Figure 3.11 Vesicles of the lipid extract obtained by mixing the extract solved in chloroform/methanol (2/1 v/v) with buffer. (a) Vesicles between 5 nm and 30 nm diameter are obtained and instabilities during imaging occurred probably by moving vesicles (white arrows). (b) After 1.5 h some patches of only 1 nm in height formed (white arrows)

However as shown in Figure 3.11a vesicles of variable size (7 to 30 nm in diameter) were obtained without the formation of a bilayer. After 1.5 h (Figure 3.11b) some patches of 1 nm thickness formed, while other vesicles remained intact. Even the addition of a solution with 2 mM calcium did not help forming a bilayer (not shown). In addition the imaging conditions were not stable, either due to the movement of vesicles by the tip as shown for this measurement in Figure

3.11a (white arrows), or due to the instability of the mica. In some cases the solvent mixture apparently led to a deformation of the mica layer, probably by a reaction between the solvent that diffused between the epoxy glue and the mica sheet.

The final method that I established was the evaporation of 100 μl of the lipid/solvent mixture under a stream of nitrogen until only appr. 10 μl remained in order to prevent a total desiccation. The addition of sodium acetate buffer pH 7.4 yielded an opalescent solution, which was kept on ice overnight and thawed to room-temperature the next day (see chapter 2.3.4). This procedure was found to increase the size of vesicles, which then promotes their rupture on a charged substrate like mica.

3.2.3 Influence of temperature on natural lipid extract

After the insertion of the sample into the AFM liquid cell, I took pictures in tapping mode at 25°C. The blurred structures indicate an inhomogeneous fluid layer as would be expected of a mixture of different lipids owing to their probable assembly into islands and layers.

To verify the nature of the layer, I acquired force curves at several places of the samples. At 25°C the curves feature two breakthrough-events (jumps). The jump with the larger distance had a thickness of 4.09 ± 0.37 nm and occurs at a very small rupture force, 0.68 ± 0.14 nN. It corresponded to values measured for phospholipid double layers [138, 151]. The inner jump occurred at higher force, 3.35 ± 0.43 nN and with a thickness of 1.20 ± 0.24 nm (see Figure 3.12, Figure 3.13a and Table 6). The onset of the outer jump started at appr. 8 nm indicating a thickness that corresponds to two bilayers either on the surface or one layer on the surface and one at the tip. The thickness of 1.2 nm of the inner jump seemed too small for a complete double layer however the layer could be compressed between the tip and the support.

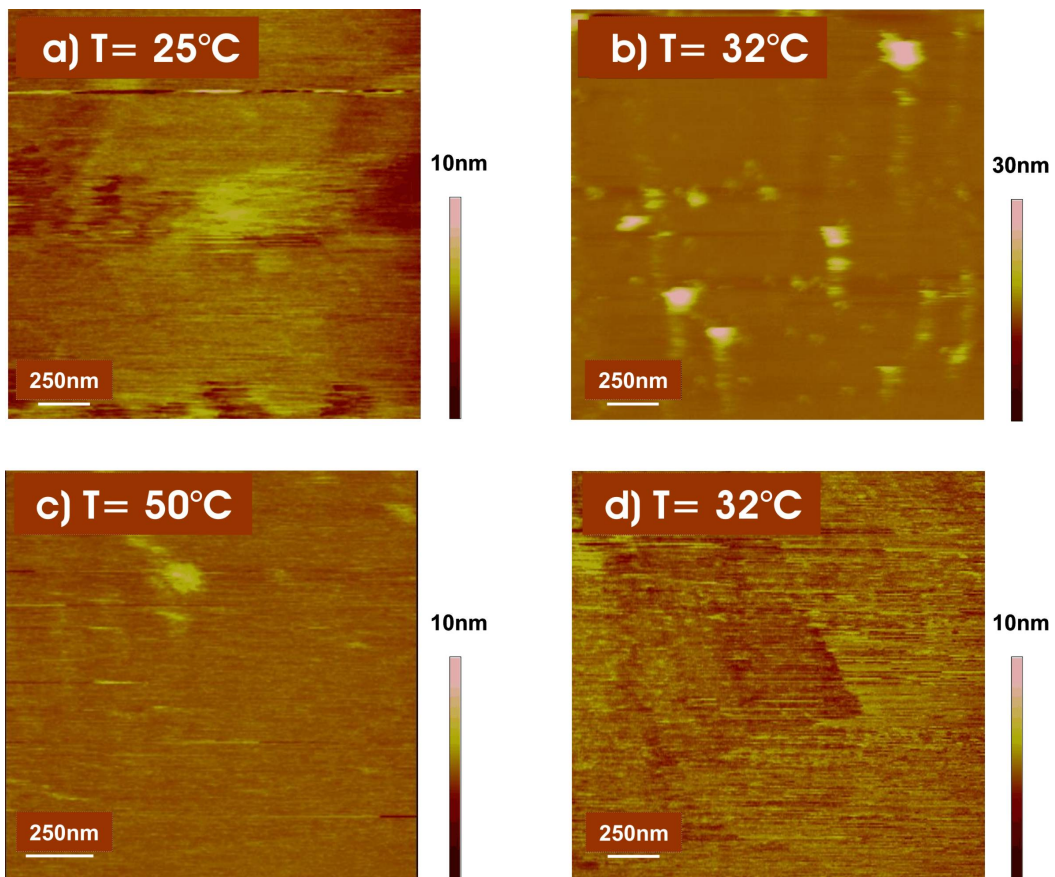


Figure 3.12 AFM tapping mode height images of the archaelipid extract. (a) at 25°C, scansize $2 \times 2 \mu\text{m}^2$, (b) at 32°C, scansize $2 \times 2 \mu\text{m}^2$, (c) at 50°C, scansize $1.5 \times 1.5 \mu\text{m}^2$, (d) cooled down to 32°C again, scansize $2 \times 2 \mu\text{m}^2$

Subsequently I heated the sample to temperatures of 32°C, 39°C, 45°C (not shown) and finally 50°C. After one hour of equilibration I took a set of pictures and approximately 100 force curves at each temperature.

At 32°C the surface displayed some round structures (see Figure 3.12).

Apart from the higher structures the lipid layer changed to a more fluid state as indicated by the force-curves. The rupture forces decreased by 8% for both jumps. This time the two layer thicknesses are more evenly distributed with 2.79 ± 1.56 nm for the outer and 3.13 ± 0.89 nm for the inner jump (Table 6). Comparing the force-curves at 32°C with those acquired at 25°C shows difference of thickness between the two jumps (Figure 3.13a and b). Seemingly the two layers reacted differently to the increase of temperature. The supported

layer resisted more to compression and was thicker, while the outer layer was compressed. The outer layer was more fluid than the underlying layer and compressed by the tip. This could be due to the lower layer coupling to the substrate, which orders the molecules additionally. This additional structuring made the layer below more resistant to phase changes, so higher temperatures were needed to obtain the same fluidity as for the upper layer.

The protruding structures could be small, unfused vesicles or aggregates of other membrane components, since the extract was used without removal of traces of proteins or sugars.

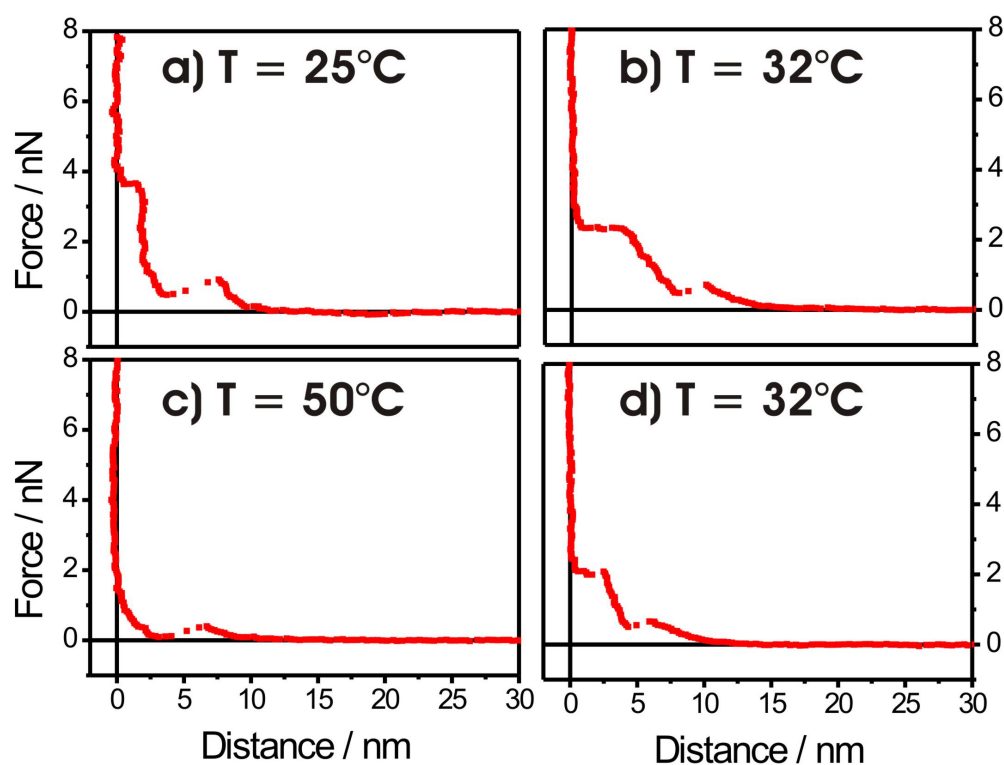


Figure 3.13 Representative force-curves for the heated natural lipid extract. The breakthrough force decreased with increasing temperature: 25° (a), 32°C (b) and 50°C (d) and increased again after cooling down the sample to 32°C (d).

Heating the sample to 39°C showed a further decrease of the rupture forces, and again the outer jump was smaller than the inner one (Table 6).

After heating the sample to 50°C the surface of the layer became more uniform and the protruding structures disappeared.

The force curves taken at this stage indicated a homogenous, very fluid layer with a thickness of appr. 8 nm. The curves can be divided into two classes: (i) curves featuring two jumps of similar width, 2.33 ± 0.82 nm and 2.09 ± 0.80 nm, with forces of 0.26 ± 0.07 nN and 0.49 ± 0.2 nN, and (ii) curves with only one jump at 0.42 ± 0.12 nN with a width of 3.51 ± 0.73 nm and an onset of the first repulsive force at 6.5 nm. The second jump was substituted for a repulsive interaction following the first jump (Figure 3.13c). However the forces of the two were smaller than for lower temperatures, so that I can say that the overall fluidity of the natural extract increased with temperature.

Table 6: Forces and distances of the two breakthrough events in the force-curves taken on the natural lipid extract

	25°C	32°C	39°C	50°C	back to 32°C
Outer	0.68 ± 0.14 nN	0.52 ± 0.18 nN	0.43 ± 0.17 nN	0.26 ± 0.07 nN	0.48 ± 0.10 nN
jump	4.09 ± 0.37 nm	2.79 ± 1.56 nm	2.81 ± 0.79 nm	2.33 ± 0.82 nm	2.36 ± 0.50 nm
(single				0.42 ± 0.12 nN	
jump)				3.51 ± 0.73 nm	
Inner	3.35 ± 0.43 nN	2.43 ± 0.25 nN	1.95 ± 0.74 nN	0.49 ± 0.2 nN	1.74 ± 0.27 nN
jump	1.20 ± 0.24 nm	3.13 ± 0.89 nm	3.89 ± 0.79 nm	2.09 ± 0.80 nm	1.97 ± 0.22 nm

A further heating was not possible, due to the generation of air bubbles in the aqueous solution. Moreover, the heat led to a drift of the cantilever, so that I could not reach stable, experimental conditions.

I checked the temperature-dependent change of fluidity also during a cooling of the sample, from 50°C down to 32°C. The measurement was started after an equilibration time of 90 minutes. The lipid extract remained fluid according to the images (Figure 3.12). As can be seen by the force-curves (Figure 3.13d) the rupture forces increased again back to the values obtained before at 32°C (Table 6).

The results showed a temperature-dependent behaviour of the lipid extract. The extract retained its fluidity throughout the chosen temperature range, the fluidity being higher at higher temperatures, which were close to the growing temperature of *Methanococcus jannaschii* (~ 50°C). No phase-transition of the lipid was observed in the studied temperature range between 25°C and 50°C.

It is also known that membranes of organisms are comprised of different lipid components like cholesterol which has an influence on the fluidity of the membranes of higher eukaryotes [152]. For prokaryotes and archae similar molecules exist and are called hopanoids [153].

A model mixture of the core lipids of *Methanococcus jannaschii* showed also no phase transition between 0°C and 120°C, when investigated with DSC [154]. This confirms our findings for the lipid extract. So the mixture of di-ether lipids, macrocyclic diether lipids and tetraethers (bolaamphiphiles) alone seems enough to account for the fluidity.

Comparing these observations with the results from the DPPC bilayer shows that in the extract the ordering seems to be reduced. This is a result of the different components like, e.g. the ether lipid cores and hopanoids, which have varying structures and thus cannot be ordered into a crystal-like structure. This reduced order and increased fluidity may be of physiological relevance, since maintaining the fluidity under a variety of conditions will ensure the survival of the organism.

Diether lipids and bolaamphiphiles are widely used as purified or synthesized lipids for their temperature resistance and stability in biotechnological applications but only as assemblies of one lipid compound. In nature a mixture of them is used to retain the necessary fluidity.

3.3 Synaptic vesicles

A number of AFM studies addressing certain aspects of synaptic vesicles have been published in the last few years. Parpura *et al.* imaged SVs purified from rat brain and sea-snail, having diameters ranging from 50 to 150 nm, on a polylysine-coated glass slide in contact mode, and found that the shape of the vesicles changed with the ionic strength of the buffer solution [155]. This was also shown by Garcia *et al.*, who imaged vesicles of the electric organ of the torpedo fish, having diameters ranging from 90 to 130 nm, in tapping mode [156]. Laney *et al.* analyzed similar vesicles by acquiring force curves in FV-mode in different buffer solutions, and found that Young's modulus increased upon addition of calcium to the buffer [157]. Other works dealt with the influence of acetaldehyde on synaptosomes [158], or monitored binding events between nerve terminal structures and proteins bound to the tip of an AFM cantilever [159, 160].

In this work I wanted to investigate the influence of synapsin I on the morphology, the mechanical properties and the aggregation mechanisms of synaptic vesicles (SVs).

Several studies were conducted showing that impairing the function of synapsin I either by antibody-injection into nerve cells [98] or by creating synapsin I knockout-mice lead to a decrease of synaptic vesicles on the synaptic cleft and as a consequence the release of neurotransmitter is highly disturbed [109]. The decrease of synaptic vesicles is giving rise to the speculation that the tethering of the vesicles not only creates storage pools for neurotransmitter, but also protects the vesicles against the degradation by metabolic processes of the cell.

Synapsin I could also confere additional mechanical stability to the membrane, making the synaptic vesicles more stable. As was shown by AFM studies in the case of clathrin for cellular vesicles or the S-layer proteins on the membrane of bacterial cells [47, 161]. The loss of synapsin I could also affect the general integrity of the vesicles and promote the fusion of the vesicles which would again submit them to degrading processes in the cell and explain the loss of vesicles without synapsin I.

3.3.1 Establishment of the AFM imaging conditions for SV

Synaptic vesicles (SV) can be considered as liposomes with proteins attached to the membrane. The adsorption of liposomes onto a suitable substrate for AFM studies is crucial. Biological samples are generally not imaged easily, which is due to their softness. The shear forces exerted by the scanning tip can cause deformation or even the destruction of the sample. Furthermore the substrate has to be chosen carefully for each individual sample, e.g. one has to find a balance between a sufficient immobilization of the liposome, while avoiding the flattening of the liposome to a bilayer caused by the surface energy of the substrate. Although SV are stabilized by their protein layer and do not flatten as readily as pure liposomes, the choice of the substrate has to be adjusted to the demands of the experiment.

For the investigation of the SVs with the AFM I assessed the optimum conditions for sample preparation and imaging. The requirement for my experiments was that the vesicles should not be displaced by the imaging process and remain intact after the probing with the tip.

SV have a net negative surface charge [162, 163] similar to cells. One of the most generally used substrates for AFM experiments is mica. Mica is a layered mineral of the aluminosilicate group, which splits easily in the direction of the crystal surface exposing a clean, atomically flat surface. Muscovite mica consists of SiO_4 molecules cross-linked by aluminium atoms with OH groups, although the strong negative charge is counterbalanced by K^+ -ions mica has a net negative charge in solution [164, 165]. Several research groups used mica as a substrate [158, 159] and added ions with a positive charge, such as Mg^{2+} , as a mediator [156, 157] between the negative charges of the sample and the mica for good adhesion.

Therefore I chose to use MgCl_2 ions as mediators between the negative charged SVs and the likewise negative charged mica as a first approach.

I diluted the vesicles to 4 $\mu\text{g}/\text{ml}$ with glycine buffer that contained 10 mM MgCl_2 to favour their adhesion onto the substrate. After one hour of incubation on freshly cleaved mica, I rinsed the sample three times with glycine buffer and inserted it into the AFM liquid cell. Glycine buffer was also used throughout the experiments. The pictures were made in the tapping mode under conditions

called 'soft tapping'. The ratio between the setpoint amplitude and the free amplitude of the oscillating cantilever A_{sp}/A_0 was between 0.95 and 0.1. Although the tapping mode is a non-destructive method the SVs were displaced during the imaging process, as is shown by the two white arrows at the bottom of Figure 3.14, or dragged several hundred nanometres, as shown at the top section in Figure 3.14. However the SVs that remained intact while imaging have the expected height of 40 to 50 nm and radii between 33 and 93 nm, reducing the measured values by twice the tip diameter of 26 nm. For the interpretation of the size of structures, that are imaged with the AFM, one has to take into account the effect of 'tip-convolution' [166]. The vertical dimension corresponds to the true height, while the lateral dimensions are augmented by approximately twice the tip radius, if tip and structures are of comparable size, which is equivalent to my experimental conditions.

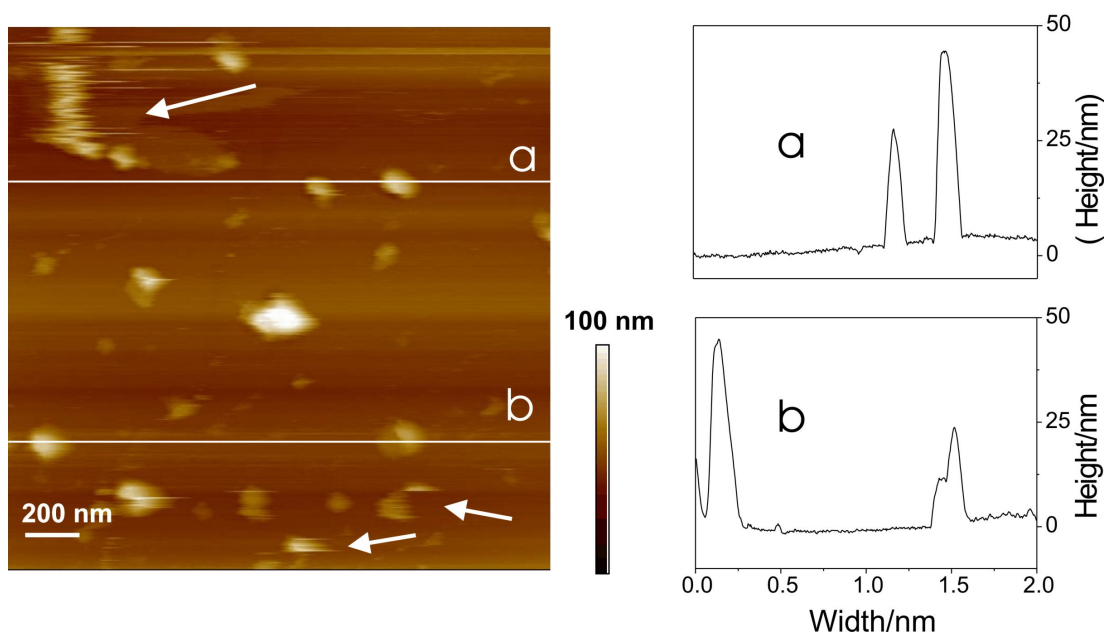


Figure 3.14 AFM tapping mode height image, scan size $2\ \mu\text{m} \times 2\ \mu\text{m}$ of SV on mica with Mg^{2+} as bonding agent.

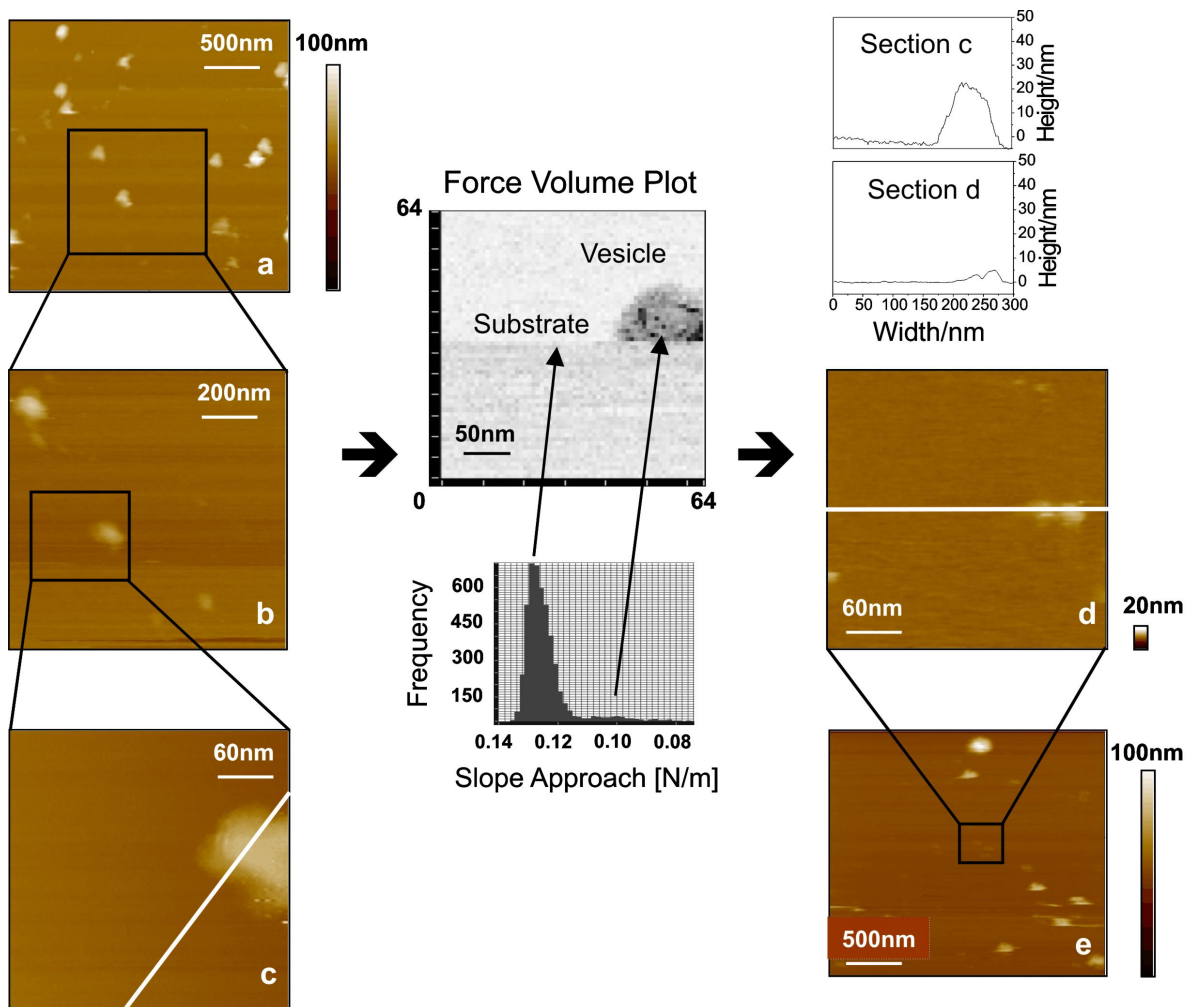


Figure 3.15 Series of AFM images and graphs summarizing the procedure of one complete stiffness measurement: (a) tapping mode AFM height image of unstripped vesicles on mica mode, size $2\ \mu\text{m} \times 2\ \mu\text{m}$; (b) Zoomed in image of two vesicles, size $950\ \text{nm} \times 950\ \text{nm}$; (c) tapping mode AFM height image before the FV-scan, size $300\ \text{nm} \times 300\ \text{nm}$; Image of a force volume plot with 64×64 curves and the histogram of the slope values; Sections of the vesicle before (Section c) and after (Section d) the FV-scan; (d) tapping mode AFM height image after the FV-scan, size $300\ \text{nm} \times 300\ \text{nm}$; (e) Zoomed out image of the area $2\ \mu\text{m} \times 2\ \mu\text{m}$, both vesicles were destroyed during the FV-scans

If some of the SV in the images were not moved, I recorded force volume plots. This specific mode of the AFM is only available in the contact mode. After imaging the sample in tapping mode and zooming in on single vesicles the AFM was switched to contact mode. A force volume plot was recorded and afterwards the AFM was switched back to the tapping mode to investigate the state of the vesicles after the procedure.

The whole procedure of one experiment is shown in Figure 3.15.

An image was recorded in tapping mode over an area of $2\ \mu\text{m} \times 2\ \mu\text{m}$.

The vesicles had an average height of 26 nm and a diameter of 93 nm after subtracting the tip radius (Figure 3.15a). They seemed to be flattened either by the tip during imaging or by the strong interaction between the vesicles and the substrate.

The image area was decreased to focus on two neighbouring SV (Figure 3.15b) and to record one force volume plot on each one separately. The stepwise decrease of the imaging area is recommended because of drifting.

Drift is a common problem during AFM experiments. The components are not directly coupled to each other so drift occurs in all three dimensions. It is caused by several factors: (i) the heating up of the microscope, the cantilever and the sample by the laserlight of the optical detection system, (ii) the drift of the scanner, when a higher magnification is chosen and the components have a time-lapse in the reaction to the software control and (iii) the silicone O-ring, when imaging in liquids, which can be deformed and therefore influence the scanner movement.

The desired structure was centered again with each zooming step and deviations from the central position were corrected, which compensated for the drifting of the system. Otherwise an area of $300\ \text{nm}^2$ without the feature of interest is imaged and the display has to be enlarged again. In Figure 3.15c a vesicle before the force volume scan is displayed. According to the cross-section, Section c, it has a height of 25 nm and a diameter of 80 nm.

The parameters for the following force volume scan were 64x64 curves over an area of 300 x 300 nm² at a force of 2.8 nN. With a speed of 4 Hz per force curve the recording takes appr. 30 min. In the force volume plot is the vesicle distinguishable by the difference of the slope values between the soft sample and the stiff substrate (chapter 2.4.4). The histogram of the slope values indicates the presence of two different values. The peak is the sum of all the substrate slopes at an value of 0.125 N/m. (For a quantitative analysis the slope values of the substrate are usually normalized to -1 and all other slope values are calibrated according to this value. However in this experiment only the uncalibrated values are mentioned to demonstrate the principle of the measurement and a detailed description is given in chapter 3.3.4). The small accumulation, that is discernible at 0.1 N/m, indicates lower slope values for the softer vesicle. A further evaluation was not possible. Qualitatively, I can show that vesicles are softer than mica without a quantitative assessment.

In addition, after the force volume scan the vesicle was either displaced or destroyed indicated by section d. The image taken afterwards of the area (Figure 3.15d) which is adjusted to a different data scale for the height information of 20 nm shows the remains of the measured vesicle. Both vesicles of Figure 3.15b were measured consecutively and as shown in the overview in Figure 3.15e destroyed. The imaging deformed other vesicles at the bottom of the image.

The deformation and displacement of the vesicles by the scanning tip due to the weak bonding with MgCl₂, necessitated a different substrate, which kept the vesicles in place and allowed an imaging process with the least deformation possible. A stronger bonding agent between the vesicles and the substrate was needed.

The fixation of cells or organelles for cytological examinations or immunostaining is often done with a poly-lysine coating on a charged substrate such as glass or mica. I adopted a protocol for the fixation of cells from Mazia et al. [167]. Mica was covered with a 10 mg/ml solution of polylysine and after 10 min the solution was removed and the substrate dried and stored at 4°C until further use. The SV solution, with a concentration of 4 µg/ml, was incubated on the substrate for 1 h and rinsed 3 times with glycine buffer.

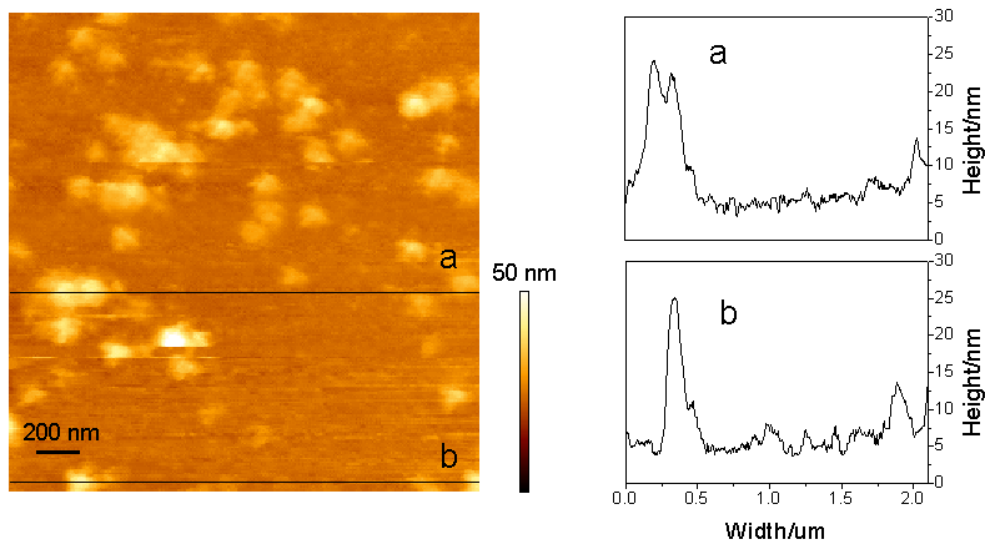


Figure 3.16 Image (Tapping Mode) of SV on mica coated with poly-lysine.

As an imaging mode I chose the tapping mode as suitable for soft biological samples. However the interaction of the silicon nitride tip with the polylysine lead to strong adhesions, which made it difficult to obtain images. If images were obtained, as shown in Figure 3.16, the vesicles seemed flattened. Due to the strong adhesion of the tip to the surface, the amplitude had to be increased until the tip could overcome the adhesion. This lead to a stronger tapping of the sample with the tip, so the SV were flattened and also lost their spherical shape. The adhesion between the polylysine and the tip could be due to some polylysine strands on top of the coating, which were not strongly adsorbed to the surface. They were picked up by the tip and thus lead to the unfavourable interaction.

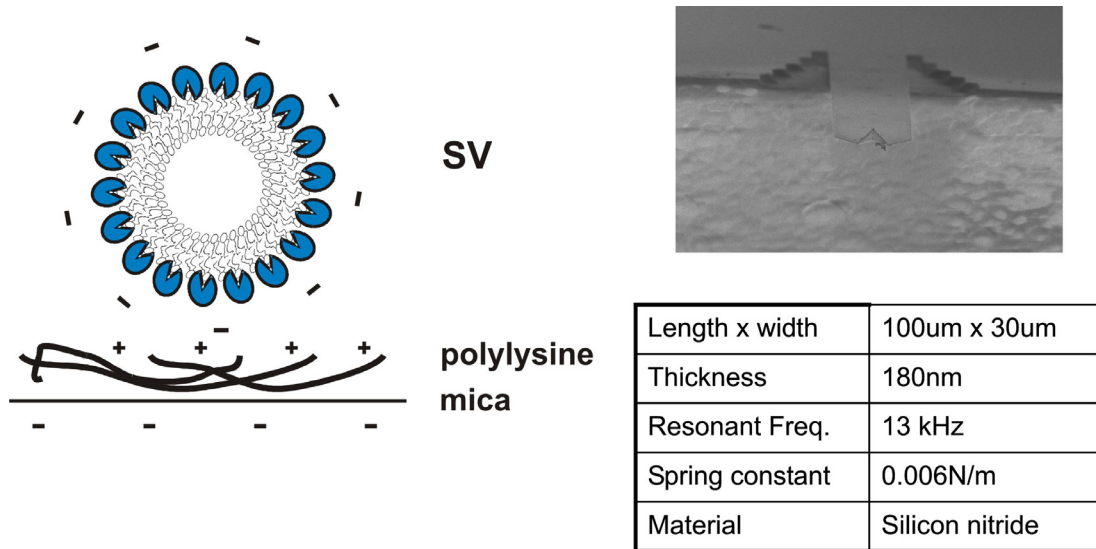


Figure 3.17 Established system for the measurement. Mica dip-coated with polylysine and adsorbed SV. Electron micrograph of a Biolever (Provided by Maren Müller).

I tried a more sophisticated method for the coating. It is derived from the coating of charged surfaces with polyelectrolytes [168]. Mica sheets were cleaved with a pointed needle and immediately covered with 150 μ l of a 0.1 mg/ml polylysine solution. After 5 min the sheets were immersed in a small container filled with distilled water and after one minute the procedure was repeated three times to desorb any loosely bound poly-lysine from the surface. The sheets were then left to dry and later glued onto an AFM specimen disk and stored at 4°C until needed.

In addition, I exchanged the silicon-nitride cantilever with a nominal spring constant of 0.3 N/m for the Biolever from Olympus with a nominal spring constant of 0.006 N/m. With such a soft cantilever, I tried again the imaging in contact mode, in contrast to the tapping mode I had used so far. The force setpoint was reduced to \sim 1nN, so that the deformation of the SVs was maintained at a minimum, as demonstrated in the following images.

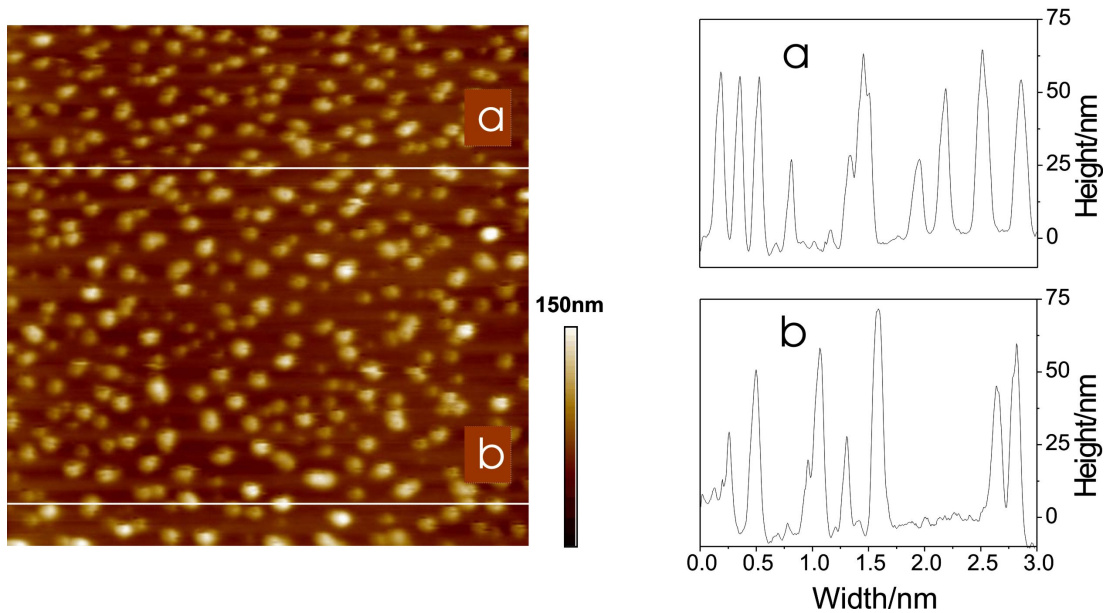


Figure 3.18 AFM contact mode height images, scansize 3 μm x 3 μm and sections (a, b). The SVs are homogenously distributed and not deformed by the scanning tip

The lower spring constant of the Biolever reduces the frictional forces exerted on the sample during the imaging in contact mode. So displacement or deformation of the soft sample is prevented.

The contact mode has the advantage that once the sample is equilibrated, which usually took more then 2h because of the soft spring, very stable imaging conditions could be achieved. The SVs had sizes between 25 and 70 nm.

The established experimental conditions made it now possible to investigate synaptic vesicles in detail and in a non-destructive manner.

3.3.2 Shape and size determination of native and synapsin-depleted SVs by DLS and AFM

I investigated the influence of synapsin I on synaptic vesicles by comparing native untreated synaptic vesicles (USV) purified from the rat forebrain (as described in 2.3.5) to synapsin-depleted synaptic vesicles (SSV) in order to mimick the synaptic vesicles of synapsin I knock-out mice. The preparation of SVs from knock-out mice is lacking the last purification step and therefore these preparations are not pure enough for AFM measurements. Tip artefacts are often introduced by the additional material in the solution, which does not adsorb properly onto the polylysine coating (results not shown).

Synapsin is reversibly associated with the SV membrane. It lacks the transmembrane regions that could mediate the permanent incorporation into the hydrophobic bilayer. The interaction between synapsins and the SV lipids is based on electrostatic interactions with polar headgroups and can be reversed by phosphorylation or by the increase of ionic strength [169].

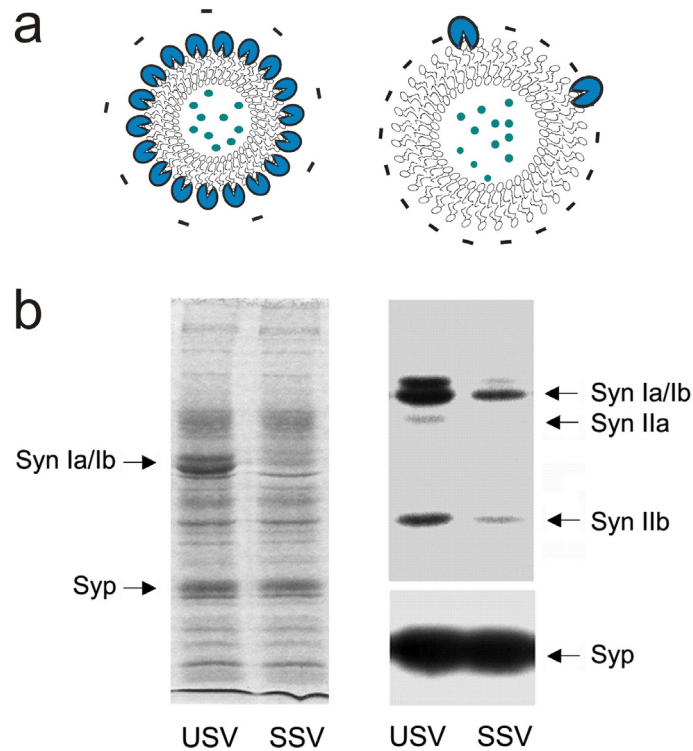


Figure 3.19 a: Schematics of the two investigated vesicle types. Left: untreated synaptic vesicle (USV) coated with synapsin (blue). Right: synapsin-depleted synaptic vesicle (SSV). b: Protein analysis of USV and SSV preparations (provided by Prof. Benfenati). Left: SDS-polyacrylamide gel. Arrows point to the synapsin Ia/Ib doublet (Syn Ia/Ib), inexistent in SSV and to the integral SV protein synaptophysin (Syp) as a control. Right: Immunoblot analysis of the same SV preparation with antibodies against all synapsin isoforms (Syn Ia/Ib, Syn IIa, Syn IIb; upper panel) and synapsotphysin (Syp; lower panel)

Therefore under a ionic strength treatment, like e.g., the dilution of the SVs in 150 mM NaCl synapsin dissociates from SVs. Up to 90% of the proteins are removed from the organelle membrane by the procedure [106]. Figure 3.19a shows a schematic of the two investigated vesicle types. After the preparation, aliquots (10 µg protein) of both vesicle types were analyzed. The SDS polyacrylamide gel on the left side in Figure 3.19b shows the separated proteins of both vesicle types (9% acrylamide in the resolving gel, stained with Coomassie brilliant blue).

The synapsin Ia/Ib doublet at 80 to 86 kDa (Syn Ia/Ib) removed from the SSV is indicated by the upper arrow in the left lane. The lower arrow points at the protein band of synaptophysin (Syp) at 38 kDa, an integral membrane protein which is not removed by the ionic strength treatment and therefore visible in both lanes. The adjacent immunoblot analysis shows the same SV preparations using antibodies specific for all synapsin isoforms (Syn Ia/Ib, Syn IIa, Syn IIb) and for synaptophysin (Syp).

Dynamic Light Scattering (DLS)

A fast method to determine the size of spherical particles in solution is dynamic light scattering (Chapter 2.4.7). The viscosity of the glycine buffer was compared with water before the DLS measurements. The buffer contains 300 mM glycine, which could lead to a change in viscosity. With rheology the deformation and flow of matter under applied stress is studied [170].

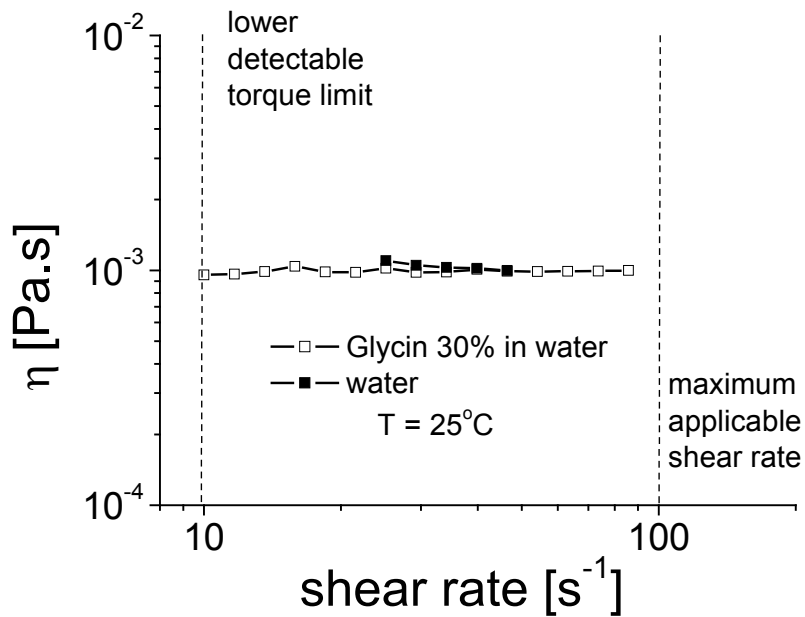


Figure 3.20 Result of the rheology measurement of water (□) and glycine buffer (■). Torque limit = limit of rotational force. (Provided by J. Vittorias)

Therefore a rheology measurement was performed, which showed that the viscosity was not different from water (Figure 3.21).

Both vesicle types were diluted at a protein concentration of 75 $\mu\text{g/ml}$ in 200 μl Glycine buffer and their size was determined by DLS.

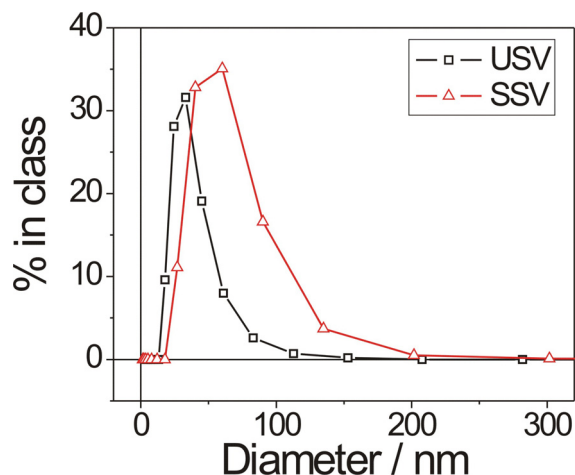


Figure 3.21 Size distributions of USV (black) and SSV (red) in solution determined by DLS

The data in Figure 3.21 show that USV had diameters ranging from 25 to 45 nm in solution, with a smooth decline towards 150 nm, indicating either the presence of larger SVs or the formation of some vesicle clusters. The SSVs had, other than the USVs, a larger diameter in the range of 40 to 70 nm. The curve declines towards 200 nm, also indicating bigger SVs or assemblies of several smaller SVs.

AFM

Both vesicle types were incubated on the polylysine coated mica in a dilution of 40 $\mu\text{g/ml}$ and bound electrostatically to the polylysine layer. The AFM tip did not disrupt neither during the imaging nor during the force curve acquisition the firm contact made by the interaction. In Figure 3.22 representative contact mode images of the two vesicle types, acquired with the same tip, are shown together with the cross-sections.

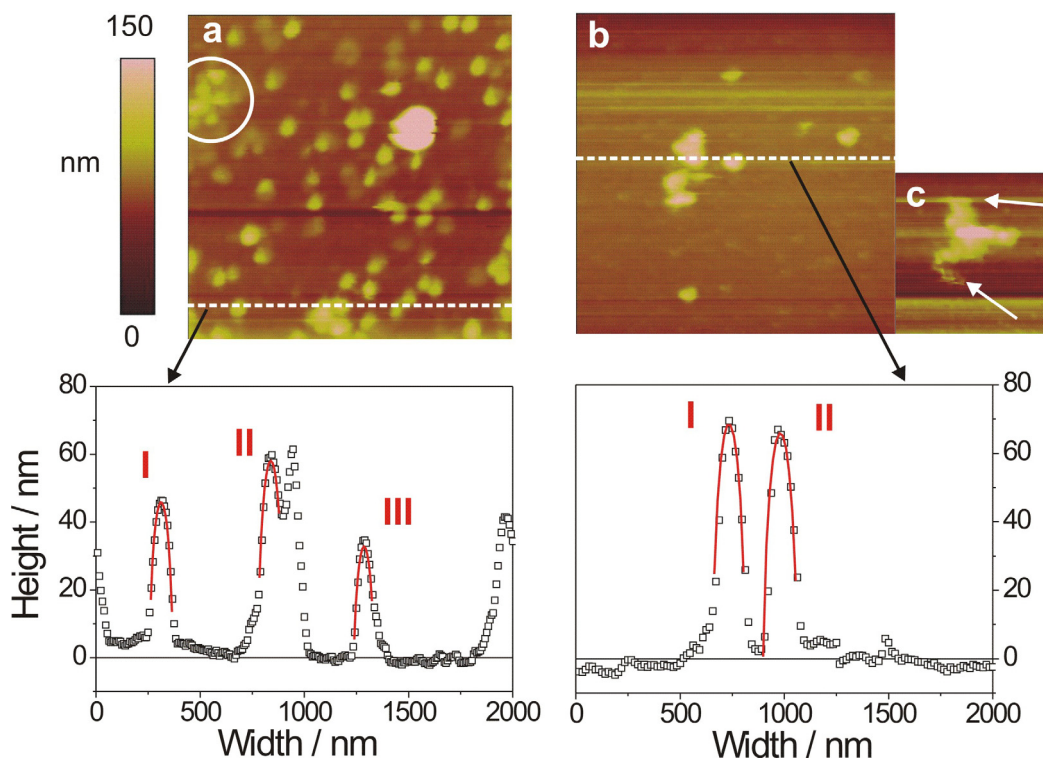


Figure 3.22 AFM contact mode height images, scansize 2 μm x 2 μm and sections. (a) USV with three representative fitted radii: $R_I = 57$ nm, $R_{II} = 59$ nm, $R_{III} = 54$ nm. (b) SSV, with fitted radii of: $R_I = 78$ nm, $R_{II} = 84$ nm. (c) Cluster of SSV's, image scansize is 1 μm x 1 μm, white arrows show deformation due to aggregation and scanning.

For the evaluation of the vesicles with the AFM circles were fitted to image sections. Accordingly, I obtained radii of curvature for the USV $R_{USV} = 55 \pm 15$ nm and for the SSV $R_{SSV} = 81 \pm 15$ nm. Taking into account that the tip radius was 22.5 nm and subtracting twice this value from the SV's radius they were similar to the ones obtained by DLS. In addition it is demonstrated that SVs kept their hemispherical shape when adsorbed on the hard substrate. The adsorption was not too strong and flattened or deformed the SVs, although they were immobilized enough to obtain images.

USVs uniformly covered the surface, whereas no similar coverage was detected for the SSVs. Although both types of SVs were dispensed from solutions with a similar concentration, only a smaller number of SSVs adsorbed to the surface. In theory, the basic synapsin should neutralize the net negative charge of SV phospholipids and therefore weaken the interaction with polylysine, while here

the opposite was observed. USVs showed also a lower tendency to cluster compared to SSVs, although aggregates could be formed. When forming these aggregates USVs kept their hemispherical shape, as can be observed inside the circle of Figure 3.22a. Contrary to the USVs, the SSVs formed larger aggregates, in which it was difficult to discern the single vesicles, since they were more easily deformed and moved by contact with the AFM tip during scanning, especially at the border of the aggregates (arrows in Figure 3.22c).

This suggests that the presence of synapsin I may stabilize the surface as was also observed for phospholipids bilayers on mica [111, 112].

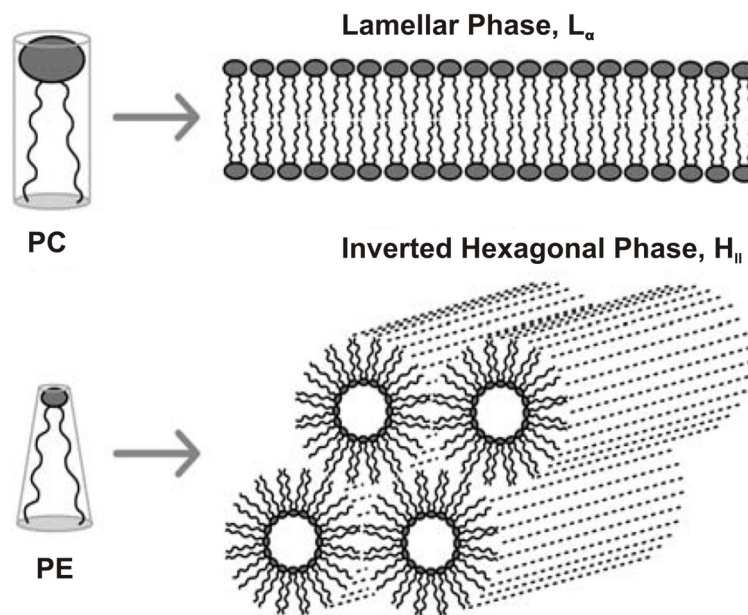


Figure 3.23 Phosphatidylcholine (PC) has the effective shape of a cylinder and favours the linear arrangement in the lamellar phase (Top). Phosphoethanolamine (PE) has the effective shape of an inverted cone and favours the curled arrangement in the inverted hexagonal phase (Bottom). Graph modified after [171].

In fact, synapsin I inhibits the transition of vesicle phospholipids from the lamellar phase (L_{α}) to the inverted hexagonal phase (H_{II}), thus inhibiting membrane fusion, as was shown by Benfenati et al with ^{31}P -nuclear magnetic resonance spectroscopy [108].

The outer leaflet of SV is enriched with phosphatidylethanolamine (PE), a lipid that has a tendency to form concave surfaces at the lipid/water interface due to its shape of an inverted cone. Lipid molecules with such a shape favour the arrangement in the inverted hexagonal phase, H_{II} , in comparison to lipid molecules with a cylindrical shape, such as phosphatidylcholine (PC), which preferentially form lamellar phases (Figure 3.23). Biological membranes are usually close to the transition point from the lamellar phase to the inverted hexagonal phase [172, 173]. This means, that the propensity for membrane fusion is enhanced and that they have to be associated with specific proteins in order to keep the lamellar phase favourable.

The presence of synapsin I at the bilayer surface is thought responsible for reducing the probability of curling for the PE-containing leaflet and thus maintaining the vesicle integrity and uniform size, as well as preventing random fusion events with neighbouring vesicles.

3.3.3 Synaptic vesicles before and after the force-volume scan

As described in the previous chapter the stiffness measurements on SV must be performed without the destruction of the vesicles. Again AFM images were acquired before the FV-scans and afterwards. The control of the intactness of the SV after the FV-scan is crucial, since the indentation should take place only in the limit of small sample deformations, e.g. in the elastic regime, in order to exclude that the sample was deformed plastically or permanently. This ensured that the stiffness measured by the slopes of the force-curves was directly related to the Young's modulus¹ of the SV.

¹ Young's modulus or the tensile elastic modulus is a parameter that reflects the resistance of a material to elongation. The higher the Young's modulus the larger the force needed to deform the material

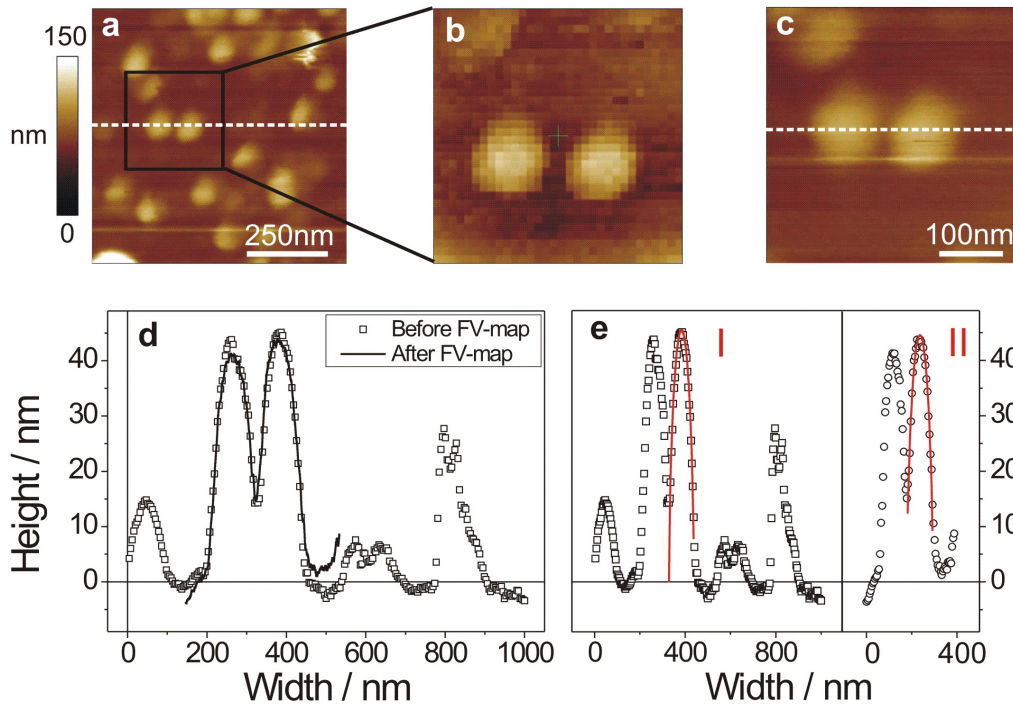


Figure 3.24 Series of AFM images showing: (a) contact mode AFM height image of USV before the FV-scan; (b) height image acquired during the FV-scan, with a resolution of 32×32 data points; (c) contact mode AFM height image after the FV-scan; (d) matching of the two profiles (dashed white lines) from (a) and (c); (e) circular fits (solid red lines) to the two profiles: $R_I = 57$ nm, $R_{II} = 61$ nm.

Figure 3.24a shows a typical image of SVs acquired before the FV-scan. SVs had a height of around 45 nm and were spherical, as I verified by fitting their profiles with circular segments. After zooming in on two adjacent SVs, a FV-map of 32×32 force curves over an area of 400 nm \times 400 nm was acquired, the topography map of which is shown in Figure 3.24b. After the force scan, which required approximately 30 min, I acquired a second image of the two SVs (Figure 3.24c) and compared the two profiles by superposing them in one graph (Figure 3.24d). They matched quite accurately, especially the width, while the height slightly decreased. I also determined the radius of curvature of one SV before and after the FV-scan (Figure 3.24e), and it did not change significantly: $R_I = 57$ nm, $R_{II} = 61$ nm. According to these observations, I could conclude that the measurement was non-destructive to the vesicles, that the tip did not displace them, that they recovered their shape after the indentations and maintained a stable morphology for a prolonged period of time.

3.3.4 Stiffness measurements with the AFM in FV-mode

The AFM in FV-mode allows to obtain information on the mechanical properties of samples by acquiring a two dimensional array of deflection curves over a defined region, a so-called "mapping" of the stiffness in that area of the sample. I calculated the stiffness (of substrate and vesicles) from the acquired deflection curves in the limit of small sample deformations. Along the contact line, i.e., the part of the deflection curve where tip and sample are in contact, the sample deformation D is given by the following [33]

$$D = Z - \delta \quad (1)$$

where Z is the piezo displacement and δ is the cantilever deflection. If D is small, I can write

$$k_c \delta = \frac{k_c k_s}{k_c + k_s} Z = k_{eff} Z \quad (2)$$

where k_c and k_s are the cantilever and sample elastic constants. This simple relation shows that the slope of the approach deflection curve is an indicator of the stiffness of the sample. If the sample is much stiffer than the cantilever, i.e., $k_s \gg k_c$, the deflection curve will probe mainly the stiffness of the cantilever, i.e., $k_{eff} \cong k_c$. If the sample is much more compliant than the cantilever, i.e., $k_s \ll k_c$, the slope of the approach contact line is determined primarily by the stiffness of the sample, i.e., $k_{eff} \cong k_s$. In the following, I calculate the stiffness as the ratio

$$S = k_{eff} / k_c \quad (3)$$

between Z and δ . Therefore, S is dimensionless and $0 < S < 1$.

An example of two typical deflection curves, acquired on the bare mica substrate and at the centre of a native vesicle, is presented in Figure 3.25. The hard mica substrate can not be indented by the tip, the slope of the curve is maximum, and I take it as my reference for stiffness $S = 1$. The soft vesicle, on the other hand, is easily indented by the tip, the slope of the curve is smaller, and thus its stiffness is $S < 1$.

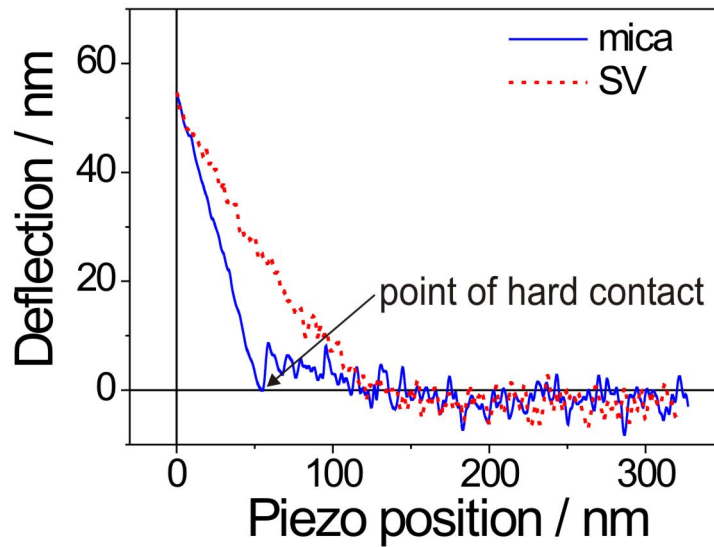


Figure 3.25: Two typical cantilever-deflection vs. piezo-position curves, acquired on the hard mica substrate (dashed line) and at the centre of a SV (solid line). Both curves were triggered to a deflection of ~ 60 nm, corresponding to a maximum load of ~ 0.4 nN, and are part of a 32×32 FV-map.

When the force needed to pierce the polylysine layer is exceeded, the tip jumps into direct "hard contact" with the mica, and from that point on the curve is linear. This allows us to clearly distinguish between the "before-contact" and the "after-contact" parts of the curve. On the other hand, the slope of the curve on the vesicle is smoothly increasing, with no jump marking the point of contact. This makes it hard to distinguish between the "before-contact" and the "after-contact" part.

3.3.5 Stiffness data analysis

Representative results for the FV-maps acquired on both SV types, are displayed in Figure 3.26. The force curves were triggered to ~ 60 nm, which corresponded to a maximum load of ~ 0.4 nN. Three curves, acquired at selected positions, are shown in Fig. 7a: the slope of the curves taken on the SVs is smaller than that of the curve taken on the polylysine-coated mica, which means that also the stiffness, and thus Young's modulus, is smaller. Moreover, the two curves obtained on USVs and SSVs were very similar, suggesting a similar stiffness. This conclusion was confirmed by the evaluation of whole FV-maps instead of single curves.

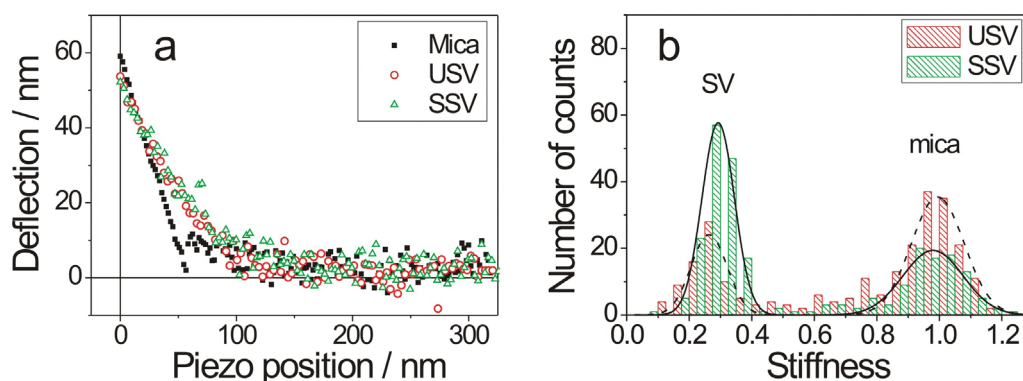


Figure 3.26 (a) Approach force curves acquired at three different places, on mica (black), at the centre of a USV (red), and at the centre of a SSV (green). (b) Histogram of the stiffness values for both SV types and for mica.

The histograms in Figure 3.26a show the stiffness distribution of USVs and SSVs: both histograms have a peak around $S = 1$, which is the stiffness of mica, and peaks at $S = 0.265$ and $S = 0.290$ for USVs and SSVs, respectively.

Although the experiments were repeated several times, the difference in stiffness between the two types of SVs was always smaller than the experimental error intrinsic to our measurements.

I can calculate the Young's modulus for the two types of SVs, according to a shell theory model presented by Delorme et al. [174]:

$$E = \frac{k_{SV} R \sqrt{3(1-\nu^2)}}{4d^2} \quad (4)$$

where k_{SV} is the stiffness of the vesicle, calculated by multiplying its dimensionless stiffness S with the spring constant k_c of the cantilever, R is the radius of curvature of the vesicle, d is the thickness and ν is the Poisson's ratio of the vesicle membrane. Assuming realistic parameter values ($k_{SV} = 0.2$ pN/nm, $R = 25$ nm, $d = 5$ nm, and $\nu = 0.5$), an estimation of the Young's modulus of $E = 75$ kPa is obtained, which is indeed close to values presented in literature [157].

Since there seems to be no difference in stiffness between the two vesicle types I assumed that depleting native SVs from their synapsin coating (i) caused them to expand in size, (ii) reduced the electrostatic repulsion among vesicles and favoured the formation of clusters, but (iii) did not affect their stiffness, at least not in a measure that I could detect by this technique.

Synapsin I is a surface-active molecule that forms monomolecular layers on top of solid-supported phospholipid bilayers, thereby mechanically stabilizing them and decreasing the probability of the AFM tip to penetrate them [175, 176]. This led to the assumption that synapsin I might also reinforce the membrane of SVs, particularly since other proteins are known either to form a stabilizing cage around vesicles, like e.g. clathrin [47], or to crystallize on their surface, like e.g. the bacterial S-layer proteins [161]. On the other hand, I found that both types of vesicles I investigated presented a similar stiffness. This might indicate that synapsin I is neither forming a closed crystalline layer on the vesicles, nor that the molecules interact in a reinforcing manner with each other. In fact, according to estimations from crystal structure [177] a synapsin I molecule covers an area of appr. 18 nm², and it is speculated that up to 30 molecules are present on one vesicle [178]. So only around 20% of the surface of a USV with a diameter of 30 nm is covered by synapsin I, too little to measure its effect, whereas in the case of Pera et al. and Murray et al. [175, 176] synapsin I covered almost entirely the phospholipid bilayer.

3.3.6 Influence of synapsin I on vesicles in solution by DLS and AFM

Next I wanted to verify the influence of synapsin I on the aggregation of native SVs, and determine the kinetics of this process and its selectivity to this specific protein. To this end I performed DLS measurements, under standard conditions and at room temperature, on pure SVs suspensions, on suspensions added with synapsin I (size 80 kDa), and on suspensions added with bovine serum albumin (BSA). I used it as a control protein of comparable size (67 kDa), which should not trigger the aggregation. The solution containing USVs, in a concentration of 40 µg/ml, was placed in the sample holder and let equilibrate for 10 min prior to measurement. After the first measurement, 8 µg of either synapsin I or BSA were added to the suspension by a pipette, in order to prevent severe perturbations in the liquid, which would then disturb the light scattering measurement. Then the solution equilibrated for a time between 2 and 5 min before starting the second measurement. Before the addition of the proteins, the SVs were clearly monodisperse, with a diameter of ~50 nm (Figure 3.27a).

Upon addition of synapsin I, the SVs began to cluster, and eventually formed aggregates bigger than 1 µm after about 20 min. At intermediate times, multiple peaks were visible. After 10 min two peaks at 500 and 1500 nm of similar height were present, whereas at 15 min the former peak became smaller and the latter became larger. The addition of the same amount of BSA did not cause any clustering, as I expected, and the SVs remained monodisperse and of the same size (Figure 3.27b). The aggregation was thus triggered by a specific interaction between synapsin I and SVs.

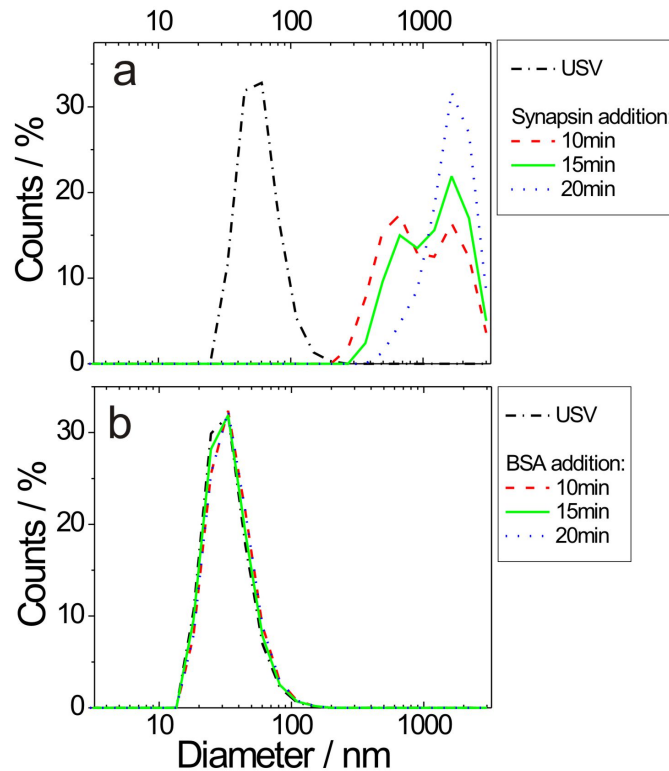


Figure 3.27 DLS data of USVs before and after the addition of either synapsin I or BSA. (a) Synapsin I: SVs are monodisperse with a diameter of 50 nm under basal conditions, and aggregate to clusters larger than 1 μm upon the addition of synapsin I (b) BSA: vesicles remain monodisperse and do not aggregate over time

Immediately after the DLS measurements, I pipetted 50 μl of each of the two vesicle suspensions on polylysine covered mica substrates, let them incubate for 30 min, and then acquired images in contact mode AFM. In the case of SVs added with synapsin I, a closed layer of aggregates of SVs covered large areas of the mica (Figure 3.28a). The cross-section of the aggregates shows a height of about 30 nm and a width of several hundreds of nanometres. On the contrary, the images acquired on SVs added with BSA showed mostly single dispersed vesicles (Figure 3.28b).

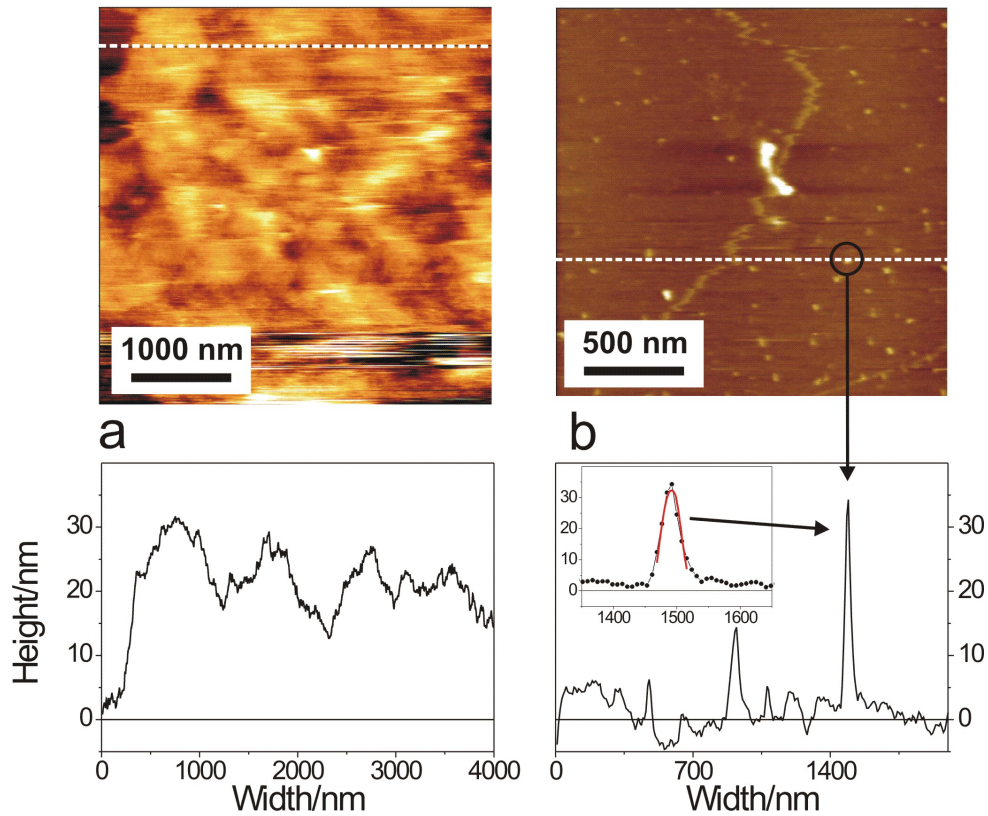


Figure 3.28 AFM topography images of the samples previously analyzed by DLS. (a) Closed SVs layer, or large aggregates, due to the addition of synapsin I to the USV suspension. (b) Control experiment with BSA and single, monodisperse SVs. The radius of curvature of the SV in the inset (red circular arc) is $R = 30.2$ nm.

This image was acquired with a tip with a smaller radius of curvature (around 10 nm), therefore also the radii of the SVs appear smaller than those shown in Figure 3.28. The evaluation of several SVs yielded radii of curvature ranging from 30 to 80 nm. The larger variance of the measured sizes was probably due to the longer time that passed before imaging, and to how this batch of vesicles was treated precedently. Both AFM images provide similar data as obtained with DLS. This combination of methods proves interesting for further interaction studies between SVs and proteins, since it allows to monitor processes taking place in bulk solution, and afterwards the direct imaging of the structures formed.

The results further indicate that synapsin I is responsible for the aggregation of SVs. The fact that USVs which carry synapsin I on their membrane did not show a strong tendency to cluster may be attributable to the electrostatic repulsion among SVs, which is capable of stabilizing them, and to the nearly total absence of synapsin I free in solution by virtue of its very high binding affinity [107, 179, 180]. When the protein is added to the suspension, the additional synapsin molecules, owing to their multiple SV binding sites [179-181] and a high potential to form dimers through the highly conserved central domain C [177, 182] bind to each other and to the SVs, promoting SV clustering. The control experiment with the addition of BSA showed in fact that the clustering process resulted from a specific interaction between synapsin I and SVs.

3.3.7 The use of thawed vesicles

SV can also be stored at -80°C for later use. Since freshly prepared SVs are usable approximately 10 days for studies, when kept on ice in a refrigerator, it was of interest to try experiments with stored SVs. This possibility would allow for more flexibility with the experiments independent from fresh preparations. SVs are diluted 1:1 with Glycerol (87%) and stored in a -80°C freezer until needed. The removal of the glycerol is accomplished either by a centrifugation step at 250 000 g, or by dialysis over night. The stored sample had a volume of 50 μl (25 μl SVs in glycine buffer and 25 μl glycerol). Such a small volume is not easily handled and recovered from a centrifugation tube, so the dialysis in a micro dialysis button² seemed more appropriate. I transferred the sample with a Hamilton syringe and the storage tube was again rinsed with another 20 μl of glycine buffer. The micro dialysis button was sealed with a dialysis membrane with cutoff at 5 kDa. The micro dialysis button was placed in 4 liters of glycine buffer overnight at 4°C . Then I recovered the sample again and determined the protein concentration by Micro BCA³ (Pierce). The protein concentration was usually reduced by 75% with this method. However, there were still enough SV left for AFM and DLS experiments. The frozen, untreated synaptic vesicles (FUSVs) were prepared for the AFM as mentioned before. When imaged in the contact mode they were larger than the USVs and the SSVs, with a height of 90 to 100 nm. The whole imaging process proved to be difficult because the FUSVs attached to the tip more easily. Also fragments of SVs and proteins, which dissociated from the SVs during the whole freezing and thawing procedure, adhered to it remained in the solution.

In Figure 3.29 a stiffness measurement on FUSVs is demonstrated. Also, indicated by the white arrow is an inconsistency of the image recording, where the setpoint had to be adjusted. Often it was not possible to obtain images at all because of instabilities and artifacts, caused by material that interacted with the tip.

² a small plastic container, diameter 1cm, with a small hole in the middle, that is filled with the sample and then covered by a semipermeable membrane with a certain exclusion size, so only small solute molecules can diffuse out into the dialysis medium

³ standard technique for the determination of protein concentrations

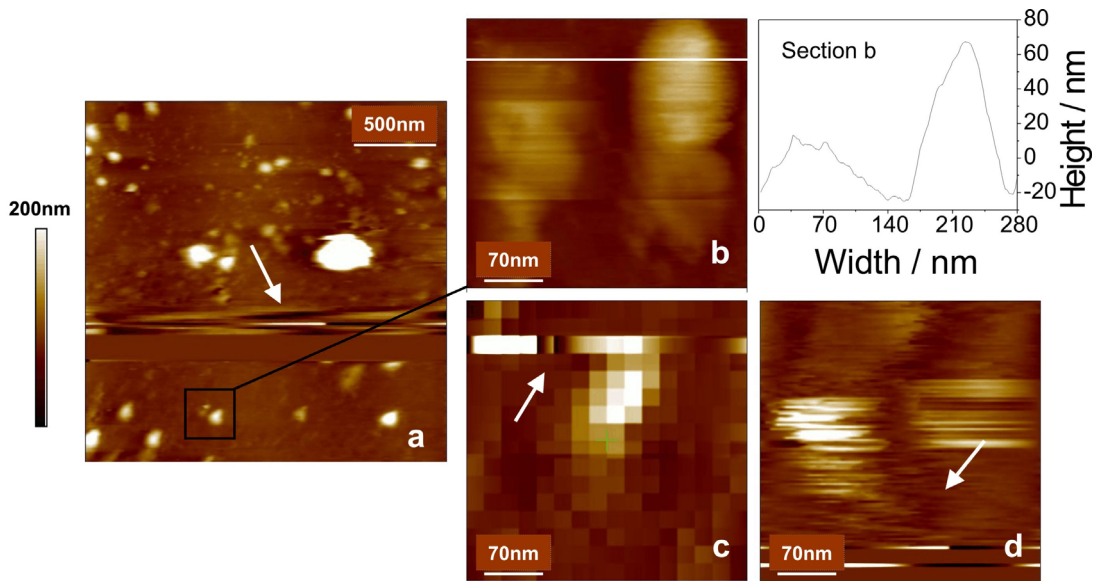


Figure 3.29 Stiffness measurement on frozen and thawed vesicles: (a) contact mode AFM height image of thawed vesicles, size $2\ \mu\text{m} \times 2\ \mu\text{m}$; (b) Zoomed in image of two vesicles, size $280\ \text{nm} \times 280\ \text{nm}$; Sections of the vesicle before (Section b): (c) Image of a force volume plot with 16×16 curves; (d) contact mode AFM height image after the FV-scan, size $280\ \text{nm} \times 280\ \text{nm}$: The sample is more adhesive which leads to drift and inconsistencies (white arrows in a, c, and d) during imaging and damages the vesicles during the FV-scan.

I zoomed in on single vesicles by subsequent steps, the last step is shown in Figure 3.29b. As indicated by the section, the FUSV were larger and they were deformed by the scanning process, as can be seen by the rather oval shape of the vesicle. Figure 3.29c and d show the FV-scan and the state of the vesicle afterwards. The plot contains irregularities due to adhesive events on the tip. The vesicle was deformed and also torn by the procedure. It seemed to be rather sticky, since it was not entirely destroyed, like the SVs measured with a stiffer tip in chapter 3.3.1 and the height was preserved. Considering the instabilities and the state of the sample the use of stored vesicles for AFM experiments cannot be recommended.

DLS

The stored vesicles were also used for DLS studies. The experiment followed the procedure for the other DLS experiments. The size of the FUSV determined by DLS is similar to the size of the USV with a peak at 40 nm (Figure 3.30).

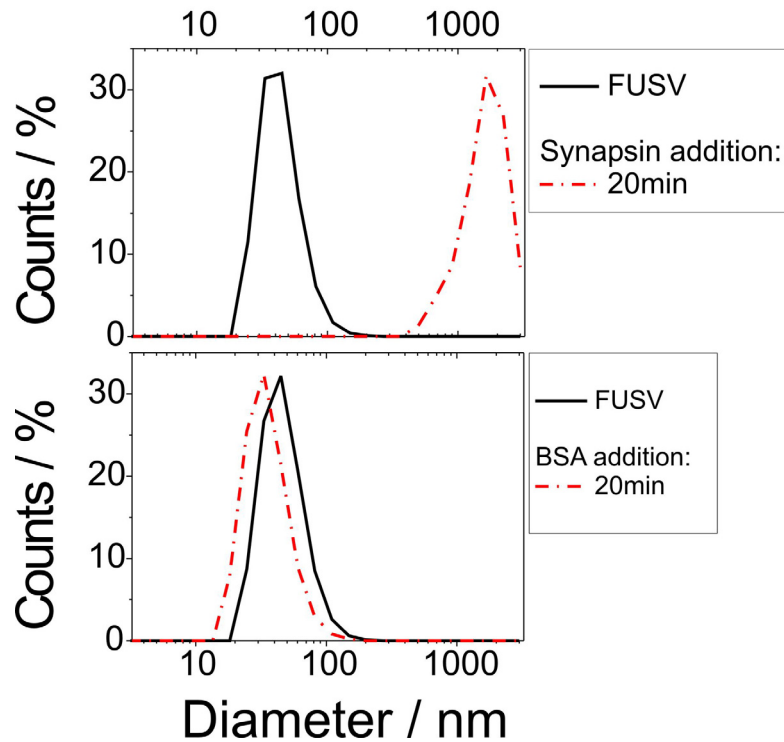


Figure 3.30 DLS data of FUSVs before and after the addition of either synapsin I or BSA. (a) Synapsin I: Like SVs the FUSV aggregate with the addition of synapsin to form larger aggregates (b) BSA: FUSV remain monodisperse after the addition of BSA although their size seems to decrease slightly

With the addition of synapsin, larger aggregates are formed 20 min later, as seen previously with SVs. In the control the size of the FUSVs changed slightly with the addition of BSA.

Both samples were also compared with AFM imaging. Large aggregates were visible for the sample with the synapsin addition. The aggregates were high (300 nm) and bulky, indicating small aggregates that adsorbed in layers to the surface, whereas the SVs joined to aggregates with the height of single vesicles. So FUSVs seemed to fuse also while aggregating or, in addition to the synapsin specific aggregation, they also joined unspecifically once the small aggregates exceeded a certain critical size.

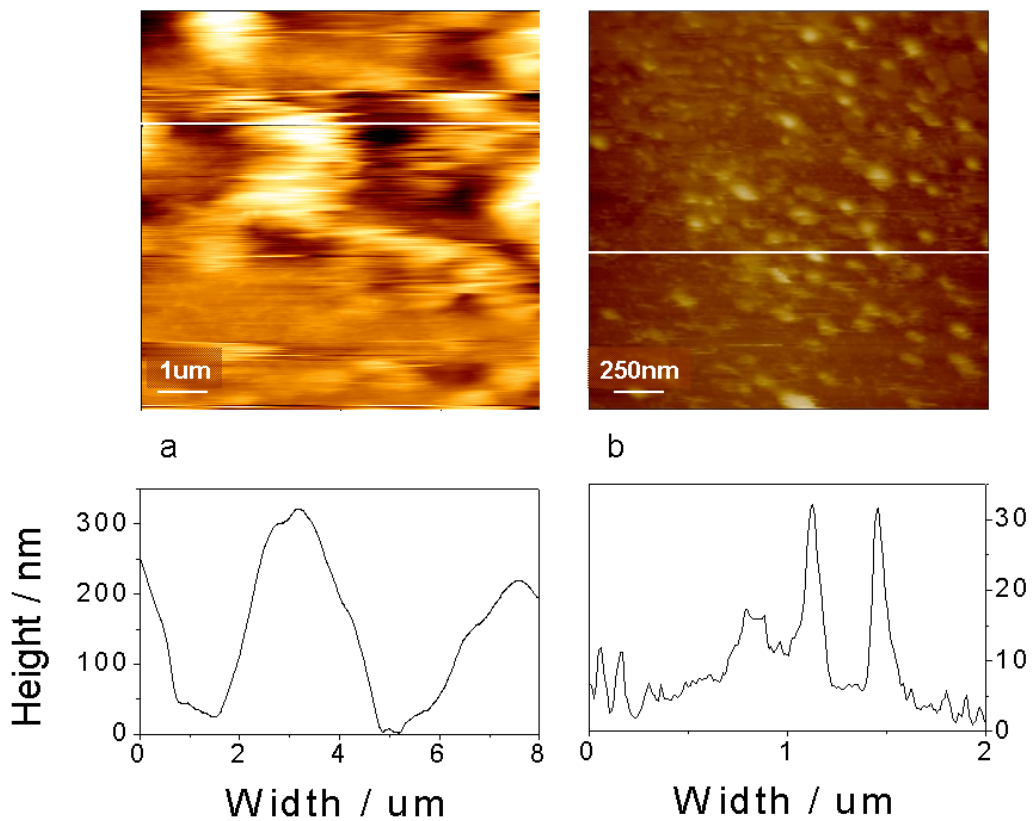


Figure 3.31 AFM topography images of the samples previously analyzed by DLS. (a) Large aggregates, due to the addition of synapsin I. (b) Control experiment with BSA and single, monodisperse FUSV.

The image of the control experiment with BSA shows dispersed vesicles which are rather smaller than the ones imaged before without the addition of BSA. This agrees with the DLS measurement where the FUSVs decreased in size by appr. 10 nm. Also the FUSVs with the BSA are more homogeneously dispersed than the FUSVs without treatment and imaging was easier without the difficulties mentioned before. Thus BSA should have an effect on the FUSVs, which is either not detectable or present, when native SVs are used.

The effect could be connected with the special properties of the BSA. The serum albumins are the most abundant proteins in the blood. They interact not only with several ligands, but also with lipids and are sometimes even carriers for the transport of fatty acids. These proteins are also involved in an immune reaction called opsonization. During opsonization exogenous particles, which entered the bloodstream, are coated with proteins, so-called opsonins, in order to be recognized and removed from the system by specialized immune cells (phagocytes). BSA is also such an opsonin and stabilizes liposomes. Rupture events that occurred at the physiological pH 7.4 decreased for cationic liposomes coated with BSA. The coating did not induce aggregation or rupture [183]. SVs and consequently FUSVs are made of a lipid mixture involving several charged lipids, which would allow for the binding of BSA.

Freshly prepared SVs have an intact protein coating, so the addition of BSA to a solution shows no effect. The binding could be either present to a lower degree or even be hindered by other proteins on the membrane. An effect that is desirable, because native SV should not be marked and removed by the immune system. This might be different for the FUSVs, which lost some stability, according to the AFM measurements. The freezing and thawing process could be responsible for the removal of synapsins, and proteins in general, from the membrane. Also, the addition and removal of glycerol could result in a loss of membrane proteins, since glycerol partitions into the membrane [184] and could change the interaction between some membrane proteins and the lipid bilayer.

So FUSVs can be used as model liposomes for protein interaction studies in DLS, always considering that during the whole process of storing, they changed into a system that differs from freshly prepared SVs. Therefore they can be studied on their own as SVs, affected by the storage conditions, but not for the comparison or as a model for SVs themselves.

4 Conclusions

Although the interaction between membranes is repulsive due to the charged headgroups, it is demonstrated by several groups and a commercially available high-throughput screening system that proteoliposomes are adsorbed to SSM-sensors, and that an analysis of the function of the proteins is possible.

I investigated the nature of this unknown interaction with AFM force-spectroscopy and revealed a possible mechanism for the interaction of the proteoliposomes with the SSM.

To mimic the charged headgroups of a membrane I coated an AFM tip with hydrophilic alkanethiols. I could show that a bilayer adsorbed on the substrate (gold-coated glass) by vesicle fusion displayed the expected repulsive interaction, as did a bilayer formed by a thiol monolayer on the gold and the addition of a complementing DOPC monolayer from a decane solution. Thus, the contribution of the substrate and the decane to a possible attractive interaction could be excluded. For the actual system of the SSM sensor, a thiol monolayer on the gold and the addition of DPhPC from a decane solution, I detected the formation of randomly distributed stacks with up to 5 bilayers on top of each other. This revealed a possible way of interaction between the stacks and the proteoliposomes in the solution. The edges of the bilayer stacks are energetically unfavourable for the membrane and promote the interaction with neighbouring material, in this case they can promote the fusion of the proteoliposomes. This process would lead to the formation of uniform layers, where the spaces between the stacks are filled with bilayers that contain the membrane protein. Such uniform layers are stabilized by the hydrophobic interaction between the lipids. This finding reconciles the repulsive interaction between membranes with the robust and long-lasting deposition of the analyte in a SSM-sensor system.

The behaviour of a natural lipid extract from the archaeobacterium *Methanococcus jannaschii*, which contains among other lipids diether, macrocyclic diether, and tetraether lipids, was investigated with the AFM. As a reference a bilayer was formed by DPPC, a synthetic lipid with a phase transition at 41°C, and the behaviour was monitored by AFM images and AFM force-spectroscopy over a temperature range from 25°C to 50°C. The DPPC bilayer is

Conclusions

in the gel-like phase below 41°C and could not be penetrated by the AFM tip. With higher temperature and near the phase transition to the liquid-crystalline phase, the bilayer became more fluid, and the force needed to penetrate the bilayer decreased.

I achieved a self-assembled, freestanding bilayer from the natural lipid extract and I found that a phase transition is absent in a temperature range from 25°C to 50°C, in contrast to DPPC. Additionally, the interaction between the lipid molecules in the extract was weaker and weakened further with increasing temperature, so that lower forces were necessary to pierce the bilayer. The bilayer from the synthetic lipid displays a higher intermolecular adhesion between the molecules even in the liquid-ordered phase, as shown by higher breakthrough forces. This supports the fact, that natural lipid bilayers are stabilized in the liquid-crystalline phase by a mixture of different lipid molecules. Such mixtures, as was shown for a mixture of diether, macrocyclic diether and tetraether lipids, remain fluid over a broad temperature range. In addition, I showed that a weaker interaction between the molecules is due to their different shape, in comparison to bilayers formed with uniform molecules.

I established a method to image the SVs non-destructively and to probe their mechanical properties in the elastic regime. I also compared the morphology, the mechanical properties, the aggregation state and the aggregation kinetics of two types of SVs: native synaptic vesicles (USVs) associated with endogenous synapsin I, and vesicles that were depleted of their synapsins (SSVs).

I found that USV have a spherical shape, with diameters ranging from 25 to 45 nm, and they are highly monodisperse. SSV have larger diameters, ranging from 40 to 70 nm, and they have a broader size distribution, but are still spherical. Moreover, the stiffness of both types of SVs is similar, at least in the range of our experimental accessibility, and their Young's modulus is around 75 kPa. Although synapsin I has been reported to inhibit the transition of pure phospholipid membranes from the lamellar to the inverted hexagonal phase, the observations suggest that synapsin I does not stabilize mechanically the SV membrane in a way that the membrane proteins of bacteria do by building a crystal layer that protects the cell.

However, bearing a net positive charge with an isoelectric point of over 10, synapsin I seems to convey a stabilizing surface charge to the SVs suspended under physiological pH conditions. This property could prevent non-specific aggregation and random fusion events of SVs *in vivo* and, at the same time, control the clustering process. The removal of synapsin I cancelled this stabilizing effect and, as a result, SSVs had an increased tendency to cluster. Thus, the clear-cut decrease in the number of SVs observed in nerve terminals of synapsin knockout mice may depend on the loss of the stabilizing effect of the synapsin I rather, than on poor mechanical properties of the SV membrane.

Thawed SV that were stored in glycerol are modified by such a procedure, and I showed that they are not suitable as a model system for native SV. The influence of BSA on thawed SV is also demonstrated. I found that BSA seems also to stabilise thawed SV, possibly due to the loss of other outer proteins, not only synapsins, by the freezing procedure, which makes large areas of the lipid membrane available to new binding partners.

5 Bibliography

1. Sengupta, S. and R. Sasisekharan, *Exploiting nanotechnology to target cancer*. British Journal of Cancer, 2007. **96**(9): p. 1315-1319.
2. Goldberg, M., R. Langer, and X.Q. Jia, *Nanostructured materials for applications in drug delivery and tissue engineering*. Journal of Biomaterials Science-Polymer Edition, 2007. **18**(3): p. 241-268.
3. Duncan, R., *Polymer conjugates as anticancer nanomedicines*. Nature Reviews Cancer, 2006. **6**(9): p. 688-701.
4. Duncan, R., *The dawning era of polymer therapeutics*. Nature Reviews Drug Discovery, 2003. **2**(5): p. 347-360.
5. Whitesides, G.M., *The 'right' size in nanobiotechnology*. Nature Biotechnology, 2003. **21**(10): p. 1161-1165.
6. Bohr, M.T., *Nanotechnology goals and challenges for electronic applications*. IEEE Transactions on Nanotechnology, 2002. **1**(1): p. 56-62.
7. Bates, A.K., et al., *Review of technology for 157-nm lithography*. IBM Journal of Research And Development, 2001. **45**(5): p. 605-614.
8. Gourley, P.L., *Brief overview of BioMicroNano technologies*. Biotechnology Progress, 2005. **21**(1): p. 2-10.
9. Cahen, D. and G. Hodes, *Molecules and electronic materials*. Advanced Materials, 2002. **14**(11): p. 789-798.
10. Vettiger, P. and G. Binnig, *The nanodrive project*. Scientific American, 2003. **288**(1): p. 46-53.
11. Vettiger, P., et al., *The "millipede" - Nanotechnology entering data storage*. IEEE Transactions on Nanotechnology, 2002. **1**(1): p. 39-55.
12. Salaita, K., Y.H. Wang, and C.A. Mirkin, *Applications of dip-pen nanolithography*. Nature Nanotechnology, 2007. **2**(3): p. 145-155.
13. Jaschke, M. and H.J. Butt, *Deposition Of Organic Material By The Tip Of A Scanning Force Microscope*. Langmuir, 1995. **11**(4): p. 1061-1064.
14. Hafner, J.H., et al., *Structural and functional imaging with carbon nanotube AFM probes*. Progress In Biophysics & Molecular Biology, 2001. **77**(1): p. 73-110.
15. Scheuring, S., et al., *Single proteins observed by atomic force microscopy*. Single Molecules, 2001. **2**(2): p. 59-67.
16. Drake, B., et al., *Imaging Crystals, Polymers, and Processes in Water with the Atomic Force Microscope*. Science, 1989. **243**(4898): p. 1586-1589.
17. Radmacher, M., et al., *From Molecules to Cells - Imaging Soft Samples with the Atomic Force Microscope*. Science, 1992. **257**(5078): p. 1900-1905.
18. Engel, A., H.E. Gaub, and D.J. Muller, *Atomic force microscopy: A forceful way with single molecules*. Current Biology, 1999. **9**(4): p. R133-R136.
19. Bustamante, C., J.C. Macosko, and G.J.L. Wuite, *Grabbing the cat by the tail: Manipulating molecules one by one*. Nature Reviews Molecular Cell Biology, 2000. **1**(2): p. 130-136.

20. Ros, R., et al., *Single molecule force spectroscopy on ligand-DNA complexes: from molecular binding mechanisms to biosensor applications*. Journal of Biotechnology, 2004. **112**(1-2): p. 5-12.
21. Vogel, V. and M. Sheetz, *Local force and geometry sensing regulate cell functions*. Nature Reviews Molecular Cell Biology, 2006. **7**(4): p. 265-275.
22. Engel, A. and D.J. Muller, *Observing single biomolecules at work with the atomic force microscope*. Nature Structural Biology, 2000. **7**(9): p. 715-718.
23. Seelert, H., et al., *Structural biology - Proton-powered turbine of a plant motor*. Nature, 2000. **405**(6785): p. 418-419.
24. Whitesides, G.M., et al., *Soft lithography in biology and biochemistry*. Annual Review of Biomedical Engineering, 2001. **3**: p. 335-373.
25. Weibel, D.B., W.R. DiLuzio, and G.M. Whitesides, *Microfabrication meets microbiology*. Nature Reviews Microbiology, 2007. **5**(3): p. 209-218.
26. Mrksich, M. and G.M. Whitesides, *Patterning Self-Assembled Monolayers Using Microcontact Printing - A New Technology For Biosensors*. Trends in Biotechnology, 1995. **13**(6): p. 228-235.
27. Ulman, A., *Formation and structure of self-assembled monolayers*. Chemical Reviews, 1996. **96**(4): p. 1533-1554.
28. Love, J.C., et al., *Self-assembled monolayers of thiolates on metals as a form of nanotechnology*. Chemical Reviews, 2005. **105**(4): p. 1103-1169.
29. Binnig, G., C.F. Quate, and C. Gerber, *Atomic force microscope*. Physical Review Letters, 1986. **56**(9): p. 930-933.
30. Hansma, H.G., et al., *Properties of biomolecules measured from atomic force microscope images: A review*. Journal of Structural Biology, 1997. **119**(2): p. 99-108.
31. Horber, J.K.H. and M.J. Miles, *Scanning probe evolution in biology*. Science, 2003. **302**(5647): p. 1002-1005.
32. Butt, H.J., et al., *Imaging Cells with the Atomic Force Microscope*. Journal of Structural Biology, 1990. **105**(1-3): p. 54-61.
33. Butt, H.J., B. Cappella, and M. Kappl, *Force measurements with the atomic force microscope: Technique, interpretation and applications*. Surface Science Reports, 2005. **59**(1-6): p. 1-152.
34. Ralston, J., et al., *Atomic force microscopy and direct surface force measurements - (IUPAC technical report)*. Pure and Applied Chemistry, 2005. **77**(12): p. 2149-2170.
35. Butt HJ, A.A., *Atomic force microscopy on lipid bilayers*. Advances in Planar Lipid Bilayers and Liposomes, 2006. **3**(7): p. 220-243.
36. Dufrene, Y.F., *Atomic force microscopy of membrane proteins separating two aqueous compartments*. Nature Methods, 2006. **3**(12): p. 973-975.
37. Dufrene, Y.F., *Using nanotechniques to explore microbial surfaces*. Nature Reviews Microbiology, 2004. **2**(6): p. 451-460.
38. Pintschovius, J. and K. Fendler, *Charge translocation by the Na⁺/K⁺-ATPase investigated on solid supported membranes: Rapid solution exchange with a new technique*. Biophysical Journal, 1999. **76**(2): p. 814-826.

39. Hanford, M. and T.L. Peeples, *Archaeal tetraether lipids - Unique structures and applications*. Applied Biochemistry and Biotechnology, 2002. **97**(1): p. 45-62.
40. Derosa, M., et al., *Lipids Of The Archaea - A New Tool For Bioelectronics*. Biosensors & Bioelectronics, 1994. **9**(9-10): p. 669-675.
41. Patel, G.B., et al., *In vitro assessment of archaeosome stability for developing oral delivery systems*. International Journal of Pharmaceutics, 2000. **194**(1): p. 39-49.
42. Krishnan, L., et al., *Archaeosome vaccine adjuvants induce strong humoral, cell-mediated, and memory responses: Comparison to conventional liposomes and alum*. Infection and Immunity, 2000. **68**(1): p. 54-63.
43. Garcia-Manyes, S., G. Oncins, and F. Sanz, *Effect of temperature on the nanomechanics of lipid bilayers studied by force spectroscopy*. Biophysical Journal, 2005. **89**(6): p. 4261-4274.
44. Ricci, D., M. Tedesco, and M. Grattarola, *Mechanical and morphological properties of living 3T6 cells probed via scanning force microscopy*. Microscopy Research and Technique, 1997. **36**: p. 165-171.
45. Fery, A., F. Dubreuil, and H. Mohwald, *Mechanics of artificial microcapsules*. New Journal of Physics, 2004. **6**.
46. Bonaccorso, E., B. Cappella, and K. Graf, *Local mechanical properties of plasma treated polystyrene surfaces*. Journal of Physical Chemistry B, 2006. **110**(36): p. 17918-17924.
47. Jin, A.J., et al., *Measuring the elasticity of clathrin-coated vesicles via atomic force microscopy*. Biophysical Journal, 2006. **90**(9): p. 3333-3344.
48. Nitzsche, R., *Partikelgrößenmessung im Submikronbereich*. Chemie in Labor und Biotechnik, 1997. **48**(10): p. 422-427.
49. Israelachvili, J.N., *Intermolecular and Surface Forces*. 1991.
50. Butt, H.J., K. Graf, and M. Kappl, *Physics and Chemistry of Interfaces*. 2003.
51. Derjaguin, B. and L. Landau, *Theory Of Stability Of Highly Charged Liophobic Sols And Adhesion Of Highly Charged Particles In Solutions Of Electrolytes*. Zhurnal Eksperimentalnoi I Teoreticheskoi Fiziki, 1945. **15**(11): p. 663-682.
52. Verwey, E.J.W. and J.T.G. Overbeek, *Theory of the stability of lyophobic colloids*. 1948.
53. Keesom, W., *Van der Waals's cohesion strength - Correction*. Physikalische Zeitschrift, 1921. **22**: p. 643-644.
54. Keesom, W., *On Waal's cohesion forces*. Physikalische Zeitschrift, 1921. **22**: p. 129-141.
55. Debye, P., *The van der Waals cohesion forces*. Physikalische Zeitschrift, 1920. **21**: p. 178-187.
56. Debye, P., *Molecular forces and their electric explanation*. Physikalische Zeitschrift, 1921. **22**: p. 302-308.
57. London, F., *Some characteristics and uses of molecular force*. Zeitschrift für Physikalische Chemie-Abteilung B-Chemie der Elementarprozesse, Aufbau der Materie, 1930. **11**(2/3): p. 222-251.
58. Gouy, G., *Sur la constitution de la charge électrique a la surface d'un electrolyte*. J. Phys. Radium (Paris), 1910. **9**: p. 457-468.

59. Chapman, D.L., *A contribution to the theory of electrocapillarity*. Philosophical Magazine, 1913. **25**: p. 475-481.
60. Debye, P. and E. Huckel, *The theory of electrolytes I. The lowering of the freezing point and related occurrences*. Physikalische Zeitschrift, 1923. **24**: p. 185-206.
61. Barouch, E. and E. Matijevic, *Double-Layer Interactions Of Unequal Spheres. 1. The Effect Of Electrostatic Attraction With Particles Of Like Sign Of Potential*. Journal of The Chemical Society-Faraday Transactions I, 1985. **81**: p. 1797-1817.
62. Israelachvili, J. and H. Wennerstrom, *Role of hydration and water structure in biological and colloidal interactions*. Nature, 1996. **379**(6562): p. 219-225.
63. Israelachvili, J. and H. Wennerstrom, *Entropic forces between amphiphilic surfaces in liquids*. Journal of Physical Chemistry, 1992. **96**(2): p. 520-531.
64. Christenson, H.K., *Modern Approaches to Wettability*. 1992: p. 29.
65. Claesson, P.M., et al., *Interactions Between Water-Stable Hydrophobic Langmuir-Blodgett Monolayers On Mica*. Journal of Colloid and Interface Science, 1986. **114**(1): p. 234-242.
66. Steitz, R., et al., *Nanobubbles and their precursor layer at the interface of water against a hydrophobic substrate*. Langmuir, 2003. **19**(6): p. 2409-2418.
67. Yoon, R.H., D.H. Flinn, and Y.I. Rabinovich, *Hydrophobic interactions between dissimilar surfaces*. Journal of Colloid and Interface Science, 1997. **185**(2): p. 363-370.
68. Singer, S.J. and G.L. Nicolson, *Fluid Mosaic Model Of Structure Of Cell-Membranes*. Science, 1972. **175**(4023): p. 720-&.
69. Simons, K. and E. Ikonen, *Functional rafts in cell membranes*. Nature, 1997. **387**(6633): p. 569-572.
70. Maxfield, F.R. and I. Tabas, *Role of cholesterol and lipid organization in disease*. Nature, 2005. **438**(7068): p. 612-621.
71. Saxton, M.J. and K. Jacobson, *Single-particle tracking: Applications to membrane dynamics*. Annual Review of Biophysics and Biomolecular Structure, 1997. **26**: p. 373-399.
72. Saxton, M.J., *Single-particle tracking: The distribution of diffusion coefficients*. Biophysical Journal, 1997. **72**(4): p. 1744-1753.
73. Engelman, D.M., *Membranes are more mosaic than fluid*. Nature, 2005. **438**(7068): p. 578-580.
74. Jensen, M.O., O.G. Mouritsen, and G.H. Peters, *The hydrophobic effect: Molecular dynamics simulations of water confined between extended hydrophobic and hydrophilic surfaces*. Journal of Chemical Physics, 2004. **120**(20): p. 9729-9744.
75. Nagle, J.F., *Lipid Bilayer Phase-Transition - Density-Measurements And Theory*. Proceedings of the National Academy of Sciences of the United States of America, 1973. **70**(12): p. 3443-3444.
76. Mabrey, S. and J.M. Sturtevant, *Investigation Of Phase-Transitions Of Lipids And Lipid Mixtures By High Sensitivity Differential Scanning Calorimetry*. Proceedings of the National Academy of Sciences of the United States of America, 1976. **73**(11): p. 3862-3866.

77. Koynova, R. and M. Caffrey, *Phases and phase transitions of the phosphatidylcholines*. Biochimica et Biophysica Acta-Reviews on Biomembranes, 1998. **1376**(1): p. 91-145.
78. Woese, C.R., O. Kandler, and M.L. Wheelis, *Towards A Natural System Of Organisms - Proposal For The Domains Archaea, Bacteria, And Eucarya*. Proceedings of the National Academy of Sciences of the United States of America, 1990. **87**(12): p. 4576-4579.
79. Jones, W.J., et al., *Methanococcus-Jannaschii Sp-Nov, An Extremely Thermophilic Methanogen From A Submarine Hydrothermal Vent*. Archives of Microbiology, 1983. **136**(4): p. 254-261.
80. Bult, C.J., et al., *Complete genome sequence of the methanogenic archaeon, Methanococcus jannaschii*. Science, 1996. **273**(5278): p. 1058-1073.
81. Comita, P.B., et al., *Structural Elucidation Of A Unique Macrocyclic Membrane Lipid From A New, Extremely Thermophilic, Deep-Sea Hydrothermal Vent Archaeobacterium, Methanococcus-Jannaschii*. Journal of Biological Chemistry, 1984. **259**(24): p. 5234-5241.
82. Sprott, G.D., M. Meloche, and J.C. Richards, *Proportions Of Diether, Macrocyclic Diether, And Tetraether Lipids In Methanococcus-Jannaschii Grown At Different Temperatures*. Journal of Bacteriology, 1991. **173**(12): p. 3907-3910.
83. Melchior, D.L., *Lipid Phase-Transitions And Regulation Of Membrane Fluidity In Prokaryotes*. Current Topics in Membranes and Transport, 1982. **17**: p. 263-316.
84. Sackmann, E., *Supported membranes: Scientific and practical applications*. Science, 1996. **271**(5245): p. 43-48.
85. Janshoff, A. and C. Steinem, *Transport across artificial membranes - an analytical perspective*. Analytical and Bioanalytical Chemistry, 2006. **385**(3): p. 433-451.
86. Castellana, E.T. and P.S. Cremer, *Solid supported lipid bilayers: From biophysical studies to sensor design*. Surface Science Reports, 2006. **61**(10): p. 429-444.
87. Tamm, L.K. and H.M. McConnell, *Supported Phospholipid-Bilayers*. Biophysical Journal, 1985. **47**(1): p. 105-113.
88. Jass, J., T. Tjarnhage, and G. Puu, *From liposomes to supported, planar bilayer structures on hydrophilic and hydrophobic surfaces: An atomic force microscopy study*. Biophysical Journal, 2000. **79**(6): p. 3153-3163.
89. Dufrene, Y.F. and G.U. Lee, *Advances in the characterization of supported lipid films with the atomic force microscope*. Biochimica et Biophysica Acta-Biomembranes, 2000. **1509**(1-2): p. 14-41.
90. Muller, D.J., *Out and in: Simplifying membrane protein studies by AFM*. Biophysical Journal, 2006. **91**(9): p. 3133-3134.
91. Sinner, E.K. and W. Knoll, *Functional tethered membranes*. Current Opinion In Chemical Biology, 2001. **5**(6): p. 705-711.
92. Hediger, M.A., et al., *The ABCs of solute carriers: physiological, pathological and therapeutic implications of human membrane transport proteins - Introduction*. Pflugers Archiv-European Journal of Physiology, 2004. **447**(5): p. 465-468.
93. Drews, J., *Drug discovery: A historical perspective*. Science, 2000. **287**(5460): p. 1960-1964.

94. Gropp, T., et al., *Kinetics of electrogenic transport by the ADP/ATP carrier*. Biophysical Journal, 1999. **77**(2): p. 714-726.
95. Fendler, K., et al., *Transport Protein on Solid-Supported Membranes: From Basic Research to Drug Discovery*. Ultrathin Electrochemical Chemo- and Biosensors, 2004. **2**: p. 331-349.
96. Buoninsegni, F.T., et al., *Time-resolved charge translocation by sarcoplasmic reticulum Ca-ATPase measured on a solid supported membrane*. Biophysical Journal, 2004. **86**(6): p. 3671-3686.
97. Decamilli, P., et al., *The Synapsins*. Annual Review of Cell Biology, 1990. **6**: p. 433-460.
98. Pieribone, V.A., et al., *Distinct Pools Of Synaptic Vesicles In Neurotransmitter Release*. Nature, 1995. **375**(6531): p. 493-497.
99. Heuser, J.E. and T.S. Reese, *Evidence For Recycling Of Synaptic Vesicle Membrane During Transmitter Release At Frog Neuromuscular Junction*. Journal of Cell Biology, 1973. **57**(2): p. 315-344.
100. Ceccarelli, B., W.P. Hurlbut, and A. Mauro, *Turnover Of Transmitter And Synaptic Vesicles At Frog Neuromuscular Junction*. Journal of Cell Biology, 1973. **57**(2): p. 499-524.
101. Rossi, M.L., et al., *Quantal Nature Of Synaptic Transmission At The Cytoneural Junction In The Frog Labyrinth*. Journal of Physiology-London, 1994. **478**(1): p. 17-35.
102. Sudhof, T.C., *The synaptic vesicle cycle*. Annual Review of Neuroscience, 2004. **27**: p. 509-547.
103. Sudhof, T.C., et al., *Synapsins - Mosaics of Shared and Individual Domains in a Family of Synaptic Vesicle Phosphoproteins*. Science, 1989. **245**(4925): p. 1474-1480.
104. Navone, F., P. Greengard, and P. Decamilli, *Synapsin-I in Nerve-Terminals - Selective Association with Small Synaptic Vesicles*. Science, 1984. **226**(4679): p. 1209-1211.
105. Valtorta, F., et al., *Localization Of Synapsin-I At The Frog Neuromuscular-Junction*. Neuroscience, 1988. **24**(2): p. 593-603.
106. Huttner, W.B., et al., *Synapsin-I (Protein-I), a Nerve Terminal-Specific Phosphoprotein.3. Its Association with Synaptic Vesicles Studied in a Highly Purified Synaptic Vesicle Preparation*. Journal of Cell Biology, 1983. **96**(5): p. 1374-1388.
107. Schiebler, W., et al., *Characterization of Synapsin-I Binding to Small Synaptic Vesicles*. Journal of Biological Chemistry, 1986. **261**(18): p. 8383-8390.
108. Benfenati, F., et al., *Interactions Of Synapsin-I With Phospholipids - Possible Role In Synaptic Vesicle Clustering And In The Maintenance Of Bilayer Structures*. Journal of Cell Biology, 1993. **123**(6): p. 1845-1855.
109. Baldelli, P., et al., *Synapsins and neuroexocytosis: Recent views from functional studies on synapsin null mutant mice*. Archives Italiennes de Biologie, 2005. **143**(2): p. 113-126.
110. Ho, M., et al., *Synapsin I is a highly surface-active molecule*. Journal of Biological Chemistry, 1991. **266**(9): p. 5600-5607.

111. Pera, I., et al., *Using the atomic force microscope to study the interaction between two solid supported lipid bilayers and the influence of synapsin I*. Biophysical Journal, 2004. **87**(4): p. 2446-2455.
112. Murray, J., et al., *Imaging the selective binding of synapsin to anionic membrane domains*. Chembiochem, 2004. **5**(11): p. 1489-1494.
113. Bamberg, E., et al., *Photocurrents Generated By Bacteriorhodopsin On Planar Bilayer Membranes*. Biophysics of Structure and Mechanism, 1979. **5**(4): p. 277-292.
114. Bligh, E. and W. Dyer, *A rapid method of total lipid extraction and purification*. Canadian Journal of Biochemistry and Physiology, 1959. **37**(8): p. 911-917.
115. Lewis, T., P.D. Nichols, and T.A. McMeekin, *Evaluation of extraction methods for recovery of fatty acids from lipid-producing microheterotrophs*. Journal of Microbiological Methods, 2000. **43**(2): p. 107-116.
116. DeRosa, M., *Archaeal lipids: Structural features and supramolecular organization*. Thin Solid Films, 1996. **285**: p. 13-17.
117. Pick, U., *Liposomes With A Large Trapping Capacity Prepared By Freezing And Thawing Of Sonicated Phospholipid Mixtures*. Archives of Biochemistry and Biophysics, 1981. **212**(1): p. 186-194.
118. Bahler, M. and P. Greengard, *Synapsin-I Bundles F-Actin In A Phosphorylation-Dependent Manner*. Nature, 1987. **326**(6114): p. 704-707.
119. Binnig, G., et al., *Tunneling through a controllable vacuum gap*. Applied Physics Letters, 1982. **40**(2): p. 178-180.
120. Binnig, G. and D. Smith, *Single-tube 3-dimensional scanner for scanning tunneling microscopy*. Review of Scientific Instruments, 1986. **57**(8): p. 1688-1689.
121. Meyer, E., *Atomic Force Microscopy*. Progress in Surface Science, 1992. **41**(1): p. 3-49.
122. Binnig, G., *Force Microscopy*. Ultramicroscopy, 1992. **42**: p. 7-15.
123. Gaboriaud, F. and Y.F. Dufrene, *Atomic force microscopy of microbial cells: Application to nanomechanical properties, surface forces and molecular recognition forces*. Colloids and Surfaces B-Biointerfaces, 2007. **54**(1): p. 10-19.
124. Cleveland, J., et al., *A non-destructive method for determining the spring constant of cantilevers for scanning force microscopy*. Review of Scientific Instruments, 1993. **64**(2): p. 403-405.
125. Sader, J., J. Chon, and P. Mulvaney, *Calibration of rectangular atomic force microscope cantilevers*. Review of Scientific Instruments, 1999. **70**(10): p. 3967-3969.
126. Gibson, C., G. Watson, and S. Myhra, *Determination of the spring constants of probes for force microscopy/spectroscopy*. Nanotechnology, 1996. **7**(3): p. 259-262.
127. Hutter, J.L. and J. Bechhoefer, *Calibration of atomic force microscope tips*. Review of Scientific Instruments, 1993. **64**(7): p. 1868-1873.
128. Butt, H.-J. and M. Jaschke, *Calculation of thermal noise in atomic force microscopy*. Nanotechnology, 1995. **6**: p. 1-7.

129. Hutter, J., *Comment on tilt of atomic force microscope cantilevers: effect on spring constant and adhesion measurements*. LANGMUIR, 2005. **21**(6): p. 2630-2632.
130. Rawle, A., *Efficient control of industrial processes - Analysis of particle-size distribution*. Chemie Ingenieur Technik, 1999. **71**(9): p. 52-53.
131. Raunser, S., et al., *Structure and function of prokaryotic glutamate transporters from Escherichia coli and Pyrococcus horikoshii*. Biochemistry, 2006. **45**(42): p. 12796-12805.
132. Zuber, D., et al., *Kinetics of charge translocation in the passive downhill uptake mode of the Na⁺/H⁺ antiporter NhaA of Escherichia coli*. Biochimica et Biophysica Acta-Bioenergetics, 2005. **1709**(3): p. 240-250.
133. Zhou, A., et al., *Charge translocation during cosubstrate binding in the Na⁺/proline transporter of E-coli*. Journal of Molecular Biology, 2004. **343**(4): p. 931-942.
134. Adamson, A.W. and A.P. Gast, *Physical Chemistry of Surfaces*. 1997.
135. Brian, A.A. and H.M. McConnell, *Allogeneic Stimulation Of Cyto-Toxic T-Cells By Supported Planar Membranes*. Proceedings of the National Academy of Sciences of the United States of America-Biological Sciences, 1984. **81**(19): p. 6159-6163.
136. McConnell, H.M., et al., *Supported Planar Membranes In Studies Of Cell-Cell Recognition In The Immune-System*. Biochimica et Biophysica Acta, 1986. **864**(1): p. 95-106.
137. Mueller, H., H.J. Butt, and E. Bamberg, *Force measurements on myelin basic protein adsorbed to mica and lipid bilayer surfaces done with the atomic force microscope*. Biophysical Journal, 1999. **76**(2): p. 1072-1079.
138. Mueller, H., H.J. Butt, and E. Bamberg, *Adsorption of membrane-associated proteins to lipid bilayers studied with an atomic force microscope: Myelin basic protein and cytochrome c*. Journal of Physical Chemistry B, 2000. **104**(18): p. 4552-4559.
139. Dufrene, Y.F., et al., *Characterization of the physical properties of model biomembranes at the nanometer scale with the atomic force microscope*. Faraday Discussions, 1998: p. 79-94.
140. Ducker, W.A. and D.R. Clarke, *Controlled Modification Of Silicon-Nitride Interactions In Water Via Zwitterionic Surfactant Adsorption*. Colloids and Surfaces A-Physicochemical and Engineering Aspects, 1994. **93**: p. 275-292.
141. Dubois, L.H. and R.G. Nuzzo, *Synthesis, Structure, And Properties Of Model Organic-Surfaces*. Annual Review of Physical Chemistry, 1992. **43**: p. 437-463.
142. Yoon, R., D. Flinn, and Y. Rabinovich, *Hydrophobic interactions between dissimilar surfaces*. Journal of Colloid and Interface Science, 1997. **185**(2): p. 363-370.
143. Nagle, J.F. and S. Tristram-Nagle, *Structure of lipid bilayers*. Biochimica et Biophysica Acta-Reviews on Biomembranes, 2000. **1469**(3): p. 159-195.
144. McIntosh, T.J., A.D. Magid, and S.A. Simon, *Steric Repulsion Between Phosphatidylcholine Bilayers*. Biochemistry, 1987. **26**(23): p. 7325-7332.
145. Jiang, F.Y., Y. Bouret, and J.T. Kindt, *Molecular dynamics simulations of the lipid bilayer edge*. Biophysical Journal, 2004. **87**(1): p. 182-192.

146. Richter, R.P. and A.R. Brisson, *Following the formation of supported lipid bilayers on mica: A study combining AFM, QCM-D, and ellipsometry*. Biophysical Journal, 2005. **88**(5): p. 3422-3433.
147. Xie, A.F., et al., *Materials science of the gel to fluid phase transition in a supported phospholipid bilayer*. Physical Review Letters, 2002. **89**(24).
148. Leonenko, Z.V., et al., *Investigation of temperature-induced phase transitions in DOPC and DPPC phospholipid bilayers using temperature-controlled scanning force microscopy*. Biophysical Journal, 2004. **86**(6): p. 3783-3793.
149. Yang, J. and J. Appleyard, *The main phase transition of mica-supported phosphatidylcholine membranes*. Journal of Physical Chemistry B, 2000. **104**(34): p. 8097-8100.
150. Fan, Q., et al., *Stability Against Temperature And External Agents Of Vesicles Composed Of Archaeal Bolaform Lipids And Egg Pc*. Biochimica et Biophysica Acta-Biomembranes, 1995. **1240**(1): p. 83-88.
151. Richter, R.P. and A. Brisson, *Characterization of lipid bilayers and protein assemblies supported on rough surfaces by atomic force microscopy*. Langmuir, 2003. **19**(5): p. 1632-1640.
152. Lemmich, J., et al., *Solutes in small amounts provide for lipid-bilayer softness: Cholesterol, short-chain lipids, and bola lipids*. EUROPEAN BIOPHYSICS JOURNAL WITH BIOPHYSICS LETTERS, 1996. **25**(1): p. 61-65.
153. Rohmer, M., P. Bouvier, and G. Ourisson, *Molecular Evolution Of Biomembranes - Structural Equivalents And Phylogenetic Precursors Of Sterols*. Proceedings of the National Academy of Sciences of the United States of America, 1979. **76**(2): p. 847-851.
154. Kaneshiro, S. and D. Clark, *Pressure effects on the composition and thermal Behavior of lipids from the deep-sea thermophile Methanococcus Jannaschii*. Journal of Bacteriology, 1995. **177**(13): p. 3668-3672.
155. Parpura, V., et al., *Dynamic Imaging of Purified Individual Synaptic Vesicles*. Neuroimage, 1995. **2**(1): p. 3-7.
156. Garcia, R.A., et al., *Substructure and responses of cholinergic synaptic vesicles in the atomic force microscope*. Journal of Neuroscience Research, 1998. **52**(3): p. 350-355.
157. Laney, D.E., et al., *Changes in the elastic properties of cholinergic synaptic vesicles as measured by atomic force microscopy*. Biophysical Journal, 1997. **72**(2): p. 806-813.
158. Liopo, A., et al., *The response of the neuronal membrane to acetaldehyde treatment*. Cellular & Molecular Biology Letters, 2001. **6**(2A): p. 265-269.
159. Sritharan, K.C., et al., *Binding contribution between synaptic vesicle membrane and plasma membrane proteins in neurons: An AFM study*. Cell Biology International, 1998. **22**(9-10): p. 649-655.
160. Yersin, A., et al., *Interactions between synaptic vesicle fusion proteins explored by atomic force microscopy*. Proceedings of the National Academy of Sciences of the United States of America, 2003. **100**(15): p. 8736-8741.
161. Martin-Molina, A., et al., *Structure, surface interactions, and compressibility of bacterial S-layers through scanning force microscopy and the surface force apparatus*. Biophysical Journal, 2006. **90**(5): p. 1821-1829.

162. McLaughl.J, K.R. Case, and H.B. Bosmann, *Electrokinetic Properties Of Isolated Cerebral-Cortex Synaptic Vesicles*. Biochemical Journal, 1973. **136**(4): p. 919-926.
163. Ohsawa, K., H. Ohshima, and S. Ohki, *Surface-Potential And Surface-Charge Density Of The Cerebral-Cortex Synaptic Vesicle And Stability Of Vesicle Suspension*. Biochimica et Biophysica Acta, 1981. **648**(2): p. 206-214.
164. Hunter, R.J., *Foundations of Colloid Science*. 2002. **Vol 1 + 2**.
165. Ninham, B.W. and V. Yaminsky, *Ion binding and ion specificity: The Hofmeister effect and Onsager and Lifshitz theories*. Langmuir, 1997. **13**(7): p. 2097-2108.
166. Blackford, B.L., M.H. Jericho, and P.J. Mulhern, *A Review Of Scanning Tunneling Microscope And Atomic Force Microscope Imaging Of Large Biological Structures - Problems And Prospects*. Scanning Microscopy, 1991. **5**(4): p. 907-918.
167. Mazia, D., G. Schatten, and W. Sale, *Adhesion Of Cells To Surfaces Coated With Polylysine - Applications To Electron-Microscopy*. Journal of Cell Biology, 1975. **66**(1): p. 198-200.
168. Schmitt, J., et al., *Preparation and optical properties of colloidal gold monolayers*. Langmuir, 1999. **15**(9): p. 3256-3266.
169. Chi, P., P. Greengard, and T.A. Ryan, *Synapsin dispersion and reclustering during synaptic activity*. Nature Neuroscience, 2001. **4**(12): p. 1187-1193.
170. Morrison, F.A., *Understanding Rheology*. 2001: p. 545.
171. Hamai, C., et al., *Effect of average phospholipid curvature on supported bilayer formation on glass by vesicle fusion*. Biophysical Journal, 2006. **90**(4): p. 1241-1248.
172. Gruner, S.M., et al., *Lipid Polymorphism - The Molecular-Basis Of Nonbilayer Phases*. Annual Review of Biophysics and Biophysical Chemistry, 1985. **14**: p. 211-238.
173. Ellens, H., et al., *Membrane-Fusion And Inverted Phases*. Biochemistry, 1989. **28**(9): p. 3692-3703.
174. Delorme, N. and A. Fery, *Direct method to study membrane rigidity of small vesicles based on atomic force microscope force spectroscopy*. Physical Review E, 2006. **74**(3).
175. Pera, I., et al., *Using the atomic force microscope to study the interaction between two solid supported lipid bilayers and the influence of synapsin I*. Biophysical Journal, 2004. **87**(4): p. 2446-2455.
176. Murray, J., et al., *Imaging the selective binding, of synapsin to anionic membrane domains*. Chembiochem, 2004. **5**(11): p. 1489-1494.
177. Esser, L., et al., *Synapsin I is structurally similar to ATP-utilizing enzymes*. Embo Journal, 1998. **17**(4): p. 977-984.
178. Hilfiker, S., et al., *Synapsins as regulators of neurotransmitter release*. Philosophical Transactions of the Royal Society of London Series B-Biological Sciences, 1999. **354**(1381): p. 269-279.
179. Benfenati, F., et al., *Interactions of Synapsin-I with Small Synaptic Vesicles - Distinct Sites in Synapsin-I Bind to Vesicle Phospholipids and Vesicle Proteins*. Journal of Cell Biology, 1989. **108**(5): p. 1863-1872.

180. Benfenati, F., et al., *Electrostatic and Hydrophobic Interactions of Synapsin-I and Synapsin-I Fragments with Phospholipid-Bilayers*. *Journal of Cell Biology*, 1989. **108**(5): p. 1851-1862.
181. Cheetham, J.J., et al., *Identification of synapsin I peptides that insert into lipid membranes*. *Biochemical Journal*, 2001. **354**: p. 57-66.
182. Hosaka, M. and T.C. Sudhof, *Synapsins I and II are ATP-binding proteins with differential Ca²⁺ regulation*. *Journal of Biological Chemistry*, 1998. **273**(3): p. 1425-1429.
183. Carvalho, L.A. and A.M. Carmona-Ribeiro, *Interactions between cationic vesicles and serum proteins*. *Langmuir*, 1998. **14**(21): p. 6077-6081.
184. Westh, P., *Unilamellar DMPC vesicles in aqueous glycerol: Preferential interactions and thermochemistry*. *Biophysical Journal*, 2003. **84**(1): p. 341-349.

6 List of used mathematical symbols, constants and abbreviations

AFM	atomic force microscopy
STM	scanning tunneling microscopy
SPM	scanning probe microscopy
DLS	dynamic light scattering
SAM	self-assembled monolayer
DLVO	Derjaguin-Landau-Verwey-Overbeek theory
λ_D	Debye length
ϵ_0	dielectric constant ($8.854 \times 10^{-12} \text{ AsV}^{-1}\text{m}^{-1}$)
ϵ	dielectric constant of the medium
T	temperature
k_B	Boltzmann constant
c	concentration
e	unit charge ($1.602 \times 10^{-19} \text{ C}$)
LB	Langmuir-Blodgett
DOPC	1,2-dioleoyl- <i>sn</i> -glycero-3-phosphocholine
DPPC	1,2-dipalmitoyl- <i>sn</i> -glycero-3-phosphocholine
DPhPC /Diether-PC	1,2-di- <i>o</i> -phytanyl- <i>sn</i> -glycero-3-phosphocholine
T_m	phase transition temperature
SSM	solid-supported membranes
FV	force-volume plot
k	spring constant
δ	distance
D	diffusion coefficient
d (H)	hydrodynamic radius
η	viscosity

SV	synaptic vesicles
USV	untreated synaptic vesicles
SSV	synapsin-depleted synaptic vesicles
FUSV	frozen untreated synaptic vesicles
BSA	bovine serum albumine
S	stiffness
E	Young's modulus

Curriculum Vitae

Personal information

Address

Ann-Katrin Awizio

<mailto:Ann-Katrin.Awizio@kasystron.de>

Education

09/1983 - 06/1996

Freie Waldorfschule Uhlandshöhe, Stuttgart,
Abitur 1,6

Studies

10/1997 – 04/2002

Diploma studies of Biology at the University of Konstanz
Grade: gut

09/2001 – 04/2002

Diploma thesis at the company Multimatrix GmbH, Regensburg
Grade: sehr gut

Work experience

03/2002 – 09/2002

Biologist at the company Microbionix GmbH, Regensburg

- Development of medical diagnostics based on the Luminex technology

10/2002 – 08/2003

Scientific employee at the Molecular Virology Group at the Institute for Medical Microbiology and Hygiene, University of Regensburg

- Design and recombinant manufacturing of a chemokine within the HIV vaccination development program

11/2003 – heute

PhD student in the group of Polymer Physics of Prof. Butt at the Max Planck Institute for Polymer Research, Mainz

- Investigation of lipid membranes and synaptic vesicles with the atomic force microscope and dynamic light scattering

Publications

'The Influence of Synapsin on the Stiffness and on the Aggregation Behaviour of Synaptic Vesicles', Biophysical Journal, Aug 2007
Awizio A-K, Onofri F, Benfenati F, Bonaccorso E

'Atomic Force Microscopy of Lipid Bilayers'
Advances in Planar Lipid Bilayers and Liposomes Vol 3, Chap 7
Butt H-J, Awizio A-K

Conferences

European SPM Conference, Montpellier
Scanning Probe Microscopy, Sensors & Microstructures, June 3-6,
Vortrag

International Conference on Nanoscience and Technology, Basel
ICN+T 2006, July 30- August 4, 2006
Poster 771 at Session 'Biomolecular Interactions'